

ASSESSMENT OF WHITE MATTER INTEGRITY IN BONNET MACAQUE MONKEYS  
USING DIFFUSION-WEIGHTED MAGNETIC RESONANCE IMAGING

by

Lavanya Umapathy

---

Copyright © Lavanya Umapathy 2016

A Thesis Submitted to the Faculty of the  
DEPARTMENT OF ELECTRICAL AND COMPUTER ENGINEERING  
In Partial Fulfillment of the Requirements  
For the Degree of  
MASTER OF SCIENCE  
In the Graduate College  
THE UNIVERSITY OF ARIZONA

2016

## STATEMENT BY AUTHOR

The thesis titled *Assessment of White Matter Integrity in Bonnet Macaque Monkeys using Diffusion-weighted Magnetic Resonance Imaging* prepared by *Lavanya Umapathy* has been submitted in partial fulfillment of requirements for a master's degree at the University of Arizona and is deposited in the University Library to be made available to borrowers under rules of the Library.

Brief quotations from this thesis are allowable without special permission, provided that an accurate acknowledgement of the source is made. Requests for permission for extended quotation from or reproduction of this manuscript in whole or in part may be granted by the head of the major department or the Dean of the Graduate College when in his or her judgment the proposed use of the material is in the interests of scholarship. In all other instances, however, permission must be obtained from the author.

SIGNED: Lavanya Umapathy

## APPROVAL BY THESIS DIRECTOR

This thesis has been approved on the date shown below:

<hr/>	<u>11/22/2016</u>
<i>Dr. Theodore Trouard</i>	Date
<i>Professor, Biomedical Engineering</i>	
<hr/>	<u>11/22/2016</u>
<i>Dr. Ali Bilgin</i>	Date
<i>Associate Professor, Electrical &amp; Computer Engineering</i>	

## Table of Contents

<b>Abstract</b> .....	14
<b>Chapter 1</b> Diffusion Weighted Imaging - Background and Theory .....	15
1.1 Neuroimaging Modalities.....	15
1.2 Magnetic Resonance Imaging – Classical Theory .....	16
1.2.1 Contrast Mechanisms in MR Imaging .....	18
1.3 Diffusion MRI.....	19
1.3.1 Measuring Diffusion – from NMR to MRI.....	20
1.3.2 Echo Planar Imaging.....	24
1.3.3 Structures in Human Brain – an Overview .....	26
1.4 Introduction to q-space.....	28
1.4.1 Displacement PDF and q-space .....	29
1.4.2 Sampling: Acquisition Strategies in q-space .....	31
1.4.3 Reconstruction: Estimating Diffusion PDF .....	33
1.5 Fiber Tractography.....	42
1.5.1 Deterministic Tractography .....	43
1.5.2 Probabilistic Tractography.....	43
1.5.3 Quantitative Analysis using Tractography.....	44
1.6 Assessing Age-related Decline in Amygdala-Orbitofrontal interactions.....	46
1.6.1 Primate Models: An Alternative to Human Imaging Studies .....	48
1.6.2 Motivation for Current Work.....	48
1.6.3 Thesis Objective.....	48
<b>Chapter 2</b> MR Image Acquisition, Processing and Fiber Tractography.....	50
2.1 Image Acquisition Protocol.....	50
2.1.1 DICOM to NIFTI Conversion .....	51
2.2 Distortion Correction.....	52
2.2.1 Eddy Current Distortions .....	52
2.2.2 Susceptibility-induced Distortions.....	54
2.3 Bias Field Correction .....	57
2.4 Noise Reduction in Diffusion MRI.....	59
2.4.1 Overcomplete Local Principal Component Analysis based Denoising .....	60
2.4.2 Noise Filtering the Bonnet Diffusion-weighted Images .....	61

2.5	Registration to High-resolution Anatomical Images.....	62
2.5.1	Re-orientation of Images to Radiological Convention .....	62
2.5.2	Registering Diffusion-weighted Images to T1-weighted Images .....	63
2.6	Diffusion PDF Estimation.....	66
2.6.1	Model based Reconstruction.....	66
2.6.2	Model free CSD Reconstruction.....	69
2.7	Region of Interest Identification .....	71
2.7.1	Seed and Target Masks .....	71
2.7.2	Exclusion Mask.....	73
2.7.3	Inclusion Mask.....	74
2.8	Fiber Tractography.....	75
2.8.1	Multi-tensor Diffusion PDF based Probabilistic Tractography .....	75
2.8.2	FOD based Probabilistic Tractography.....	76
2.8.3	Tractography Parameters .....	76
Chapter 3	Assessing Uncinate Fasciculus Tract Integrity in Bonnet Macaque Monkeys.....	77
3.1	Probabilistic Fiber Tractography.....	77
3.1.1	Connectivity Map from Multi-Tensor Fit based Tractography .....	77
3.1.2	Streamlines from Fiber Orientation Distribution based Tractography .....	79
3.1.3	Connectivity Map vs FOD Streamlines .....	81
3.2	Quantifying Uncinate Fasciculus Tract Integrity.....	83
3.2.1	Tract-based Analysis.....	83
3.3	UF Connectivity mask for DTI Parameters.....	85
3.3.1	HARDI parameters .....	87
3.4	Statistical Analysis .....	88
3.4.1	Assessing relationship between age and imaging parameters .....	88
3.4.2	Assessing relationship between behavioral performance and imaging parameters	92
3.5	Discussion .....	96
3.5.1	Axial and Radial Diffusivity in the white matter along the entire brain.....	96
3.5.2	Outliers in analysis.....	98
3.5.3	Laterality in the uncinate fasciculus .....	100
3.6	Conclusion.....	100
APPENDIX A	Local Principal Component Analysis based Filtering in x-q space.....	101

A.1 Finding the nearest neighbor .....	103
A.2 Joint Filtering .....	104
A.3 Comparison with Local Principal Component Analysis based Denoising.....	105
A.3.1 Diffusion Computer Phantom for Gold Standard.....	105
A.3.2 Addition of Noise .....	106
A.3.3 Noise Estimation.....	107
A.4 Results and Discussion.....	108
REFERENCES .....	112

## List of Figures

Figure 1.1: Net magnetic moment from spins in a volume is aligned along the direction of the strong magnetic field along z-direction (A). On application of a 90° RF pulse, the spins are tipped to the transverse plane (B). In addition to dephasing, resulting in a decay of the  $M_{xy}$  component, the spins recover to the original magnetization along z (C)..... 17

Figure 1.2: Different contrast images in MRI. From left to right: T1-weighted, T2-weighted and Diffusion-weighted image ..... 19

Figure 1.3: An illustration of the displacement distribution of water molecules..... 20

Figure 1.4: Diagram showing a pulsed gradient spin-echo sequence used in diffusion MR imaging. The two diffusion sensitizing gradients wrap and unwrap phase respectively along the gradient direction.  $\delta$  = duration of diffusion pulse,  $\Delta$  = diffusion time interval. .... 21

Figure 1.5: The plot illustrates signal decay curves corresponding to two tissues with different diffusion coefficients  $D1$  and  $D2$  where tissue with  $D1$  experiences greater diffusion when a gradient is applied along a certain direction. As the b-value increases, the separation between the two curves increases, giving rise to contrast between the two tissues..... 24

Figure 1.6: A pulse sequence diagram for an EPI sequence is shown. With each read out gradient, the signal is read out in the Fourier space along the x-direction as shown in the image on the right. Each blip on the phase encode direction helps in traversing a small distance along the y-direction. The next read out enables reading this new line of information. In this way, a train of blips and read out gradients traverse the entire k-space in a zig-zag fashion. .... 25

Figure 1.7: An axial slice of human brain showing no diffusion weighting image and diffusion-weighted images where gradients are played along three different orientations. The directions along which the diffusion gradients were played are indicated by the yellow arrow..... 25

Figure 1.8: Structure of a neuron showing gray matter and white matter. The white matter consists of myelinated neuron and connects regions of gray matter. .... 26

Figure 1.9: A representation of random motion of water molecules in cerebrospinal fluid, gray matter and white matter. .... 27

Figure 1.10: Diffusion weighted images acquired at a given b-value ( $b=1000s/mm^2$ ) and $\Delta$ . The q-vectors and the corresponding diffusion-weighted images show a loss of MR signal in tissues oriented along the direction of the vectors.....	29
Figure 1.11: Diffusion in different tissues and the corresponding diffusion ellipsoid shapes.....	31
Figure 1.12: A single shell high angular resolution diffusion imaging sampling scheme that samples q-space on the surface of a sphere of fixed radius .....	32
Figure 1.13: An anisotropic diffusion tensor with the three eigenvectors indicated by the arrows and their corresponding eigenvalues.....	34
Figure 1.14: Diffusion tensors for voxel are overlaid on a fractional anisotropy map. Regions with crossing fiber (red arrows) show disc shaped diffusion tensor.....	35
Figure 1.15: The diffusion signal profile of a single fiber oriented along the z-direction is shown in (A). The corresponding response function is shown in (B).....	38
Figure 1.16: Observed signal is the Spherical Deconvolution of the response function with the FOD over the surface of a sphere. ....	39
Figure 1.17: Diffusion tensors (left) and fiber orientation distributions corresponding to each voxel (right) are overlaid on a fractional anisotropy map. In the region of crossing fibers, the diffusion tensors are oblate, whereas the fiber orientation distributions show two distinct lobes with different colors. The colors correspond to the direction of the underlying fiber.....	42
Figure 1.18: Diffusion tensors that approximately describe diffusion in a white matter voxel and a gray matter/CSF voxel are shown. The uncertainty in the direction of the fiber is illustrated next to the tensors. ....	44
Figure 1.19: An illustration of the possible orientations of two fibers within a voxel in the top row with the corresponding reconstructed diffusion tensor and fiber orientation distribution. With complex fiber orientations, such as kissing or bent fibers, the two techniques struggle to identify the underlying orientation correctly.....	45
Figure 1.20: A predicted model of interactions between the orbitofrontal cortex and Amygdala	47
Figure 2.1: A sagittal slice of a Bonnet monkey corresponding to the T1-, T2- and Diffusion-weighted images.....	51
Figure 2.2: Distortions due to eddy currents displayed on two images along opposite directions. The bottom row shows the distortion corrected images corresponding to the top row. ....	54

Figure 2.3: Coronal slices of a monkey brain showing susceptibility-induced distortions in diffusion-weighted images (A) and distortion-free T2-weighted images (B) ..... 55

Figure 2.4: Coronal slices arranged from anterior to posterior slices of a monkey. (A) DW images with distortion along PE direction. Signal loss can be seen in the inferior regions of the brain. (B) Final results from TORTOISE after registering with distortion free T2-weighted images (C)..... 57

Figure 2.5: Non-bias corrected DW brain images showing sagittal (A) and axial (D) slices. (B) and (E) show the bias fields with inhomogeneity in the posterior regions of the brain, (C) and (F) are the bias corrected images corresponding to sagittal and axial slices respectively. .... 59

Figure 2.6: Top row corresponds to noisy sagittal (A) and axial (B) slice of a macaque brain. Bottom row (C) and (D) show the denoised versions of the sagittal and axial slices respectively. .... 62

Figure 2.7: Original data (A) and images after re-orientation as per radiological convention (B). The labels on the images are Superior (S), Right (R), Anterior (A) and Posterior (P). The RAS convention is: x (Left to Right), y (Posterior to Anterior) and z (Superior to Inferior). The Vitamin-E capsule marking the right side of the animal is visible as a bright spot in the image outside the brain..... 63

Figure 2.8: A T1-weighted image (A) and the corresponding DW image registered to it using Boundary based registration (C) are shown. Also included are the zoomed in versions of the area highlighted in the yellow box for the T1-weighted (B) and DWI (D). The white matter edge (in red) identified by FSL’s FAST algorithm is overlaid on the two images..... 65

Figure 2.9: Sagittal, coronal and axial cross-sections of a monkey brain showing the T1-weighted images in (A), the corresponding fractional anisotropy (B), axial diffusivity (C) and radial diffusivity (D) images. White matter has a high FA compared to the gray matter and cerebrospinal fluid. White matter pathways are visible in the T1- images in (A). Corresponding structures in fractional anisotropy and axial diffusivity images appear brighter than the surrounding structures. In the radial diffusivity images (D), the white matter appears darker as the gray matter and cerebrospinal fluid has higher diffusivity than white matte..... 67

Figure 2.10: Fractional Anisotropy map of a coronal slice in diffusion space (A) with up to three crossing fibers modelled in each voxel using BedpostX. This modelling is performed in the

native diffusion space. Image in (B) shows a zoom in of a small section of (A) showing the first (red), second (blue) and the third (pink) fiber modelled within each voxel. .... 69

Figure 2.11: The diffusion profile generated for the CSD operation in one of the monkeys. The function is ideally supposed to be a flat disk but the shape varies slightly due to the truncation of higher-order Spherical Harmonic coefficients..... 70

Figure 2.12: The voxels that were selected for the generation of the response function are highlighted in yellow. The image only shows the voxels from the axial slice being displayed... 70

Figure 2.13: FODs overlaid on an FA map (A). (B) is the zoom in to the yellow box. The ODFs are color-coded and are scaled by the underlying FA values. This means that voxels with higher FA will have larger FOD lobes..... 71

Figure 2.14: OFC binary mask (blue) overlaid on coronal (A-C from anterior to posterior of the brain), sagittal (D) and axial (E) cross-sections of a T1-weighted image. .... 72

Figure 2.15: Amygdala binary mask (red) overlaid on coronal (A-C from anterior of the brain to posterior), sagittal (D) and axial (E) cross-sections of a T1-weighted image. .... 73

Figure 2.16 A: Left-right separation mask in green on a sagittal slice and exclusion mask in yellow on a coronal slice. Exclusion mask in A excludes the commissure fibers, that crossover from the left to the right hemispheres. Exclusion mask in B excludes fibers from inferior longitudinal fasciculus from being taken into account. .... 74

Figure 2.17: Coronal cross-sections of a monkey brain showing the T1-weighted image (A), uncinat fasciculus inclusion mask in blue overlaid on the T1-weighted image (B) and the corresponding fractional anisotropy image. The coronal slice in A shows a clear separation between the frontal and the temporal lobes and marks the region of transition of the uncinat fasciculus..... 75

Figure 3-1: The connectivity map between amygdala and the orbitofrontal cortex (shown in blue) is overlaid on an axial cross-section of a fractional anisotropy image for one of the bonnet monkeys. The slice shows uncinat fasciculus tracts entering into the orbitofrontal cortex. Each voxel in the connectivity map represents the number of tracts that pass through that voxel and end up in orbitofrontal cortex. The tracts are shown in a red-yellow color map where yellow represents the maximum value of the connectivity map..... 78

Figure 3-2: The uncinat fasciculus connectivity map in one of the bonnet monkeys is overlaid on axial cross-sections (moving from inferior to superior) of the fractional anisotropy map. The

amygdala is highlighted in blue in the top row of the image and the orbitofrontal cortex is highlighted in blue in the bottom row of the image. Voxels that have less than 10% of the maximum number of tracts in the connectivity map were eliminated. .... 79

Figure 3-3: Fiber tracts from amygdala to orbitofrontal cortex are overlaid on axial slices moving from inferior to superior. The streamlines are direction-encoded i.e. the fibers going left to right are in red, superior to inferior are in blue and posterior to anterior are in green. From every voxel in the seed amygdala mask (in yellow in the posterior slices), 2000 streamlines are initiated. All streamlines that reach the mask (in yellow in the superior slices) through the waypoint uncinate fasciculus and do not enter any of the exclusion masks identified in Chapter 2 are shown here. 80

Figure 3-4: Fiber tracts from amygdala to frontal cortex are overlaid on sagittal slices moving from right edge to the medial regions of the brain. The streamlines are direction-encoded i.e. the fibers going left to right are in red, superior to inferior are in blue and posterior to anterior are in green. As the fibers emerge from the amygdala in the first image, they rise up and are blue in color. The hook shape of the uncinate fasciculus tracts can be seen in the third and the last image. .... 81

Figure 3-5: Axial slices of a T1-weighted bonnet brain show the overlaid uncinate tracts identified by a multi-tensor based (A) and a FOD based (B) probabilistic algorithm. Rows 3 and 4 also show the orbitofrontal cortex ROI in blue. Both the algorithms predict that the right uncinate fasciculus is stronger than the left for this particular monkey. .... 82

Figure 3-6: Probabilistic streamlines from uncinate fasciculus overlaid on axial cross-sections of a T1-weighted image belonging to a young monkey (A) and an aged monkey (B). The axial slices move from the inferior to the superior direction. The amygdala mask and the orbitofrontal cortex are highlighted in yellow in the first and the second row of A and B. The uncinate tracks are larger in number and thicker in the younger monkey than the older one. .... 84

Figure 3-7: A weighted connectivity map (right) is generated from a connectivity map (left). A probability map is created by first dividing each voxel in the connectivity map with the waytotal. A threshold is applied to the probability map such that any voxel that has a probability less than 40% of the 95<sup>th</sup> percentile of the histogram of the intensities in the probability map is set to zero. .... 86

Figure 3-8: Scatter plot of imaging measures from diffusion space and T1-weighted space. There is a strong correlation between the DTI imaging parameters extracted along the uncinate fasciculus in the two spaces. .... 87

Figure 3-9: A comparison of the mean fractional anisotropy index between the young and aged group of monkeys. The error bars represent standard error of means. .... 88

Figure 3-10: A comparison of the mean axial diffusivity index between the young and aged group of monkeys. There is a significant difference between the axial diffusivities in the right hemisphere of the two groups. .... 89

Figure 3-11: A comparison of the mean radial diffusivity index between the young and the aged group of monkeys. The difference in the right hemisphere is close to significant values, with the older monkeys in the group having a smaller radial diffusivity on average. .... 89

Figure 3-12: A comparison of the number of tracts between the amygdala and the orbitofrontal cortex in young and the aged group of monkeys. The tracts were identified by a FOD based tractography algorithm and were normalized by the seed amygdala volume. .... 89

Figure 3-13: Scatter plots showing the relationship between imaging parameters and age. From top to bottom, the imaging parameters are fractional anisotropy, axial diffusivity, radial diffusivity and the number of streamlines normalized by the amygdala volume. The columns from left to right are left hemisphere, right hemisphere and the average of the two hemispheres. The Pearson’s correlation coefficient ‘r’ and the p-values are depicted on each plot. .... 91

Figure 3-14: Scatter plots showing the relationship between imaging parameters and the performance of monkeys on a reversal-learning task. From top to bottom, the imaging parameters are fractional anisotropy, axial diffusivity, radial diffusivity and the number of streamlines normalized by the amygdala volume. The columns from left to right are left hemisphere, right hemisphere and the average of the two hemispheres. The Pearson’s correlation coefficient ‘r’ and the p-values are depicted on each plot. .... 93

Figure 3-15: Scatter plots showing the relationship between imaging parameters and the performance of monkeys on a delay no match to sample task with interference. From top to bottom, the imaging parameters are fractional anisotropy, axial diffusivity, radial diffusivity and the number of streamlines normalized by the amygdala volume. The columns from left to right are left hemisphere, right hemisphere and the average of the two hemispheres. The Pearson’s correlation coefficient ‘r’ and the p-values are depicted on each plot. .... 95

Figure 3-16: Figure shows a fractional anisotropy image (A), a white matter mask (B) obtained from the fractional anisotropy image by applying a threshold of  $FA > 0.25$ , the corresponding radial diffusivity image (C). The white matter mask (B) is applied to the radial diffusivity image to extract the image in (D). ..... 97

Figure 3-17: A comparison of the average radial diffusivity (A) and axial diffusivity (B) in the white matter voxels in young and aged subjects. For each subject, a white matter mask was applied on the radial and axial diffusivity maps ..... 97

Figure 3-18: Relationship of imaging parameters with DNMS with performance scores. The second column on the right excludes the outlier monkey from regression analysis. The negative correlation of the imaging parameters reverses to a good positive correlation. .... 99

Figure A.1: (A) shows a select orientation (in green) and five directions (red) closest to it. The projection of the b-vectors on the sphere on a 2D plane is shown in (B). ..... 101

Figure A.2: DW images corresponding to the closest directions highlighted in Figure A.1. The images are in the order of increasing distances from the direction of interest. Note the similarities in signal intensities. .... 102

Figure A.3: Diffusion-weighted image corresponding to an axial section of a human brain (A), denoising results from the local principal component analysis based filtering (B) and denoising results from directionally constrained x-q space filtering (C). .... 105

Figure A.4: The diffusion directions displayed on a unit sphere surface in q-space (A). Red is the direction of interest, with the corresponding DWI image (B). The vectors in green are the five orientations close to the direction in red and the corresponding DW images are shown in (C – G). ..... 106

Figure A.5: Diffusion-weighted image of the computer phantom corrupted by varying levels of Rician noise is shown. Images (A-F) are corrupted by Rician noise of level 1%, 2%, 3%, 5%, 7% and 9% of maximum B0 image intensity. As the amount of noise in the image increase, valuable signal information is lost. .... 107

Figure A.6: Diffusion-weighted image corrupted by 3% Rician noise in (A), noise standard deviation estimated in local blocks (B), regularized noise map (C) obtained by low pass filtering the standard deviation map in (B) ..... 108

Figure A.7: Root mean square error map for the two noise filtering algorithms at different noise levels. Each pixel represents the root mean square error in the estimation of that pixel across the

diffusion directions. The error map for local principal component analysis based denoising method for 3% and 7% Rician noise levels is shown in image (A) and (C). (B) and (E) are the error maps for directionally constrained x-q space filtering for 3% and 7% Rician noise level respectively. .... 109

Figure A.8: Root mean square error map for local principal component analysis based filtering technique (A) and directionally constrained x-q space filtering technique (B) at 5% Rician noise. Each pixel represents the root mean square error in the estimation of fractional anisotropy values when compared to the ground truth. .... 110

Figure A.9: A plot of root mean square error in the estimation of fractional anisotropy in the computer phantom for different levels of Rician noise. For low noise levels, the directionally constrained x-q space filtering technique outperforms the principal component analysis based filtering technique. As the level of Rician noise increases, the performance deteriorates and the error in estimation of fractional anisotropy values increase. .... 111

## Abstract

Diffusion-weighted magnetic resonance imaging (dMRI) has been used to non-invasively investigate the integrity of white matter and the connectivity of the brain. In this work, high angular resolution diffusion imaging (HARDI), an advanced dMRI methodology was developed and employed in bonnet macaque monkeys to study the connectivity of the orbitofrontal cortex (OFC) and amygdala, two gray matter regions involved in making reward-guided decisions. With age, it is believed that there is a decline in the white matter connectivity between these two regions, also known as uncinate fasciculus (UF), and that this affects reward-value assignment and feedback learning in older adults. The analysis pipeline involved correction for distortions due to eddy currents and field inhomogeneity, noise reduction using a local principal component analysis based technique and subsequent registration to the high-resolution T1-weighted images. Gray matter regions corresponding to OFC and amygdala were identified on the T1-weighted images and probabilistic tractography was carried out to delineate the tracts belonging to UF. The output connectivity map from tractography was used to extract imaging parameters of interest such as fractional anisotropy, axial and radial diffusivity along the UF. A significant reduction in the fractional anisotropy index and the axial diffusivity index along the UF tract was observed with increased age of monkeys. Compared to the left hemisphere, stronger trends were observed in the right hemisphere of the monkeys, indicating possible laterality.

## Chapter 1 Diffusion Weighted Imaging - Background and Theory

The human brain, an intricate neuronal network spanned by billions of neurons, is undeniably the most complex structure in the body. There is an innate need in the medical community to understand the structural and functional mechanisms of the brain (Casey, Giedd et al. 2000) with the hope that this knowledge would aid in demystifying the effects of normal aging on complex cognitive and behavioral processes. Research interest in this area is also aimed at understanding changes in the brain in several neurological brain abnormalities such as schizophrenia (Shenton, Dickey et al. 2001), drug-addiction, alcoholism, geriatric depression, Alzheimer's disease (AD), Multiple Sclerosis (MS), Parkinson disease, Cerebral Palsy (CP), etc.

### 1.1 Neuroimaging Modalities

Neuroimaging helps understand the structural and functional connectivity of the nervous system either directly through structural imaging or indirectly through functional imaging (Bihan 2003). Structural imaging involves assessing local cortical regions constituting the gray matter whereas functional imaging measures activity within these regions during cognitive or emotional processing. For example, functional imaging studies can be used to identify the regions of the brain that are activated when a visual or auditory stimuli is presented. Histology, in case of animals is an invasive imaging technique that provides high-resolution patterns using Haemotoxylin and Eosin (H&E), trichrome or other similar stains. When examined under an electron/light microscope, the white matter pathways can be observed at a molecular level. This high sensitivity and specificity comes at a price of it being invasive, labor-intensive and only possible post-mortem.

Other non-invasive imaging modalities include X-rays, cerebral angiography, computerized axial tomography (CT), Single Photon Emission Computed Tomography (SPECT), Positron Emission Tomography (PET) and Magnetic Resonance Imaging (MRI). Of these, MRI is non-invasive, non-ionizing, three-dimensional, and can image the entire brain anatomy. Another advantage to using MRI is the different type of imaging contrasts it offers, for example, contrast using the tissue-specific relaxation times in T1- and T2- weighted images, flow enhancement in vessels in MR angiography, blood oxygen level dependency (BOLD) contrast to measure brain activity in

functional MRI (fMRI) and diffusion of water molecules in neuronal pathways in diffusion-weighted MRI. The diffusion-weighted MRI technique provides indirect information about the axonal organization of the brain in vivo (Hagmann, Kurant et al. 2007, Mori, Kaufmann et al. 2002, Alexander, Lee et al. (2007), Jones 2010). It also reveals abnormalities in white matter fiber structure and provide brain connectivity models.

The current chapter explains the theory behind magnetic resonance imaging (MRI) and how diffusion MRI, in particular, is being used to image the structures of interest in the brain. The motivation behind the current thesis work is presented at the end of this chapter.

## 1.2 Magnetic Resonance Imaging – Classical Theory

MRI is based on signals from atoms with an odd number of protons and/or neutrons that possess a spin angular momentum, such as hydrogen ( $H^1$ ) nuclei and phosphorus ( $P^{31}$ ) nuclei. The abundance of water in biological tissues makes it safe to assume that the MR signal from human body is predominantly from hydrogen atoms. The  $H^1$  atoms from a volume of interest can be visualized as a spinning charged sphere that give rise to a magnetic moment. Under ordinary conditions, these spins are randomly oriented and their net magnetic moment is cancelled out. However, in the presence of a strong homogenous external magnetic field  $B_0$ , conventionally applied along the z-direction, these spins align along the  $B_0$  field. Some spins align in the direction of  $B_0$  and others in the opposite direction, resulting in a net magnetic moment  $M_0$  or  $M_z$ . In addition, these spins precess at a resonant frequency,  $\omega$ , also known as Larmor frequency, that is directly proportional to the applied magnetic field  $B_0$ :

$$\omega = \gamma B_0$$

Here the gyromagnetic ratio  $\gamma$  is equal to  $42.576 \text{ MHz T}^{-1}$ . Figure 1.1 shows net magnetization of a volume of protons aligned along the z-direction. Excitation involves application of a radio frequency (RF) pulse  $B_1$  tuned to the resonant frequency  $\omega$  in the transverse (x-y) plane. When this RF pulse is applied, the magnetization is tipped from its equilibrium position along z towards the transverse plane.

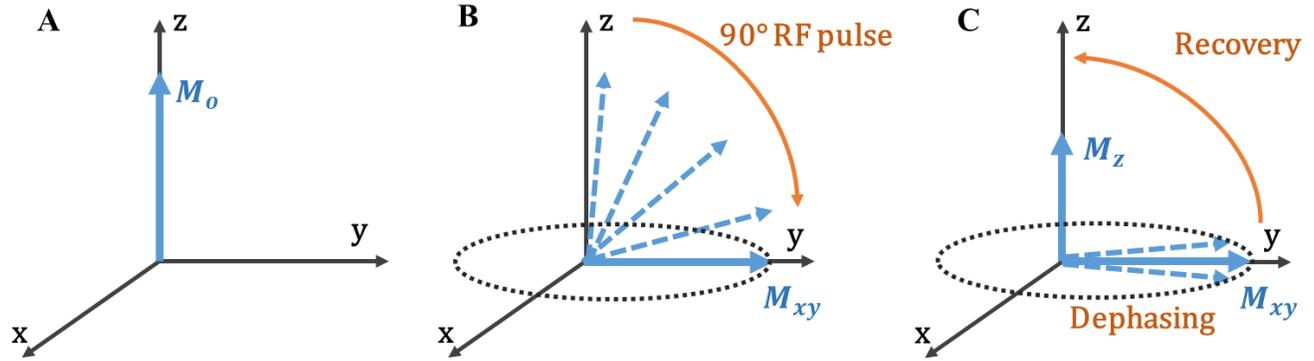


Figure 1.1: Net magnetic moment from spins in a volume is aligned along the direction of the strong magnetic field along z-direction (A). On application of a  $90^\circ$  RF pulse, the spins are tipped to the transverse plane (B). In addition to dephasing, resulting in a decay of the  $M_{xy}$  component, the spins recover to the original magnetization along z (C).

In a spin-echo MRI sequence, the strength of the  $B_1$  field is such that the angle of tipping (flip angle)  $\alpha$  is  $90^\circ$ . Once tipped to the transverse plane, as shown in Figure 1.1, the transverse magnetization  $M_{xy}$  precesses in the x-y plane at Larmor frequency  $\omega$  while slowly recovering to its equilibrium position along the z-direction. In this two-stage recovery,  $M_{xy}$  decays in the transverse plane due to dephasing of spins and  $M_z$  recovers along the z-axis. The signal relaxation in the transverse plane is governed by relaxation parameter T2 and the signal recovery along the z-axis is governed by the parameter T1. Both T1 and T2 are characteristics of water in the tissue of interest. Although the time constant T2 has contributions from static field inhomogeneities and is generally referred to as T2\*, the sequences used in this thesis minimize the contribution and so only T2 will be described. Receiver RF coils placed in the transverse plane, tuned to Larmor frequency,  $\omega$ , measure the precessing and decaying transverse magnetization  $M_{xy}$  which is the MR signal. The behavior of the magnetization vector is governed by the Bloch equations (Bloch, 1946). The MR signal measured by the receiver coil is proportional to the Fourier transform of the spatial distribution of the tissue being imaged.

In its simplest form, the MR signal in a voxel of tissue, S, can be modelled by:

$$S \propto S_0 \left(1 - e^{-\frac{TR}{T_1}}\right) e^{-\frac{TE}{T_2}} e^{-bD}$$

(1-1)

TR and TE are the repetition time and echo time of the MR signal and can be adjusted experimentally.  $S_0$  is the proton density within the voxel. The parameters  $D$  and  $b$  refer to the diffusion coefficient of water molecules and an experimental diffusion-weighting value, respectively; the significance of these two terms will be evident in the next few sections when we discuss diffusion-weighted MRI.

### 1.2.1 Contrast Mechanisms in MR Imaging

The physical properties of the tissue being imaged and the imaging parameters generate MR images with varying contrasts. The tissue properties consist of the proton density  $S_0$ , relaxation parameters  $T_1$ ,  $T_2$  and diffusion  $D$ . The imaging parameters include TR, TE and  $b$ . The commonly acquired contrasts are proton density (PD), T1-weighted, T2-weighted and diffusion-weighted. The proton density represents water concentration; T1 and T2 are signal relaxation times that depend on the rotational mobility of water. The diffusion coefficient,  $D$ , represents the translational or Brownian motion of water molecules.

By modifying imaging parameters TR, TE and  $b$  in the MR signal equation in (1-1), the contribution of T1, T2 and  $D$  to images can be controlled. Figure 1.2 illustrates the different contrasts for axial cross-sections of the human brain. A T1-weighted image is acquired using a short TR and a long TE such that the white matter in the brain that has the smallest T1 value appears bright compared to the gray matter. The cerebrospinal fluid with the highest T1 value appears darkest. The contrast is inverted in a T2-weighted image where we use a long TR and long TE and fatty tissues appear darker compared to tissues with higher water concentration. The diffusion-weighted image for a given  $b$ -value and a direction of diffusion causes the diffusion signal from tissues oriented along that direction to appear darker than the rest of the tissues.

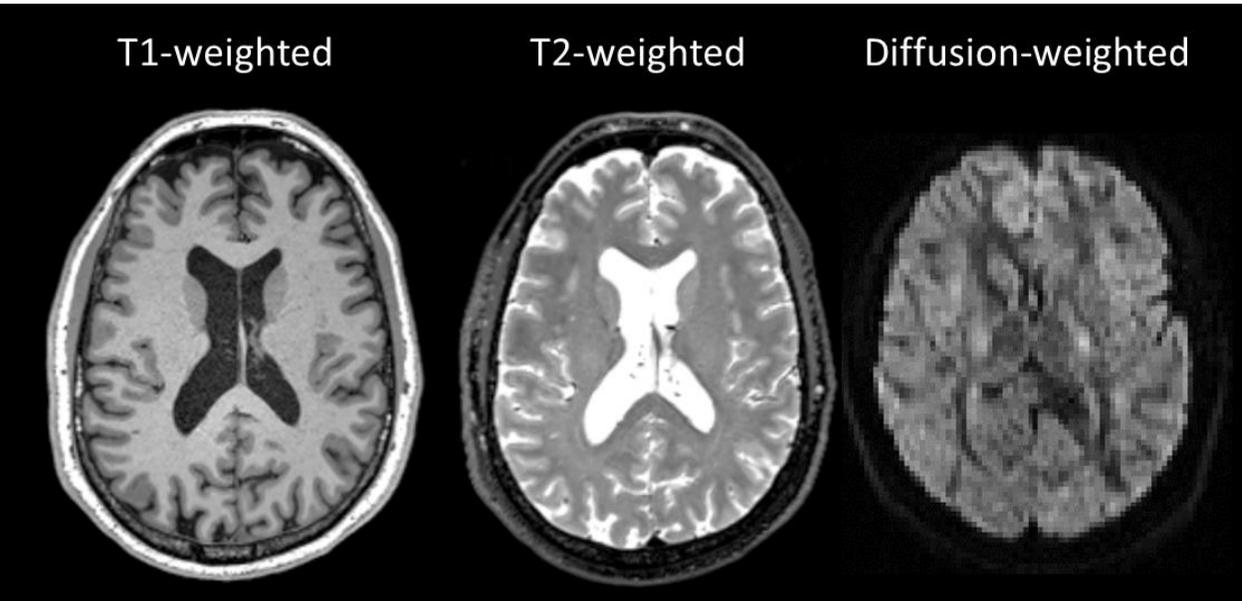


Figure 1.2: Different contrast images in MRI. From left to right: T1-weighted, T2-weighted and Diffusion-weighted image

### 1.3 Diffusion MRI

Molecular Diffusion or Brownian motion (Einstein 1905) refers to the notion that any molecule in a freely flowing liquid is randomly displaced when the molecule is agitated by thermal energy. This concept is similar to a random walk process of the water molecules. The displacement distribution of free water molecules is shown in Figure 1.3 as a distribution of the proportion of molecules that undergo displacement in a specific direction and to a specific distance during some time interval. Typically, this displacement follows a Gaussian distribution. In free diffusion or diffusion in a homogenous medium, the displacement is isotropic as there is no preferential direction. When the diffusion has a preferential direction, it is called anisotropic diffusion. Einstein showed that the mean square displacement of a particle over a time  $\delta$  is given by

$$\langle \Delta x^2 \rangle = 2D\delta$$

The diffusion coefficient  $D$  describes the ease with which molecules are displaced in a certain medium. For pure water at room temperature,  $D = 3 \times 10^{-9} m^2/s$ . Diffusion MRI exploits this motion of water molecules in tissues to measure microstructural anatomy.

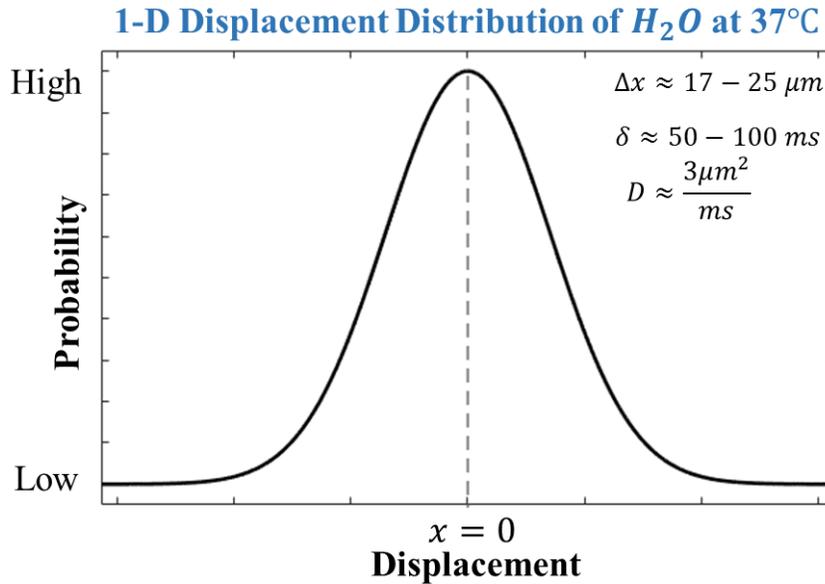


*Figure 1.3: An illustration of the displacement distribution of water molecules.*

### 1.3.1 Measuring Diffusion – from NMR to MRI

Modern diffusion-MRI borrows much of its foundational mathematics from the classic work by Stejskal and Tanner in the field of Nuclear Magnetic Resonance (NMR) spectroscopy. In their seminal paper (Stejskal, Tanner 1965), Stejskal and Tanner introduced pulsed gradients into a basic spin-echo sequence (Hahn 1950), resulting in diffusion sensitivity. They solved the Bloch-Torrey partial differential equation for a symmetric pair of pulsed gradients and obtained the famous Stejskal-Tanner formula shown below:

$$S = S_0 e^{-bD} \tag{1-2}$$

In their work, diffusion is measured by the inclusion of extra gradient pulses,  $G_{diff}$  as shown in the pulse sequence diagram in Figure 1.4. Diffusion gradients can be applied along any of the three gradient directions. For clarity, it will be assumed that  $G_{diff}$  is applied only along the x-direction.

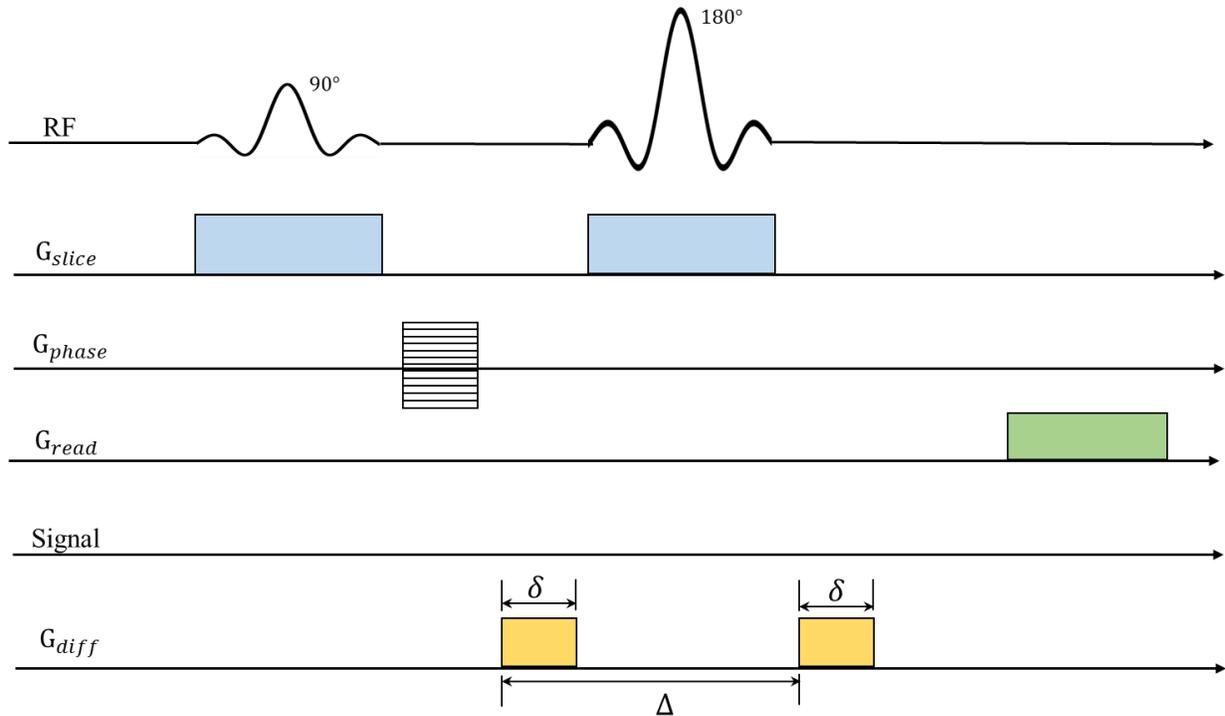


Figure 1.4: Diagram showing a pulsed gradient spin-echo sequence used in diffusion MR imaging. The two diffusion sensitizing gradients wrap and unwrap phase respectively along the gradient direction.  $\delta$  = duration of diffusion pulse,  $\Delta$  = diffusion time interval.

During the application of the first pulsed gradient of strength  $G$  and width  $\delta$ , water molecules initially at location  $x_0$  accumulate a net phase  $\Delta\phi_0$  given by:

$$\Delta\phi_0 = \omega(x_0)\delta = \gamma G x_0 \delta$$

Here, we have ignored the phase effects due to the main magnetic field  $B_0$  as it remains the same for all molecules. A second gradient pulse of similar strength and duration is applied after a time interval  $\Delta$ . The narrow pulse approximation, assumes  $\delta \ll \Delta$ , which means that no diffusion of water during the diffusion pulse needs to be considered. All subsequent derivations will assume the narrow pulse approximation. Let's consider two cases for water motion during the diffusion time  $\Delta$ :

**Case a: Water molecules do not move during the diffusion time  $\Delta$ .**

Net phase accumulated by the spins during the second pulsed gradient

$$\Delta\phi_{\Delta} = -\omega(x_0)\delta = -\gamma G x_0 \delta$$

Note that the negative sign is a result of the  $180^\circ$  RF pulse as shown in the spin-echo sequence that reverses the phase of the spins. After the two gradients, net phase accumulated by the molecules is zero.

$$\Delta\phi = \Delta\phi_0 + \Delta\phi_{\Delta} = 0$$

**Case b: Water molecules diffuse during time interval  $\Delta$  with diffusion coefficient  $D$ .**

Let us assume that the water molecules randomly diffuse during  $\Delta$  in 'n' discrete time steps with  $k_+$  steps along  $+x$  and  $k_-$  steps along  $-x$ . Then, the net displacement along  $+x$  is  $K_x \Delta x$ , where  $K_x = k_+ - k_-$  and  $\Delta x$  is the unit step size. The new spatial location  $x_1$  of the water molecules is given by:

$$x_1 = x_0 + \Delta x K_x$$

Net phase accumulated by the spins during the second pulsed gradient

$$\Delta\phi_1 = -\omega(x_1)\delta = -\gamma G x_0 \delta - \gamma G \Delta x K_x \delta$$

After the two gradients, net phase accumulated by the molecules is

$$\Delta\phi = \Delta\phi_0 + \Delta\phi_1 = -\gamma G \Delta x K_x \delta$$

Because the diffusion of molecules is a random process, and the MRI signal comes from the integration of the complex signal from many molecules, this accumulated phase leads to a signal decay. In its discrete formulation, and assuming a Gaussian distribution of displacements from diffusion, the MR signal measured is the sum of signal from all such molecules and is shown to be:

$$S = M_0 \cos^n(\gamma G \delta \Delta x)$$

Here,  $M_0$ , the initial magnetization of spins in the absence of any gradients cannot be truly identified. Therefore, another NMR signal is obtained in the absence of diffusion-sensitizing gradients, i.e.  $G=0$  and the normalized signal attenuation  $\frac{S}{S_0}$  is calculated.

$$S_0 = M_0 \cos^n(0) = M_0$$

$$\frac{S}{S_0} = \cos^n(\gamma G \delta \Delta x)$$

The mean square displacement of water molecules is given by  $\langle \Delta x^2 \rangle = 2D\Delta t$  where  $\Delta = n\Delta t$  and  $\Delta t$  is unit time. Substituting this in the normalized signal attenuation equation:

$$\gamma G \delta \Delta x = \sqrt{\gamma^2 G^2 \delta^2 \Delta x^2} = \sqrt{\frac{\gamma^2 G^2 \delta^2 2D\Delta}{n}} = \sqrt{\frac{2bD}{n}}$$

A new parameter b-value for the diffusion-sensitizing gradient is defined as  $b = \gamma^2 G^2 \delta^2 \Delta$ . This discrete formulation can be converted to continuous time, as described in (Stejskal & Tanner, 1965) to obtain:

$$\frac{S}{S_0} = \lim_{n \rightarrow \infty} \cos^n \left( \sqrt{\frac{2bD}{n}} \right) = e^{-bD}$$

$$\ln \left( \frac{S}{S_0} \right) = -bD$$

(1-3)

Contrast in diffusion MRI is generated by tissues with different diffusion coefficients, as shown in Figure 1.5. If two experiments are carried out, one with a no diffusion weighting, i.e.  $b = 0$  and one with  $b$  set to a finite value, the diffusion coefficient  $D$  can be easily calculated:

Because water in tissue does not have a single diffusion coefficient and because there are barriers and restrictions to water movement within a single voxel, we do not really measure true diffusion, but an apparent diffusion coefficient or ADC. The ratio of signal in two experiments, one without diffusion weighting to yield  $S_0$  and one with a non-zero b-value can be used to calculate ADC as.

$$ADC = -\frac{1}{b} \ln\left(\frac{S}{S_0}\right)$$

(1-4)

As described in later sections, the ADC, can be calculated for every voxel in an image and for multiple directions in each voxel.

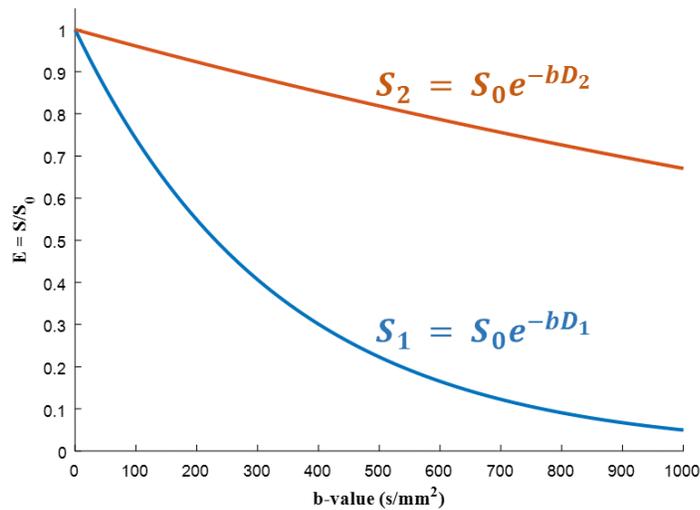


Figure 1.5: The plot illustrates signal decay curves corresponding to two tissues with different diffusion coefficients  $D_1$  and  $D_2$  where tissue with  $D_1$  experiences greater diffusion when a gradient is applied along a certain direction. As the  $b$ -value increases, the separation between the two curves increases, giving rise to contrast between the two tissues.

### 1.3.2 Echo Planar Imaging

Echo Planar Imaging (EPI) is a fast data acquisition strategy that can acquire an MR image from a slice from a single excitation and in the period of 50-100 milliseconds. First described by Mansfield in 1977 (Mansfield 1977), it has gained popularity in the clinical setting where it can image rapidly changing physiological processes, such as a beating heart, with decreased motion artifacts. The pulse-sequence diagram of a spin-echo EPI sequence is shown in Figure 1.6. Following a 90-180 RF excitation pulse sequence, strong rapidly switching frequency encode (FE) gradients along the read out direction (x-direction) and blipped gradients along the phase encode (PE) direction (y-direction) are played out such that an entire 2D Fourier space is covered and the

center of Fourier space is collected at the spin-echo point. Thus, within a single RF excitation, this sequence samples the entire k-space for a slice in a serpentine fashion. Hence, it is also known as single-shot SE-EPI.

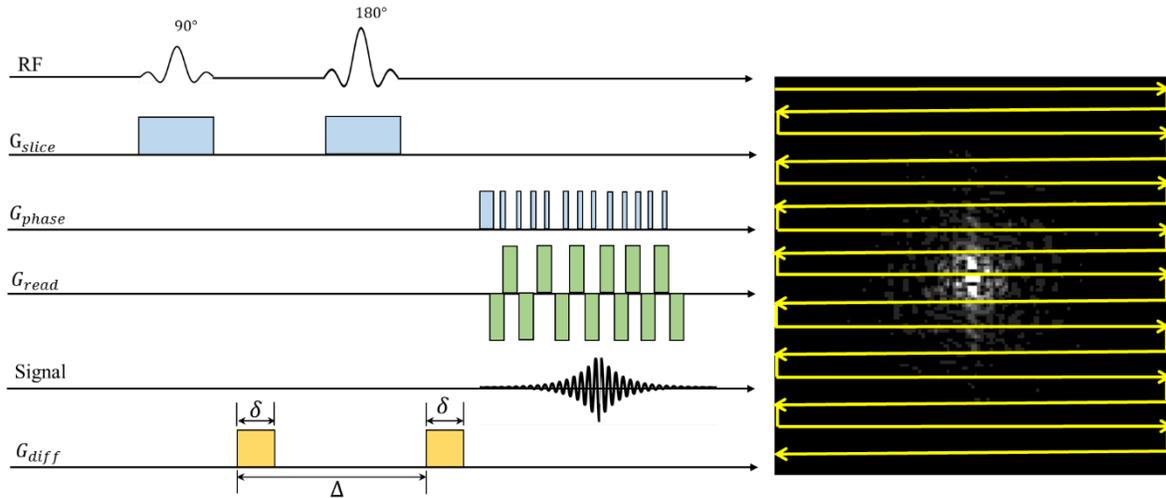


Figure 1.6: A pulse sequence diagram for an EPI sequence is shown. With each read out gradient, the signal is read out in the Fourier space along the x-direction as shown in the image on the right. Each blip on the phase encode direction helps in traversing a small distance along the y-direction. The next read out enables reading this new line of information. In this way, a train of blips and read out gradients traverse the entire k-space in a zig-zag fashion.

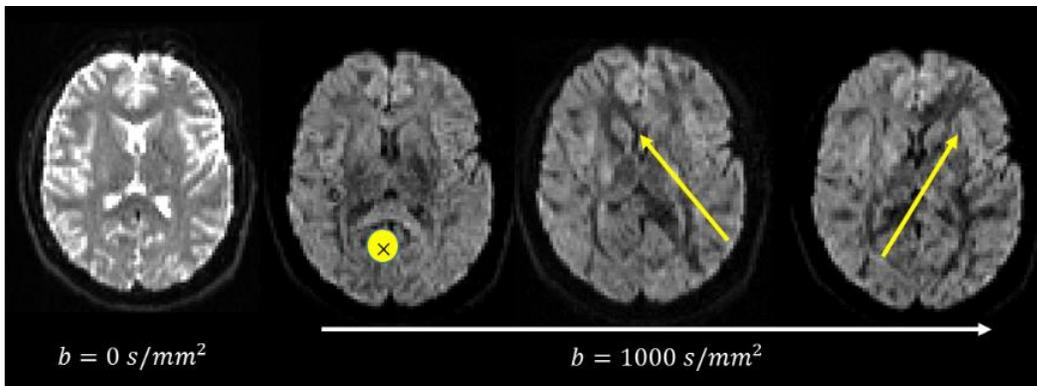
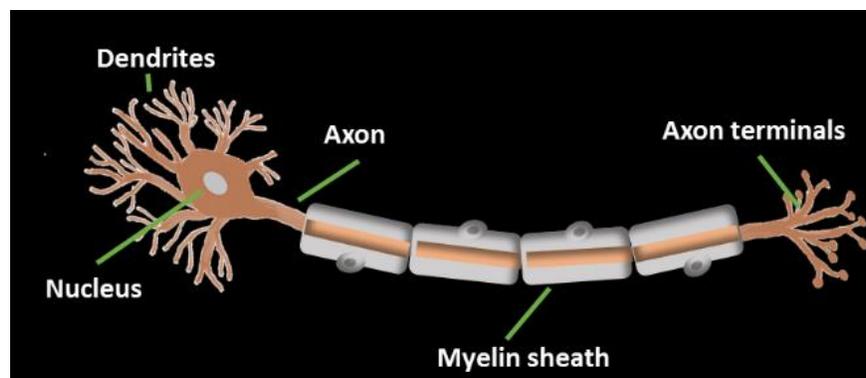


Figure 1.7: An axial slice of human brain showing no diffusion weighting image and diffusion-weighted images where gradients are played along three different orientations. The directions along which the diffusion gradients were played are indicated by the yellow arrow.

The fast read out in k-space leads to low bandwidth in the phase-encode direction, making the EPI sequence more sensitive to susceptibility effects and magnetic field inhomogeneity. The artifacts in EPI images and the approaches to correct for these distortions will be described in more detail in Chapter 2. Each traversal of the k-space produces a diffusion-weighted image. Figure 1.7 shows four diffusion-weighted images corresponding to different orientations of the diffusion gradient.

### 1.3.3 Structures in Human Brain – an Overview

The brain cells can be classified histologically into neurons and glial cells. Neurons either deliver information about the condition of the body and its external surroundings or integrate and process the delivered information. Glial cells, on the other hand, support and protect the neurons. A type of glial cell, *oligodendrocytes* wrap the axons of neurons to produce insulation called as myelin (Pfeiffer, Warrington et al. 1993).



*Figure 1.8: Structure of a neuron showing gray matter and white matter. The white matter consists of myelinated neuron and connects regions of gray matter.*

The unmyelinated neurons constitute the cortical regions of the brain or the gray matter (GM) and act as the processing centers in the brain. The myelinated neurons transmit information to and from the gray matter areas and connect them to the rest of the brain. Under autopsy, the bundles of myelinated neurons appear white due to the myelin sheath, hence the name white matter (WM). Long white matter fiber bundles are called fasciculi or tracts. WM comprises more than half of the volume of the cerebral hemisphere (Feldman, Yeatman et al. 2010).

### 1.3.3.1 Diffusion in Biological Tissues

Diffusion MRI uses the anisotropic diffusion of water molecules in brain tissues to infer its axonal organization (Pierpaoli, Basser 1996). The interaction between the diffusing water and well-ordered tissue microstructure, such as bundles of white matter ordered along a particular direction, results in anisotropy of the water displacement distribution, also known as diffusion profile (Beaulieu 2002). For example, the water molecules in and around axonal bundles in white matter have a higher rate of diffusion in a direction parallel to the fiber bundles compared to a perpendicular direction along which diffusion is impeded. Compare this to the cerebrospinal fluid (CSF) which is homogenous with isotropic diffusion. The water molecules in gray matter, owing to the presence of cellular structures, diffuses slowly compared to the diffusion along the long axis of white matter. Figure 1.9 illustrates diffusion in different types of brain structures.

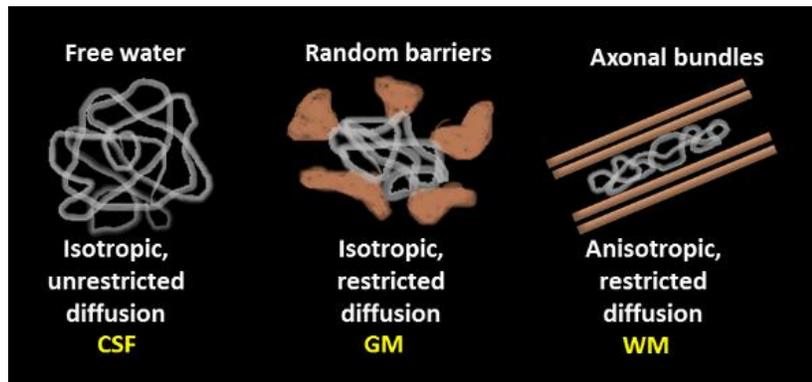


Figure 1.9: A representation of random motion of water molecules in cerebrospinal fluid, gray matter and white matter.

The anisotropic diffusion in white matter has been attributed to factors such as dense axonal packing, large axonal diameters, and high levels of myelination. Clinically, these factors have been used as an indicator for a healthy or mature white matter structure (Basser 1995). Pathologies in brain affect white matter. In the case of normal aging of brain, there is axonal pruning or axonal degradation and de-myelination. The ability to identify and characterize axonal fiber bundles is important to understand normal as well as pathological processes affecting higher cerebral functions of the brain (Mori, van Zijl 2002). Visualizing and characterizing white matter pathways in the brain, therefore, provide valuable insights into the intricate inner mechanisms of the brain.

## 1.4 Introduction to q-space

Similar to the concept of a k-space for Fourier data, q-space has been used in many studies (Callaghan, Eccles et al. 1988, Basser, Jones 2002) to visualize the complex relationship of the displacement distribution of molecules with the orientation of the diffusion gradients and the time interval between them. In diffusion MRI, a diffusion gradient can be applied along any orientation in 3D space. In q-space, the same diffusion gradient can be thought of as  $q(r_j, \theta_j, \phi_j)$ ;  $q \in R^3$  oriented along the direction of diffusion gradient  $(\theta_j, \phi_j)$  with its length  $r_j$  proportional to the gradient strength or the b-value. Mathematically, this is expressed as:

$$q = \frac{\gamma}{2\pi} \int_0^t G(t) dt = \frac{1}{2\pi} \gamma G \delta$$

The width  $\delta$  of the diffusion gradient is considered to be infinitesimally short such that the gradient waveform  $G(t)$  can be replaced by a delta function that has an area of  $G\delta$ . The b-value accounts for both the signal gradient and the time interval for diffusion and is related to the q-vector as follows:

$$b = (2\pi q)^2 \Delta$$

Images acquired at each point in q-space are generated from a diffusion gradient of certain orientation, b-value and diffusion time interval. The origin, for example, is a diffusion-weighted image corresponding to no gradients and a b-value of 0. Figure 1.10 shows diffusion-weighted images corresponding to three points in the q-space that have the same b-value but different orientations. In the diffusion image for q-vector along right-left orientation, the signal in axons that move in the left-right direction is highly attenuated. For e.g. in the corpus callosum, there is no signal in the horizontal orientation but in the other two diffusion-weighted images, signal is retained.

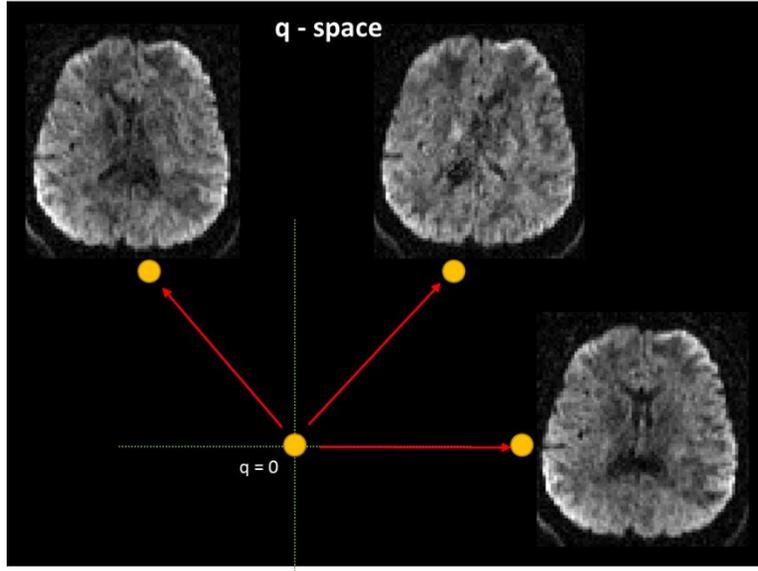


Figure 1.10: Diffusion weighted images acquired at a given  $b$ -value ( $b=1000\text{s/mm}^2$ ) and  $\Delta$ . The  $q$ -vectors and the corresponding diffusion-weighted images show a loss of MR signal in tissues oriented along the direction of the vectors

#### 1.4.1 Displacement PDF and $q$ -space

A displacement distribution or a diffusion probability density function (PDF) can be used to describe the motion of water molecules within an imaging voxel. It has been shown that a relationship exists between data measured in  $q$ -space and the underlying diffusion PDF (Basser, Jones 2002). Let  $P(r_0)$  be the initial distribution of spins in a volume and  $P(r_1|r_0, \Delta)$  be the conditional probability that  $H^1$  spins are displaced to position  $r_1$  in time  $\Delta$  from the initial position  $r_0$  when diffusion-sensitizing gradient pulses of strength  $G$  are applied. The phase accumulated by the spins during the diffusion time-interval  $\Delta$  is given by:

$$\Delta\phi = \gamma\delta G \cdot (r_1 - r_0)$$

The normalized echo attenuation  $E_\Delta(G)$  is given as:

$$E_\Delta(G) = \int \int P(r_0) P(r_1|r_0, \Delta) e^{i\Delta\phi} dr dr_1$$

$$E_\Delta(G) = \int \int P(r_0) P(r_1|r_0, \Delta) e^{i\gamma\delta G \cdot (r_1 - r_0)} dr dr_1$$

If we consider a homogenous diffusion medium, then the displacement PDF only depends upon the net displacement ‘r’ irrespective of the initial or final positions i.e.

$$P(r_1|r_0, \Delta) = P(r|0, \Delta) = P(r, \Delta); \text{ where } r = r_1 - r_0$$

The displacement PDF is defined as:  $P(r, \Delta) = \int P(r_0) P(r_0 + r|r_0, \Delta) dr$

This is the probability that a spin at any location is displaced along the gradient direction during the diffusion time interval. The expression for the normalized echo attenuation reduces to the following:

$$E_{\Delta}(G) = \int P(r, \Delta) e^{i\gamma\delta gr} dr$$

Substituting for  $q$  we get,

$$E_{\Delta}(q) = \int P(r, \Delta) e^{i2\pi qr} dr$$

(1-5)

where

$$q = \frac{1}{2\pi} \gamma G \delta$$

The integral here shows that the measured normalized diffusion attenuation signal is the Fourier transform of the displacement probability density function. Using inverse Fourier transform formulation, one can get the displacement PDF if the diffusion signal in q-space is known, i.e. when the sample points from q-space are Fourier transformed in every voxel, the result is the displacement distribution profile of water in that voxel.

$$P(r, \Delta) = \int E_{\Delta}(q) e^{-i2\pi qr} dr$$

This interesting relationship has been exploited in numerous sampling and reconstruction techniques to recover the diffusion PDF. Sampling data in the q-space is equivalent to acquiring diffusion images along different directions and/or different b-values. Therefore, by sampling a larger number of points in the q-space, the resolution of the Fourier transform and the water

displacement PDF can be increased. The following section introduces techniques of sampling q-space and reconstructing the diffusion PDF.

## 1.4.2 Sampling: Acquisition Strategies in q-space

### 1.4.2.1 Diffusion Spectrum Imaging

The obvious sampling technique is to sample the q-space on a regular Cartesian grid. This is referred to as q-space imaging (QSI) or Diffusion spectrum imaging (DSI) (Weeden, Hagmann et al. 2005). DSI provides a high resolution of the underlying diffusion PDF and the fiber structure but also requires longer scans as a large number of points in the q-space need to be sampled. It uses the Fourier relationship in equation (1-5) to measure the diffusion PDF directly without applying a model.

### 1.4.2.2 Diffusion Tensor Imaging

The notion to model the diffusion PDF as a tensor ellipsoid was introduced by Basser (Basser 1995). Mathematically, a tensor or a 3D ellipsoid can be completely described by three eigenvectors corresponding to the three axes and three eigenvalues corresponding to the intercepts along these axes. By measuring diffusion along a minimum of six non-collinear directions in q-space, these six parameters can be estimated. The technique was referred to as diffusion tensor imaging (DTI) (Basser 1995). The diffusion tensors corresponding to CSF, GM and WM are depicted in Figure 1.11.

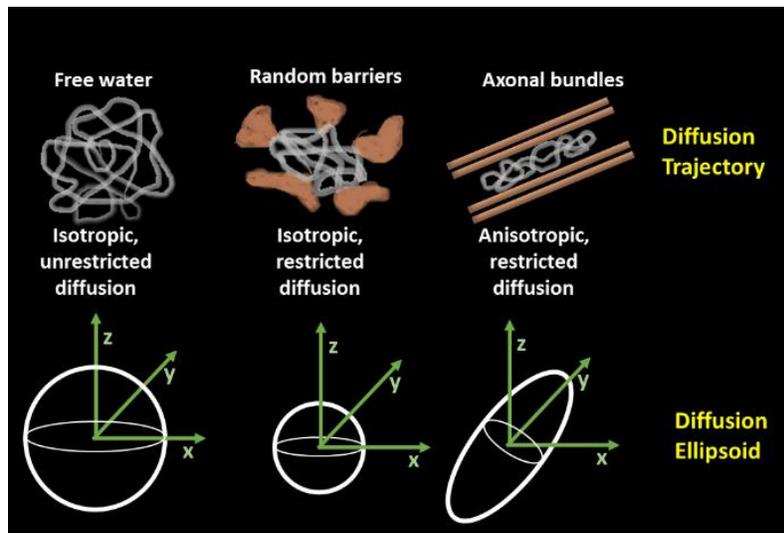
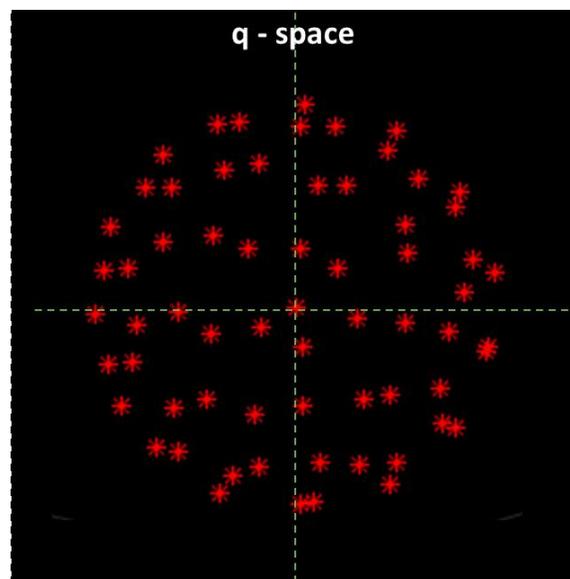


Figure 1.11: Diffusion in different tissues and the corresponding diffusion ellipsoid shapes

In the case of Gaussian and isotropic diffusion similar to that in CSF or gray matter, the diffusion tensor is simply a sphere. In white matter, diffusion is known to be anisotropic and hence a cigar or disc-shaped diffusion tensor. With the need to measure only six points in q-space, DTI clearly has an advantage over the DSI with respect to the acquisition time. However, sampling very few points in q-space provides poor resolution of the diffusion PDF, leading to researchers exploring other complex alternatives. Nevertheless, it is the most common technique used in clinical application of diffusion-MRI.

### 1.4.2.3 High Angular Resolution Diffusion Imaging

High angular resolution diffusion imaging or HARDI (Tuch, Reese et al. 2002) was proposed as an alternative to DSI and DTI. It provides better resolution of the underlying diffusion PDF without completely sampling q-space. HARDI acquires a large number of q-space samples along orientations  $(\theta_j, \phi_j)$  on the surface of a spherical shell of constant radius 'r' corresponding to a single b-value, typically greater than  $b = 1000 \text{ s/mm}^2$ . This is referred to as single shell imaging. A sample single shell HARDI acquisition scheme is shown in Figure 1.12.



*Figure 1.12: A single shell high angular resolution diffusion imaging sampling scheme that samples q-space on the surface of a sphere of fixed radius*

### 1.4.3 Reconstruction: Estimating Diffusion PDF

Once the q-space samples have been acquired, several reconstruction strategies exist to estimate the displacement PDF of the tissues from the measured MR signal. Estimation is done either by fitting the data to a pre-hypothesized model and or by using a model free approach.

#### 1.4.3.1 Model based Approaches

These techniques assume a particular shape or distribution for the diffusion PDF and search for a set of parameters that best fit the data.

#### Elliptical Tensor model - DTI

As discussed earlier, DTI hypothesizes the shape of the diffusion PDF to be an elliptical tensor and fits the observed signal to an ellipsoid (Basser, Mattiello et al. 1994, Basser, Jones 2002). Using diffusion-weighted images and the corresponding b-values at which they were acquired, an apparent diffusion coefficient (ADC) is calculated for every direction using equation (1-4). A diffusion tensor can be described by a 3x3 matrix, requiring the calculation of ADC for at least 6 collinear directions.

$$D = \begin{bmatrix} D_{xx} & D_{xy} & D_{xz} \\ D_{yx} & D_{yy} & D_{yz} \\ D_{zx} & D_{zy} & D_{zz} \end{bmatrix} = \mathcal{V}\Lambda\mathcal{V}^T$$
$$\Lambda = \begin{bmatrix} \lambda_1 & 0 & 0 \\ 0 & \lambda_2 & 0 \\ 0 & 0 & \lambda_3 \end{bmatrix} \quad \text{and } \mathcal{V} = [\vec{v}_1 \quad \vec{v}_2 \quad \vec{v}_3]$$

Here,  $D_{ij}$  corresponds to ADC in a voxel corresponding to a diffusion gradient applied along the  $(i, j)$  direction. The eigenvectors  $\mathcal{V}$  and eigenvalues  $\Lambda$  of matrix  $D$  represent the direction of principle diffusion within a voxel and the strength of diffusion respectively (Basser, Mattiello et al. 1994). The largest eigenvalue is represented by  $\lambda_1$  and its corresponding eigenvector  $v_1$  is the direction of maximum diffusion for a given diffusion tensor. The mean diffusion in the voxel is given by the trace of the diffusion matrix. The shape of the diffusion tensor is determined by the eigenvalues. In Figure 1.13, a cigar shaped diffusion tensor is shown that exhibits preferential diffusion along  $\lambda_1$ . Here  $\lambda_1 \gg \lambda_2$  and  $\lambda_3$ .

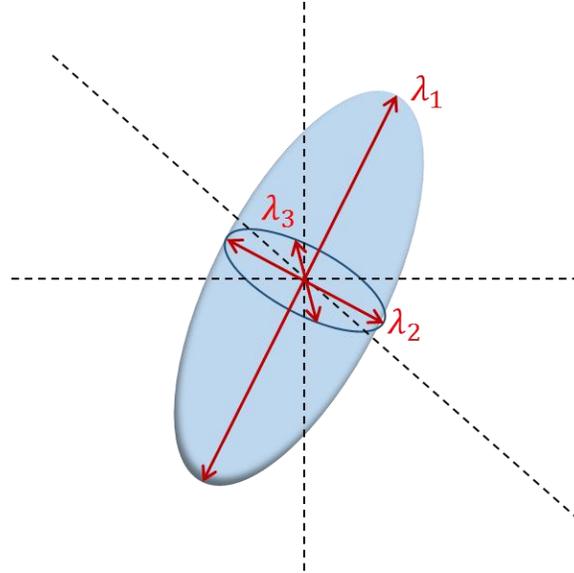


Figure 1.13: An anisotropic diffusion tensor with the three eigenvectors indicated by the arrows and their corresponding eigenvalues.

A number of studies use scalar parameters derived from the eigenvalues of the diffusion matrix to quantify diffusion. These scalar parameters are rotationally invariant such that they do not depend on the orientation of a patient's head in the scanner. These can also be used for univariate statistical tests. These are fractional anisotropy (FA), axial diffusivity (AD), radial diffusivity (RD) and mean diffusivity (MD). FA is a number between 0 and 1 where a score of 0 in a voxel implies a spherical diffusion tensor with isotropic diffusion and a score of 1 implies highly anisotropic behavior. Axial diffusivity measures the strength of the diffusion along the direction of maximum diffusion. Radial diffusivity refers to the diffusion in a direction perpendicular to the direction of maximum diffusion. Mean diffusivity is simply the average diffusion in the voxel.

The formal definition of these parameters is given below:

$$FA = \sqrt{\frac{3}{2}} \sqrt{\frac{(\lambda_1 - \bar{\lambda})^2 + (\lambda_2 - \bar{\lambda})^2 + (\lambda_3 - \bar{\lambda})^2}{\lambda_1^2 + \lambda_2^2 + \lambda_3^2}}$$

$$AD = \lambda_1 \quad RD = \frac{\lambda_1 + \lambda_2 + \lambda_3}{3} \quad MD = \bar{\lambda} = \frac{\lambda_1 + \lambda_2 + \lambda_3}{3}$$

(1-6)

A common assumption in DTI is that the direction of maximum diffusion corresponds to the direction of the axonal bundles in a voxel (Basser, Mattiello et al. 1994). As such, AD represents the diffusivity along the fiber bundle and RD represents the diffusivity perpendicular to the fiber bundle. White matter with pathologies, either due to normal aging or due to neurological disorders, typically exhibit reduced FA, reduced AD and increased RD. Although there is an abundance of clinical studies that associate radial diffusivity with myelin damage (de-myelination) and axial diffusivity with axonal degeneration (Song, Sun et al. 2002, Kumar, Nguyen et al. 2012), there is increasing concern in the research community that these metrics cannot be construed as true representatives of myelin/axonal damage without additional proofs such as post-mortem dissections (Wheeler-Kingshott, Cercignani 2009, Jones, Cercignani 2010).

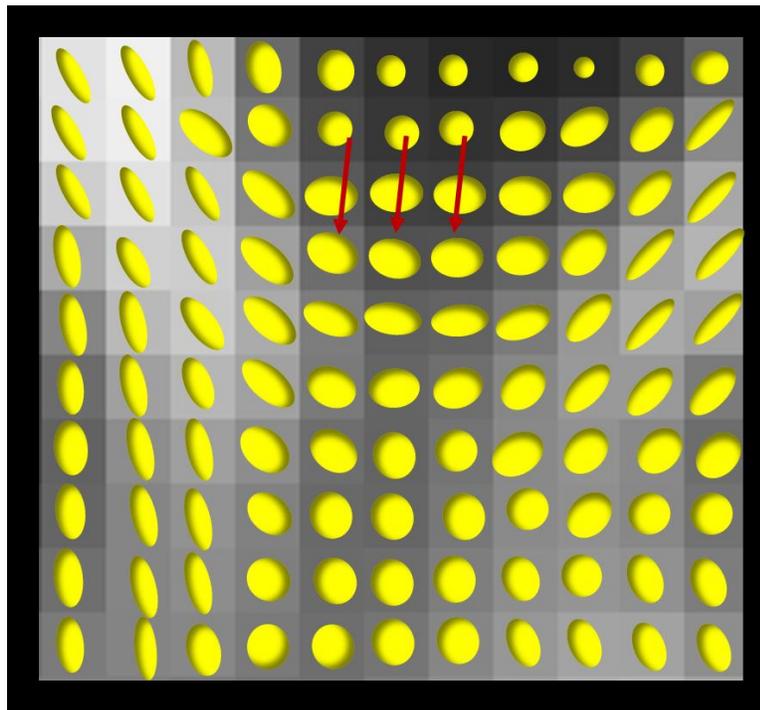


*Figure 1.14: Diffusion tensors for voxel are overlaid on a fractional anisotropy map. Regions with crossing fiber (red arrows) show disc shaped diffusion tensor.*

The DTI model is simple to calculate and requires few assumptions about data acquisition and reconstruction while working accurately in regions with a single fiber population. The biggest criticism of the DTI model is that it fails to capture complex fiber orientation in a voxel, i.e., when

there are multiple fiber bundles occupying the same voxel that are oriented along different directions. For example, when there are two directions of maximum diffusion in a voxel, corresponding to crossing fibers, the reconstructed diffusion tensor is pancake-shaped or oblate as  $\lambda_1 = \lambda_2$ . As a result, any information about the directions of the crossing fibers is lost. Figure 1.14 shows diffusion tensor ellipsoids overlaid on a zoomed in version of FA map showing regions of crossing fibers. Diffusion ellipsoid is cigar shaped in regions with a high FA, appearing brighter in the image, and spherical in regions with low FA. The regions with intermediate FA, appearing gray in the image, could be a result of pathology or multiple fiber crossings.

### Multi-compartment model

An alternative to the DTI single tensor model is the multi-compartment model (Behrens, Woolrich et al. 2003, Hosey, Williams et al. 2005) that considers partial volume effects. The diffusion signal contributed by different compartments within a voxel is assumed to be independent of each other and the observed signal in each voxel is the sum total of the signal contributions from individual compartments. An example of the two-compartment model is the ball and stick model where the diffusion model consists of an anisotropic compartment consisting of a fiber bundle and an isotropic compartment that models inter-cellular water that is free to move. The diffusion signal equation describing a two-compartment model is given by:

$$S_k = S_0 \left( (1 - f)e^{-b_k d} + f e^{-b_k d r_k^T R A R^T r_k} \right)$$

Here,  $S_k$  is the measured DW-MRI signal,  $d$  is the diffusivity,  $b_k$  and  $r_k$  are the b-value and the gradient orientation for the  $k^{\text{th}}$  diffusion gradient at each voxel. The signal contributed by the single fiber, or the volume fraction of the fiber, in the voxel is given by  $f$  and  $(1 - f)$  represents the proportion of voxel that contributes to the isotropic diffusion. The term  $R A R^T$  is the diffusion tensor oriented along the fiber direction  $(\theta, \phi)$ . A multi-compartment model for diffusion assumes the presence of  $N$  fibers each contributing a volume fraction  $f_j$ , with a diffusion tensor oriented along  $R_j A R_j^T$ .

$$S_k = S_0 \left( \left( 1 - \sum_{j=1}^N f_j \right) e^{-b_k d} + \sum_{j=1}^N f_j e^{-b_k d r_k^T R_j A R_j^T r_k} \right)$$

### 1.4.3.2 Model Free Approaches

A model-free reconstruction strategy infers the shape of the distribution by looking only at the probability density function (PDF) of the MRI data. Model free techniques have been shown to capture the complexity of diffusion PDF better than the model-based approaches but are computationally more expensive and dependent on the way q-space is sampled. Although many HARDI model free reconstruction techniques exist, the one that will be considered here is the constrained spherical deconvolution (CSD) (Tournier, Calamante et al. 2004, Tournier, Calamante et al. 2007).

#### **Constrained Spherical Deconvolution**

CSD assumes that white matter fiber bundles in the brain have similar diffusion profiles (Tournier, Calamante et al. 2004) or diffusion PDFs. Additionally, it also accounts for partial volume effects similar to the multi-tensor model.

Let us consider a fiber oriented along the z-direction, giving rise to maximum diffusivity along that direction. The diffusion profile corresponding to that fiber would be a flat disc in the x-y plane, as there is low diffusivity and little attenuation of signal in the plane perpendicular to the fiber orientation. The response function of a fiber oriented along  $(\theta, \phi)$  is defined as the sum of the diffusion signal intensities perpendicular to  $(\theta, \phi)$ . Therefore, the response function of the fiber in our example would have a maximum along the z-direction and a minimum in the x-y plane, with values in between along other orientations. Figure 1.15 shows the response function (B) corresponding to a single fiber along the z-direction. This response function is radially symmetric, that is, it has a maximum at both +z and -z. The diffusion profile from which this response function was calculated is shown in (A).

If we assume that, there are multiple fibers oriented along directions  $(\theta_i, \phi_i)$  and the axially symmetric response function of a fiber aligned along the z-direction is represented by  $R(\theta)$ ; the observed MR signal from a voxel  $S(\theta, \phi)$  is the sum of independent signal contribution from each of the fiber bundles (Tournier, Calamante et al. 2004).

$$S(\theta, \phi) = \sum_i f_i \hat{A}_i R(\theta)$$

Here  $\hat{A}_i R(\theta)$  rotates the response function  $R(\theta)$  such that it is oriented along the direction of the  $i^{\text{th}}$  fiber  $(\theta_i, \phi_i)$  with volume fraction  $f_i$ .

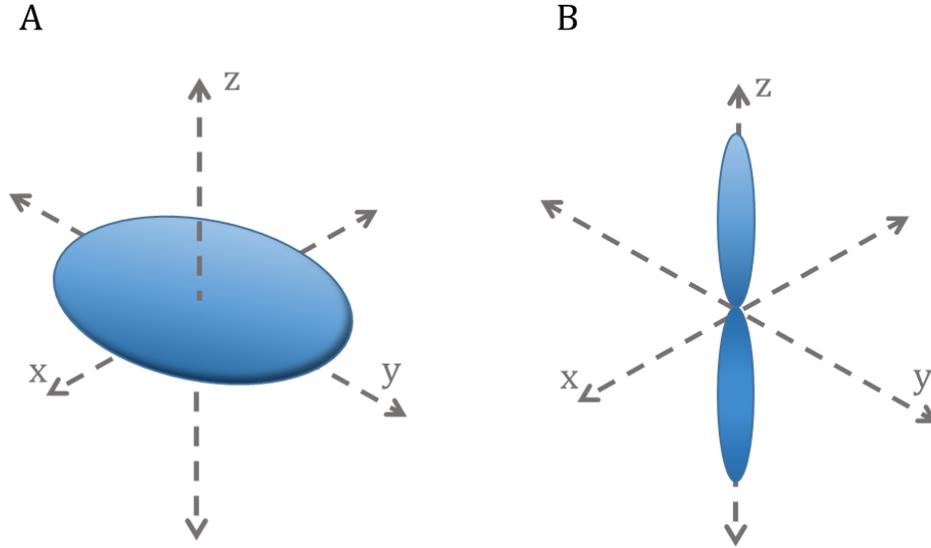


Figure 1.15: The diffusion signal profile of a single fiber oriented along the  $z$ -direction is shown in (A). The corresponding response function is shown in (B).

The measured signal over the surface of a sphere can also be expressed in terms of a convolution of the response function with the fiber orientation distribution (FOD) function given by  $F(\theta, \phi)$ .

$$S(\theta, \phi) = F(\theta, \phi) * R(\theta)$$

(1-7)

The fiber orientation distribution (FOD) is a continuous function of  $(\theta, \phi)$  that gives the fraction of fibers within a voxel that are aligned along the direction  $(\theta_i, \phi_i)$ . In other words, FOD is the probability distribution of partial volumes of fibers in a voxel as a function of direction (Raffelt, Tournier et al. 2012).

Figure 1.16 shows the convolution of the response function with the FOD corresponding to a voxel with only two fibers, oriented along the two directions pointed by the sticks. The FOD therefore is delta functions oriented along the two directions. The observed signal in the voxel is the convolution of the delta functions with the response function.

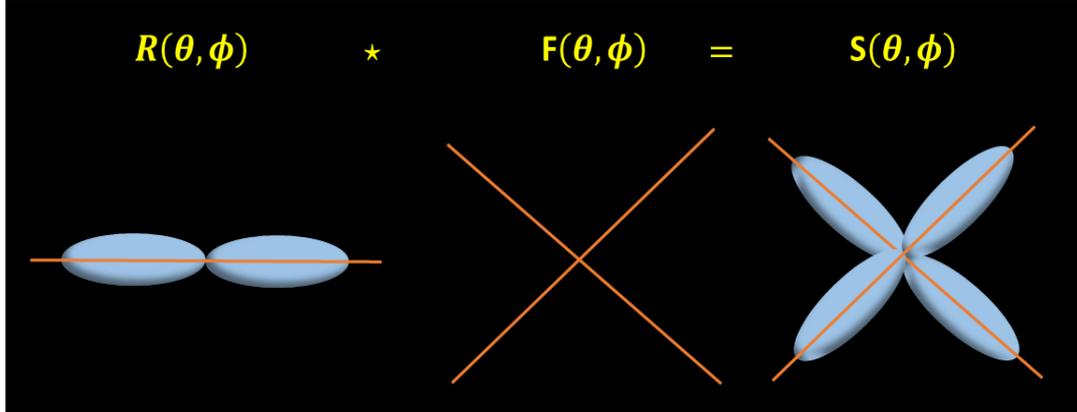


Figure 1.16: Observed signal is the Spherical Deconvolution of the response function with the FOD over the surface of a sphere.

From equation (1-7), if signal  $S(\theta, \phi)$  is measured and if somehow, the response function can be estimated, the FOD can simply be obtained by the spherical deconvolution (SD) of  $R(\theta)$  from  $S(\theta, \phi)$ . The spherical deconvolution can be performed by a simple multiplication in the spherical harmonic basis (Healy, Hendriks, & Kim, 1998). Spherical harmonic (SH) functions form an orthonormal basis over the surface of a unit sphere. If  $F_n$  and  $R_n$  are the  $n^{\text{th}}$  order spherical decomposition of  $F(\theta, \phi)$  and rotational harmonic decomposition of  $R(\theta)$  respectively, then the  $n^{\text{th}}$  order spherical harmonic decomposition of signal  $S(\theta, \phi)$  is given by:

$$S_n = R_n F_n$$

(1-8)

By inverting each rotational decomposition, one can recover  $F_n$ . As is the case with deconvolution, the presence of noise will produce erroneous results, as a true inverse is no longer feasible. In addition, noise can introduce spurious negative lobes in the FOD estimates that are not physically feasible, as a compartment cannot have negative volume fraction. To reduce the susceptibility of SD to noise, high frequency angular components can be filtered out. This filtered SD leads to loss of angular resolution. SD can also be constrained to ensure the FODs only have positive values (Tournier, Calamante et al. 2007), which in turn would reduce noise. This approach is referred to as the Constrained Spherical Deconvolution (CSD).

The FOD estimation is posed as an optimization problem where noise is minimized by imposing a large penalty on the negative values of FOD using a modified Tikhonov regularization (Hansen 1994).

$$F_{i+1} = \arg \min \{ \|QRF_i - S\|^2 + \lambda^2 \|LF_i\|^2 \}$$

The first term fits the result of equation (1-8) to the original signal using a least squares fit. Q is the transformation from the SH basis to the signal intensities. The second term imposes a penalty on FOD coefficients with signal intensities less than a set threshold.

Let  $F_i$  be the spherical harmonic coefficients corresponding to the current estimate of the FOD. For CSD, the initial estimate of the FOD is obtained using filtered SD and  $F_0$  is set to zero. A transformation matrix P applied to  $F_i$  provides the diffusion intensities ‘u’ along a set of pre-defined orientations (Tournier, Calamante et al. 2007).

$$u = PF_i$$

Instead of setting the negative intensities from the current FOD to zero, a threshold  $\tau$  is set to identify orientations along which  $u < \tau$ . Those coefficients from the transformation map P are retained in a constraint matrix L for each iteration as shown below:

$$L_{m,n} = \begin{cases} P_{m,n} & u_m < \tau \\ 0 & u_m \geq \tau \end{cases}$$

The constraint matrix L transforms the current estimate of FOD to a set of orientations along which the FOD is assumed to have a zero amplitude. The iterations continue until there is no further change in the L matrix.

### **Response function estimation**

Several approaches have been proposed to estimate the response function from the given diffusion data (Tax, Jeurissen et al. 2014, Jeurissen, Tournier et al. 2014, Tournier, Calamante et al. 2013). The algorithm for one such approach used in MRtrix (Tournier, Calamante et al. 2012) to implement CSD is outlined here:

- Calculate an initial response function  $R(\theta)$ . This is done by selecting voxels that have a high probability of containing single fiber population and using them to obtain an initial estimate.
- The diffusion-weighted images with a set of amplitudes along the different orientations are decomposed to their spherical harmonic (SH) representation using a least squares fitting. As the signal attenuation profile is real, the program assumes conjugate symmetry in the SH representation. Antipodal symmetry implies that all odd components of the spherical harmonics (SH) are zero and only even components need to be computed.

$$S(x) = S(-x)$$

- Non-negativity constrained spherical deconvolution is performed for all the voxels.

$$S_l = R_l f_l$$

Here  $l$  is the order of the SH representation,  $S$  is the diffusion signal and  $R$  is the response function. Using a matrix inversion, spherical deconvolution is performed to give the FOD  $f$ .

- The next step identifies fibers with a single fiber population using a ratio of the tallest and the second tallest FOD peaks. If  $A_1$  and  $A_2$  represent the peak amplitude values corresponding to the first and the second tallest lobes of an FOD, the following computation is used to identify the ratio.

$$\sqrt{|A_1|} * \left(1 - \frac{|A_2|}{|A_1|}\right)^2$$

These values are sorted and a user-defined number of voxels with the highest ratio are selected. This forms the initial set used in the calculation of a new response function.

- Using the new response function, CSD calculates a new FOD. The ratio calculations are repeated for all voxels and if the same set of voxels as in the initial set are selected, we have the correct single fiber population voxels. If the voxels change between iterations, a mask of the top 3000 voxels with the highest first peak to second peak ratio is selected and the process is repeated again.

This iterative process stops when the selection of voxels with single fiber population do not change between iterations or when a fixed maximum number of iterations have been reached.

The FOD estimates obtained from CSD for every voxel are overlaid on a zoomed in version of the FA map in Figure 1.17. The corresponding diffusion tensor estimates for the same region is presented for comparison. It is clear that the FODs present a better alternative to resolve regions of crossing fibers/multiple fiber. Tournier et al. (Tournier, Calamante et al. 2007) show that at higher b-values, CSD can estimate the white matter orientation to within 3.5 degrees of accuracy.

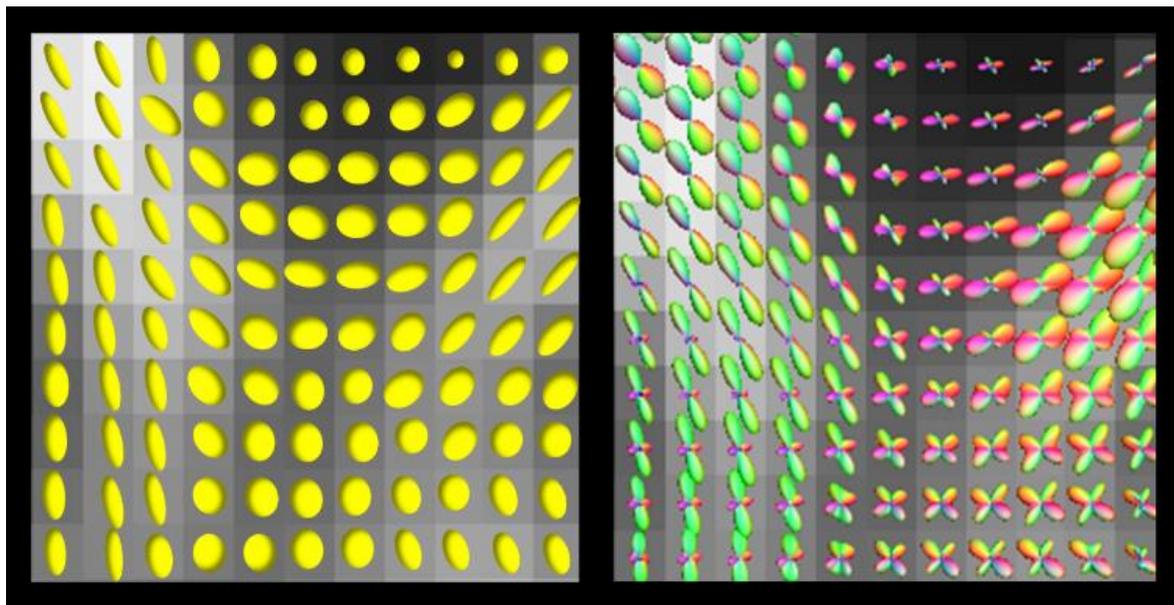


*Figure 1.17: Diffusion tensors (left) and fiber orientation distributions corresponding to each voxel (right) are overlaid on a fractional anisotropy map. In the region of crossing fibers, the diffusion tensors are oblate, whereas the fiber orientation distributions show two distinct lobes with different colors. The colors correspond to the direction of the underlying fiber.*

## 1.5 Fiber Tractography

Fiber tractography is an in-vivo visualization of the white matter connectivity in the brain using diffusion-weighted images (Basser, Pajevic et al. 2000). We have already seen that the orientation of white matter bundles in a voxel can be approximately estimated by the primary eigenvector in DTI and the FOD peaks in CSD. Tracts can be generated by simply piecing together the estimates of fiber orientation in each voxel (Feldman, Yeatman et al. 2010). This can be performed either on the entire brain or between user-defined regions of interests (ROI). The next sub-sections describe the two different types of tractography – deterministic and probabilistic.

### 1.5.1 Deterministic Tractography

In deterministic tractography, at every voxel, only a single decision is made regarding the primary direction along which the tract is believed to propagate. After making a unit step along that direction, this decision is repeated until a voxel is encountered that can no longer be in the tract, at which point the tracts are terminated. In the DTI based deterministic tractography algorithms, the decision on tract direction is based on the primary eigenvector  $v_1$  of the underlying voxel (Mori, van Zijl 2002). (Mori, Zhang 2006) show that tract propagation is equivalent to solving the PDE:

$$\frac{d}{ds}r(s) = v_1(r(s)); r(0) = r_0$$

The starting position is  $r_0$  and  $r(s)$  is the position along a curve. CSD based tractography algorithms follow the FOD peak orientation closest to the current direction of tracking using a Newton-Raphson gradient ascent algorithm modified to operate over a sphere (Tournier, Calamante et al. 2012).

### 1.5.2 Probabilistic Tractography

Probabilistic algorithms take into account the uncertainty in the orientation of axonal bundles at each step. Figure 1.18 illustrates the uncertainty associated with estimating the primary orientations of a fiber from the DTI model. There is little uncertainty in the WM tensor whereas the uncertainty is high in the case of GM or CSF.

Instead of a single decision, probabilistic tractography generates multiple streamlines at each step where the decisions for the next direction are drawn from random sampling of the underlying distribution of orientations. Each individual streamline propagation is similar to the deterministic approach. In DTI based probabilistic tractography, these samples can be chosen using rejection sampling or can be pre-computed before tracking (Behrens, Woolrich et al. 2003, Behrens, Berg et al. 2007). Sampling is usually restricted to directions within a certain angle of the current orientation of tracking. A sample is selected if it lies within a set curvature threshold. If not, a new sample is selected that meets the criteria. This process is repeated until a user specified number of samples have been generated.

In the CSD based probabilistic tractography, direction for subsequent steps are determined by sampling the underlying FOD in a voxel and choosing the direction with the highest probability. This corresponds to the direction with the largest FOD amplitudes.

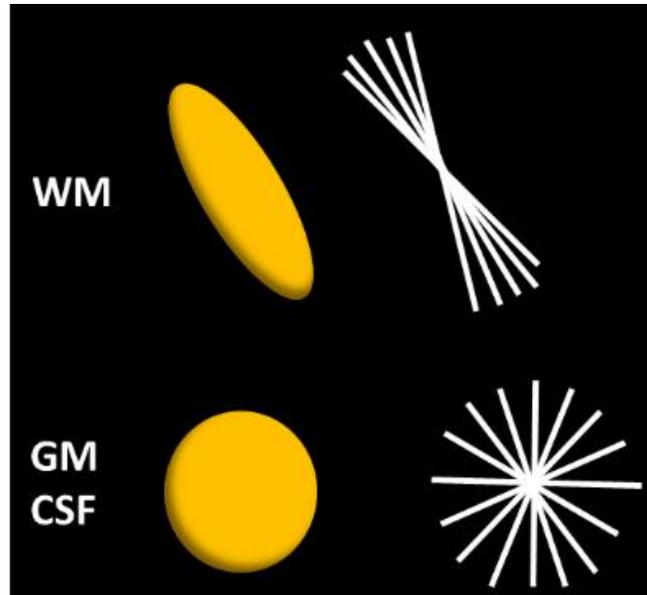


*Figure 1.18: Diffusion tensors that approximately describe diffusion in a white matter voxel and a gray matter/CSF voxel are shown. The uncertainty in the direction of the fiber is illustrated next to the tensors.*

A fixed step size has been shown to cause overshoot in regions of curvature and can be mitigated by employing a variable step size that steps along an arc, tangential to the current direction of tracking. This technique, called iFOD2 (Tournier, Calamante et al. 2010), decides on the next direction using the joint probability of current FOD and the FOD along the tangent path.

Tractography algorithms are usually terminated based on existing knowledge of anatomy, using any of the following approaches: termination masks such that as soon as a step is made into the masked region, tracking is stopped; user specified FA thresholds; curvature threshold to ensure smoothness and avoid bending of tracts and gray matter-white matter interface. Other constraints that are used to guide tractography include the step size, initial FA values to initiate tracks from seed voxels, etc.

### 1.5.3 Quantitative Analysis using Tractography

Studies have shown a high correlation between in-vivo tractography results and tracer studies on animals or post-mortem dissections on human brains (Catani, Thiebaut de Schotten et al. 2008, Thiebaut de Schotten, M. et al. 2012). However, one must be cautious in interpreting the results of tractography. The Figure 1.19 illustrates possible ways in which two distinct fiber bundles can be

oriented within a voxel. The fibers could be parallel to each other, crossing each other at a certain angle, merely kissing or bending within a voxel. The diffusion tensors and the FODs corresponding to each possibility are also shown. Crossing, kissing and bent fibers would result in the similar diffusion signal profile and hence similar tensor and FODs.

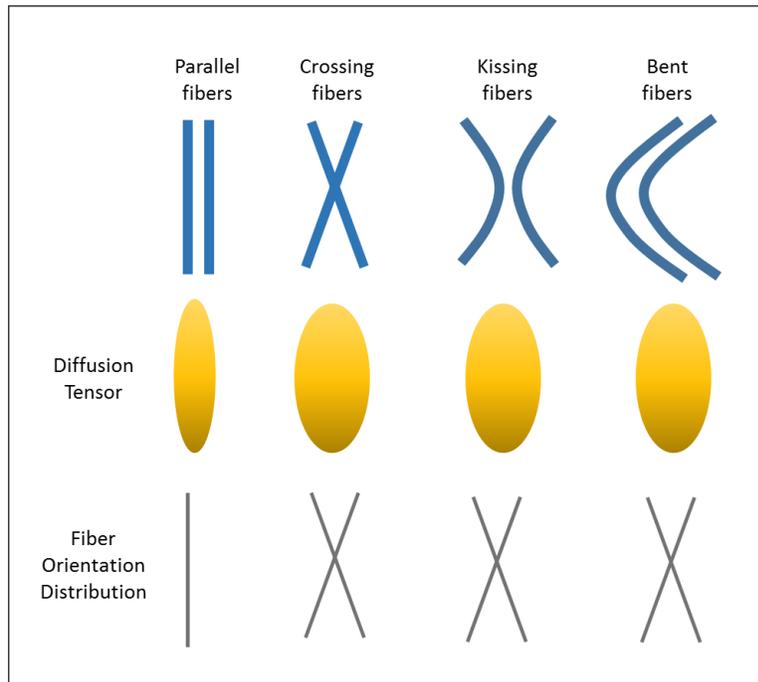


*Figure 1.19: An illustration of the possible orientations of two fibers within a voxel in the top row with the corresponding reconstructed diffusion tensor and fiber orientation distribution. With complex fiber orientations, such as kissing or bent fibers, the two techniques struggle to identify the underlying orientation correctly*

What tractography tells us is the direction of macroscopic diffusion pathways, which may or may not coincide with the location or direction at the level of the individual axons. Tractography algorithms are prone to errors in mapping the diffusion profiles to axonal geometry and are difficult to analyze quantitatively. However, they do have their own benefits, in that they are non-invasive and can provide a picture of the inner complex structures of the human brain.

Some of the widely used parameters to perform quantitative analysis across subjects using tractography include:

- Number of tracts connecting two regions of interest
- FA, AD and RD along the tracts
- Volume fraction of fiber tracts in a voxel (Axonal packing)

Confounding factors such as axon diameter, inter-axonal spacing, myelination, membrane permeability, number of fiber crossing and partial volume effects and the type of reconstruction algorithm influence the parameters described above. Studies have shown that almost 90% of the voxels in the brain white matter have crossing fibers (Jeurissen, Tournier et al. 2014). As such using a DTI model might produce erroneous results.

## 1.6 Assessing Age-related Decline in Amygdala-Orbitofrontal interactions

Cognitive aging is known to cause dysfunction of prefrontal cortical circuits, especially the orbitofrontal cortex (OFC), a gray matter region that is involved in decision-making (Gazzaley, Cooney et al. 2005). Research studies on humans and animals alike have shown that with age, both exhibit deficits on tasks that rely on orbitofrontal cortex (OFC) (Resnick , Lamar, & Driscoll, 2007) (Lai, Killany, Rosene, & Herndon, 1995) (Voytko 1999). OFC has been known to assign values (reward/punishment) to stimuli i.e. if a stimulus is deemed beneficial, it is considered a reward. The amygdala, a crucial part of the limbic system, stores these reward-value associations, shaping the response to a stimulus. In case of a reward devaluation, that is, a previously desired stimulus is no longer coveted; amygdala assesses the significance of the new value, updates previously stored associations and facilitates the OFC in making reward-guided decisions (Ghashghaei, Hilgetag et al. 2007). A pictorial representation of how the amygdala is believed to interact with the OFC is presented in Figure 1.20.

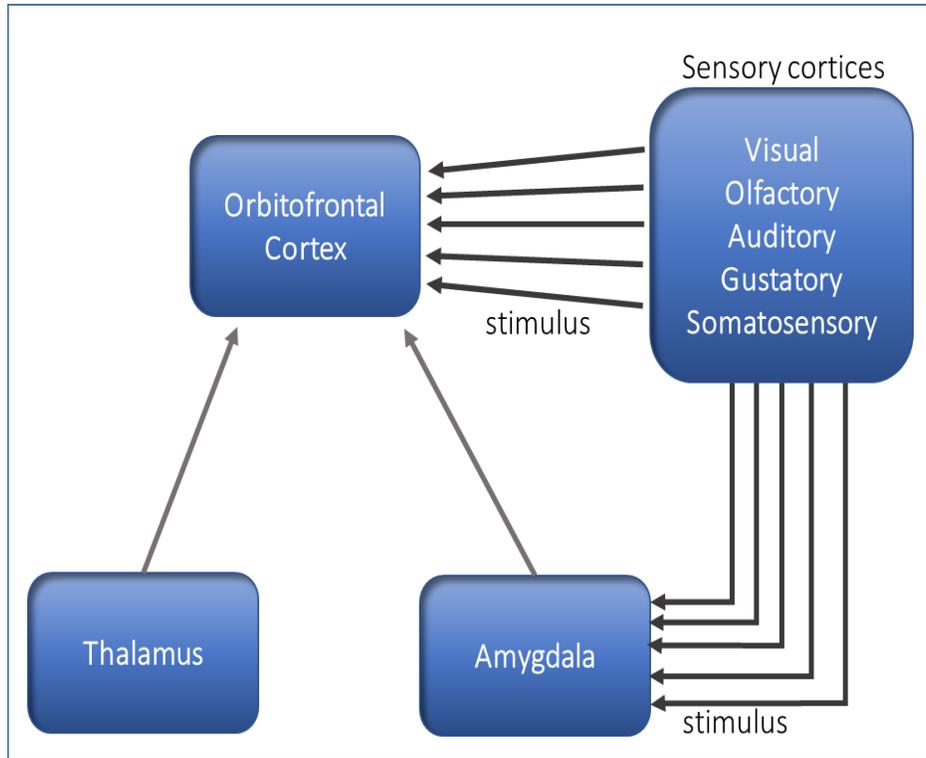


*Figure 1.20: A predicted model of interactions between the orbitofrontal cortex and Amygdala*

The amygdala is one of the highly connected regions of the human brain and consists of several nuclei. For the purpose of our study, the basolateral (BL) and the basomedial (BM) nuclei are grouped together and called basolateral amygdala (BLA) (Burke, Thome et al. 2014). The primary white matter pathway between the OFC and the BLA is known as uncinate fasciculus (UF). The UF has been implicated in value assignment and control behavior in reversal learning and learning from feedback (Gaffan, Wilson 2008, Catani, Mesulam 2008) . The bi-directional nature of UF ensures information flow between OFC and BLA stays up-to-date and reflects the current reward and punishment associations. It is believed that the strength of this UF connectivity changes with aging and affects reward-value assignment and feedback learning in older adults as shown in a study (Cook, Bookheimer et al. 2007) where older adults performed poorly in a working memory test.

### 1.6.1 Primate Models: An Alternative to Human Imaging Studies

Animal models are commonly used in the research community to investigate the structural and functional workings of brain. Research finding on primate brains have been shown to correlate well with those on humans (Thiebaut de Schotten, M. et al. 2012). Of these, the rhesus macaques (*macaca mulatta*) and bonnet macaques (*macaca radiata*) monkeys have been used in a number of studies, including those to understand the pathways for emotion (Ghashghaei, Barbas 2002), changes to frontal connections and cognitive changes in aging brain (Makris, Papadimitriou et al. 2007) and lesions. Tracer studies on rhesus macaque monkeys reveal striking similarities in the axonal organization with humans (Thiebaut de Schotten, M. et al. 2012). The monkeys are usually trained on specific tasks under proper experimental conditions and their responses to a wide variety of stimuli are tested. Imaging is performed to assess the structural and functional integrity of the brain, and to correlate the behavioral performances with parameters that can be extracted from imaging. Monkeys age at approximately 3 times the rate of humans.

### 1.6.2 Motivation for Current Work

In a previous study by Sara Burke et al (Burke, Thome et al. 2014), the performance of a group of young and aged bonnet macaque monkeys was assessed on a reward devaluation (RD) task; a task that specifically assesses the integrity of OFC-amygdala functional connections. The monkeys were tested on their ability to choose the optimal food reward by accounting for stimulus information provided to them. The study reported a decline in OFC volume with age, correlating with performance of the monkeys on the RD task such that the older monkeys performed poorly compared to the young ones. The basolateral amygdala (BLA) volume, however, did not change with age, nor correlate with their performance. This study looked at the structural changes in the gray matter volumes corresponding to the OFC and the BLA. The functional connectivity was tested using behavioral tests. An alternate is to look at how strong the white matter pathways connecting the two regions of interests are, in particular, the uncinate fasciculus connectivity.

### 1.6.3 Thesis Objective

The objective of this thesis is to make quantitative assessment of age-related white matter connectivity differences between OFC and amygdala in young and aged bonnet macaques using Diffusion MRI. The integrity of the UF pathway is evaluated using high angular resolution diffusion imaging along with anatomical T1- and T2-weighted imaging. A group of 11 healthy

adult female bonnet macaque monkeys, ranging from 11 years to 30 years of age (mature to old bonnet monkeys), were imaged. Prior to imaging, the bonnet macaque monkeys were also tested on a Wisconsin General Test Apparatus on working memory task, reversal-learning task, delay-no-match-to sample task with interference in the lab of Dr. Carol Barnes. A detailed description of these tasks is available in (Gray, Smith et al. 2016).

Chapter 2 presents the image-acquisition protocol used in acquiring the diffusion-weighted images and outlines an image-processing pipeline employed to remove any imaging-related artifacts. A diffusion PDF is reconstructed from the processed images using the DTI and the CSD based methods. Probabilistic tractography is performed using a multi-tensor and iFOD2 based techniques.

Chapter 3 presents the results of tractography where uncinate fasciculus is delineated and imaging parameters of interests that reflect the underlying characteristics of the white matter tract are extracted along the length of the tract. These include the FA, AD, RD and the number of tracts that belong to UF. These imaging parameters, indicative of WM integrity, are then analyzed with respect to the behavioral performance measures to study the relationship, if any, between the performance of the monkeys on cognitive tasks and the measured WM integrity.

## Chapter 2 MR Image Acquisition, Processing and Fiber Tractography

Chapter 2 presents an overview of the data acquisition protocol and an image-processing pipeline to ensure the acquired raw MR images are free from diffusion imaging related artifacts prior to the estimation of the diffusion PDF. The pre-processing also ensures that the images are suitable for any statistical analysis. Section 1 describes the MRI acquisition protocol used in imaging bonnet macaque monkeys. Section 2 introduces the different types of distortions present in diffusion-weighted images and the methods to correct them. The significance of noise removal in diffusion-weighted images, with a discussion of a local principal component analysis (LPCA) based approach to filter the images is also presented. Section 4 highlights the image processing necessary to visualize the images from a low-resolution diffusion space in a high-resolution anatomical space. The last two sections explain the methods for diffusion PDF reconstruction and the requisites for fiber tractography; including identification of regions of interest for tract propagation and constraint parameters for the tract termination.

### 2.1 Image Acquisition Protocol

All MRI images were acquired on a 3T GE (General Electric, Milwaukee, WI) Signa scanner. A body coil was used for the radio frequency excitation and a commercial eight-channel head coil was used for reception. The monkeys were imaged in a “*Sphinx*” position, placed in a customized MRI-compatible stereotactic head holder with mouth, orbit and ear bars within the receiver coil. A vitamin-E capsule was placed near the right ear of the monkeys to be able to differentiate the right side of the image from the left. Prior to imaging, each monkey was anaesthetized with an intramuscular injection and was given an intravenous catheter for fluids and intubation as described in (Burke et al., 2014). This ensured that there was no subject motion during the imaging. A T2-weighted reference scan of the whole brain was performed using a fast spin echo (FSE) sequence with the following parameters: TR = 3916.66 ms, TE = 73.8 ms, flip angle = 90°, slice thickness = 1.4 mm, in-plane resolution = 0.7 mm × 0.7 mm, acquisition matrix = 256 × 256 (FOV = 179 mm × 179 mm) with 4 repetitions of 47 continuous coronal slices. Diffusion-weighted images were acquired using a single shot echo planar imaging (SS-EPI) sequence with the

following parameters: TR = 12500 ms, TE = 71.8 ms, flip angle = 90°, number of averages = 2, 47 coronal slices to cover the entire brain, slice thickness = 1.4 mm, slice gap = 1.4 mm, in-plane resolution = 1.4 × 1.4 mm, and acquisition matrix = 128 × 128 (FOV = 179 mm × 179 mm). The data was acquired over 51 diffusion directions in a HARDI sampling scheme over a single shell with a b-value of 1000 s/mm<sup>2</sup>. Six volumes with no diffusion weighting (b=0 s/mm<sup>2</sup>) were also acquired.

High-resolution anatomical whole brain T1-weighted images were acquired with a 3D inversion-recovery prepped spoiled gradient-echo sequence (MP-RAGE) with the following imaging parameters: TR = 8.1 ms, TE = 3.3 ms, TI = 500 ms, flip angle = 20°, acquisition matrix = 256 × 256 (FOV = 15.4 mm × 15.4 mm), in-plane resolution = 0.7 mm × 0.7 mm and slice thickness = 0.7 mm with two repetitions of 86–100 coronal slices depending on the brain size. A sagittal cross section of a bonnet monkey brain is shown in Figure 2.1. The high-resolution anatomical T1-weighted, T2-weighted and the low-resolution diffusion weighted B0 (b=0 s/mm<sup>2</sup>) images are shown along with the acquisition matrix size and the number of slices.

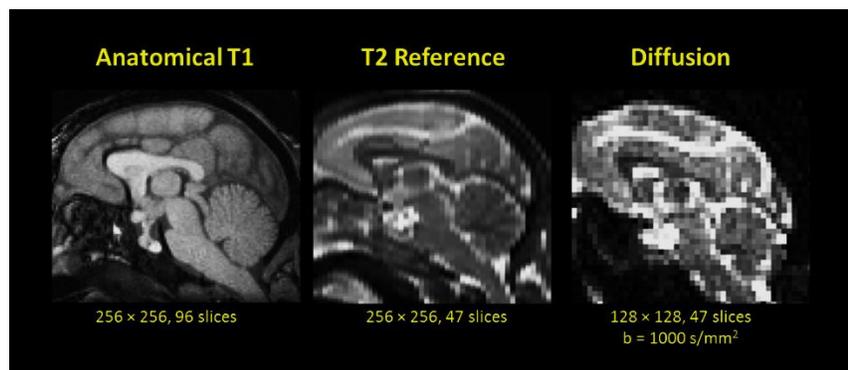


*Figure 2.1: A sagittal slice of a Bonnet monkey corresponding to the T1-, T2- and Diffusion-weighted images.*

### 2.1.1 DICOM to NIFTI Conversion

The DICOM (Digital Imaging and Communications in Medicine) images obtained from the scanner are converted to the NIFTI (Neuroimaging Informatics Technology Initiative) format using the DICOM2NII tool (Rorden). The output of this conversion process results in a four dimensional NIFTI file where the fourth dimension corresponds to the diffusion directions. The diffusion-weighted MR images have a low in-plane resolution of 1.4 mm compared to the 0.7 mm

anatomical T1-weighted images. In addition, the presence of noise and distortions make these images unfit for registration with either the T2-weighted or the T1-weighted images.

## 2.2 Distortion Correction

The EPI acquisition strategy traverses the entire k-space in a single shot in a serpentine manner; making the DWI images more susceptible to diffusion related artifacts. The slow data acquisition along the phase encode (PE) direction and phase accumulation during readout causes a geometric shift in image space along the PE axis (Sutton 2009, Andersson, Sotiropoulos 2016). Other distortions include susceptibility induced field in-homogeneity and acquisition noise. The objective of the distortion correction process is to ensure the DWI data is as close to the original object as possible. This is achieved by the estimation of a distortion map using image registration techniques and correcting for it. The technique used in this work was a Gaussian Process (GP) based correction for eddy currents and a b-spline based correction for susceptibility-induced distortions.

### 2.2.1 Eddy Current Distortions

The strong diffusion-sensitizing gradients being rapidly turned on and off causes fluctuations in the background magnetic fields in the bore of the MRI magnet. Based on the Faraday-Lenz law, electrical currents or eddy currents are induced and the magnitude of the eddy currents depends on the rate of change of the magnetic field inducing the currents. Current in the conducting material, in turn, induces a magnetic field, creating an off-resonance condition. This phenomenon is referred to as eddy current (EC) induced off-resonance fields and is believed to cause in-plane shearing in the frequency encode direction, and scaling, zooms and translations along the PE direction (Haselgrove, Moore 1996, Jezzard, Barnett et al. 1998). These can cause spatial misalignment and blurring of the interface between gray matter and white matter, making it difficult to register with either T1- or T2-weighted images using conventional methods.

#### 2.2.1.1 Image Registration

In the absence of a bipolar pulsed gradient sequence, known to cancel eddy currents (Bodammer, Kaufmann et al. 2004, Reese, Heid et al. 2003), many studies retrospectively correct for spatial nonlinearities and phase shifts due to eddy currents in post-processing (Chan, von Deuster et al.

2014, Andersson, Sotiropoulos 2016). The simplest method involves registering the distorted diffusion image to a distortion-free target image. Image registration identifies a spatial transformation matrix or a deformation map  $T(\cdot)$  to map a voxel in a source/reference image to a voxel in the target/moving image using any of the standard interpolation techniques – nearest neighbor, trilinear interpolation, sinc or b-spline etc. A cost function  $C(\cdot)$  is associated with the transformation that measures either the degree of similarity or the differences between the target and the source image warped to the target image. When posed as an optimization problem, registration can be described as:

$$T^* = \arg \min_T C[Y - T(X)]$$

The optimal transformation map  $T^*$  minimizes or maximizes the cost function depending on the nature of cost function involved. For example, if the cost function measures differences between the images, the optimization routine would want to minimize the differences. Some commonly used metrics are sum of squared differences (SSD), correlation ratio (CR), mutual information (MI) etc. CR and MI depend on the relationship between the distributions of the image intensities (Viola, Wells III 1997, Roche, Malandain et al. 1998) and are more commonly used in inter-modal registrations such as registering a DWI to a T1-weighted or a T2-weighted image. A good choice for the target image are the DWI images acquired with no diffusion-sensitized gradients or the B0 images as these are unaffected by eddy currents. This relatively simple registration technique is based on the assumption that with a linear combination of gradients in the PE direction with an offset, one can adequately describe the EC-induced field.

### 2.2.1.2 *Gaussian Process based Eddy Current Distortion Correction*

Higher-order modelling of eddy currents such as a second-order or a third-order polynomial have been shown to perform significantly better than an affine registration model for HARDI data (Rohde, Barnett et al. 2004). Andersson et al. (Andersson, Sotiropoulos 2016) introduced an alternative optimization routine that iteratively registers individual diffusion volumes to a model free prediction of what each volume would look like in the absence of eddy currents. Each iteration is based on a Gaussian Process (Rasmussen 2006, Andersson, Sotiropoulos 2015) and compares the prediction to the observed signal. The error in estimation is used to estimate the deformation field.

Figure 2.2 shows two diffusion-weighted images corresponding to two diffusion orientations that are almost opposite to each other. As a result, the diffusion-weighted images appear similar in intensity but have EC induced distortions in the opposite directions. It is difficult to visualize eddy current distortions in an image, as the distortions are mostly translations between images. The top row shows the original EC-distorted images where subtle stretching is visible in the posterior regions of the brain in (A) and in the forebrain in (B). The bottom row shows the distortion-corrected images corresponding to the top row.

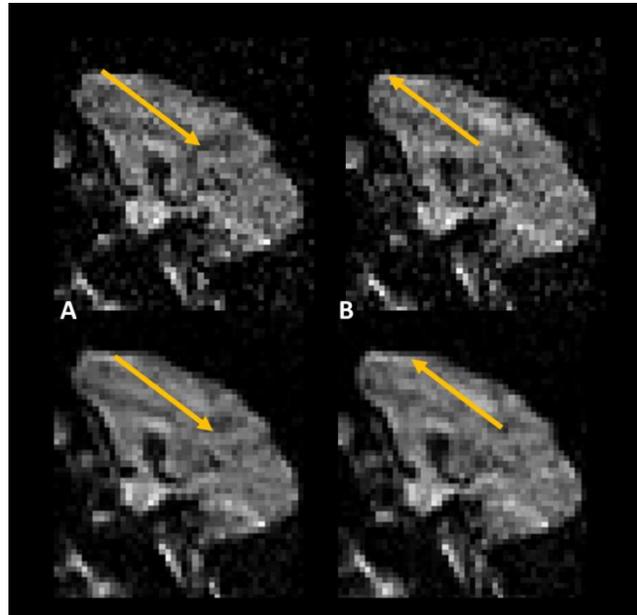


*Figure 2.2: Distortions due to eddy currents displayed on two images along opposite directions. The bottom row shows the distortion corrected images corresponding to the top row.*

The bottom row shows the distortion-corrected images corresponding to (A) and (B) where correction was performed using the Oxford Center for Functional MRI of the Brain's (FMRIB) diffusion toolbox (FSL) that implements the GP-based optimization routine described in (Andersson, Sotiropoulos 2015).

### 2.2.2 Susceptibility-induced Distortions

Maintaining a uniform main magnetic field in the field of view of image acquisition is essential to yield uniform signal intensity in the images. An object being imaged can have different magnetic susceptibilities based on the different constituents of the object. Depending on the magnetic

susceptibility of the tissue being scanned, the uniformity of the main magnetic field around the tissues as well as the air-tissue interface varies; this is referred to as magnetic field inhomogeneity. These susceptibility effects result in variations in the proton precession frequency; creating an off-resonance. A shift in Larmor frequency results in geometric distortions and spatial misalignment of MR signals; with signal loss in some areas and signal pile-up in others. The sensitivity of EPI sequence to off-resonance fields (Le Bihan, Poupon et al. 2006) makes it problematic to image regions near the air-tissue interface such as the orbitofrontal cortex and the amygdala; ones that we are particularly interested in this thesis.

The top row in Figure 2.3 shows diffusion-weighted images of coronal slices of a monkey brain along with the corresponding distortion-free T2-weighted images for reference. The first image shows visible distortions along the phase-encode direction, the superior-inferior direction in the image plane. The second image shows signal loss as well as signal pile-up near the air-tissue interface. It is important to note that any signal lost during image acquisition cannot be redeemed by any post processing techniques; only spatial distortions or misalignments can be corrected.

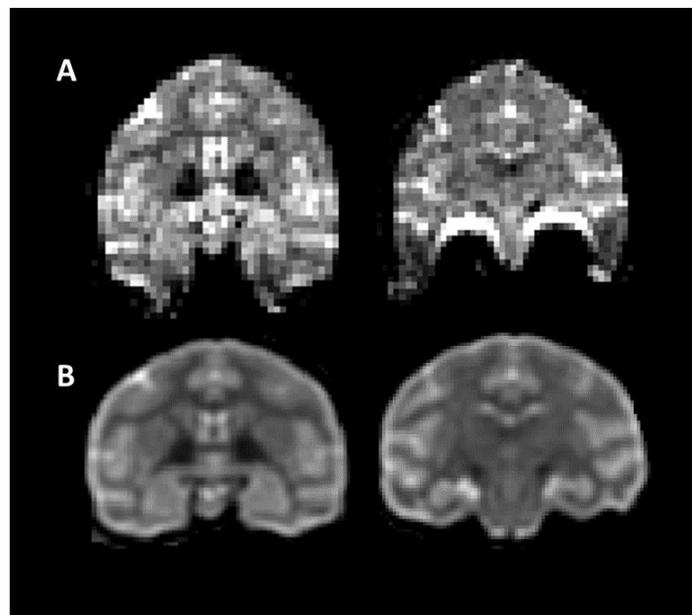


*Figure 2.3: Coronal slices of a monkey brain showing susceptibility-induced distortions in diffusion-weighted images (A) and distortion-free T2-weighted images (B)*

### 2.2.2.1 *Correcting Susceptibility-induced Distortions*

The distortions associated with magnetic field inhomogeneity can be retrospectively corrected by knowing how the main magnetic field varies as an object is imaged. The variation in the B0 field can be either collected as a B0 field map during image acquisition or estimated using a deformable registration to a reference T2-weighted image with b-splines. In the first technique, images are acquired at two different echo times and the difference in the phase of the images is used to estimate the field map (Jezzard, Balaban 1995). The second technique performs non-linear registration of the diffusion images to the reference T2-weighted images to create a deformation map with cubic b-splines. A deformable registration computes a non-linear (or higher order) spatial transformation between corresponding structures in two images. This spatial transformation, also known as a vector field or a deformation field, is applied to the reference image to map it to the target space. A comparative study of the field map based correction and the registration based approach shows that in the absence of a field-map, non-linear registration to the T2 images produces comparable results (Wu, Chang et al. 2008). The Tolerable Obsessive Registration and Tensor Optimization Indolent Software Ensemble (TORTOISE) (Pierpaoli, Walker et al. 2010, TORTOISE) toolbox is used to perform the non-linear registration using third order b-spline polynomials. In TORTOISE, the structural T2 input image is moved to the diffusion space by a rigid body registration to the first B0 image. A mutual information (MI) cost function is used to create this structural target for EPI distortion correction. The deformation field for EPI correction is then modelled in the diffusion space iteratively using cubic b-splines until the MI cost function is maximized. This optimization model assumes the distortion to be constrained along the PE direction. Once an optimal deformation field is obtained, it is applied to all diffusion-weighted images. The b-vectors associated with the original DWIs are rotated to reflect the applied deformation map (Leemans, Jones 2009). Figure 2.4 shows coronal slices of one of the bonnet brains with susceptibility induced distortions (A). There is visible stretching along the PE direction, which is along the superior-inferior direction in the image plane. After registering the DWI with the distortion free T2-weighted images (C) in TORTOISE, the distortions are visibly reduced as is evident in (B). There is still some residual distortion and signal loss near the air-tissue interfaces in the corrected images.

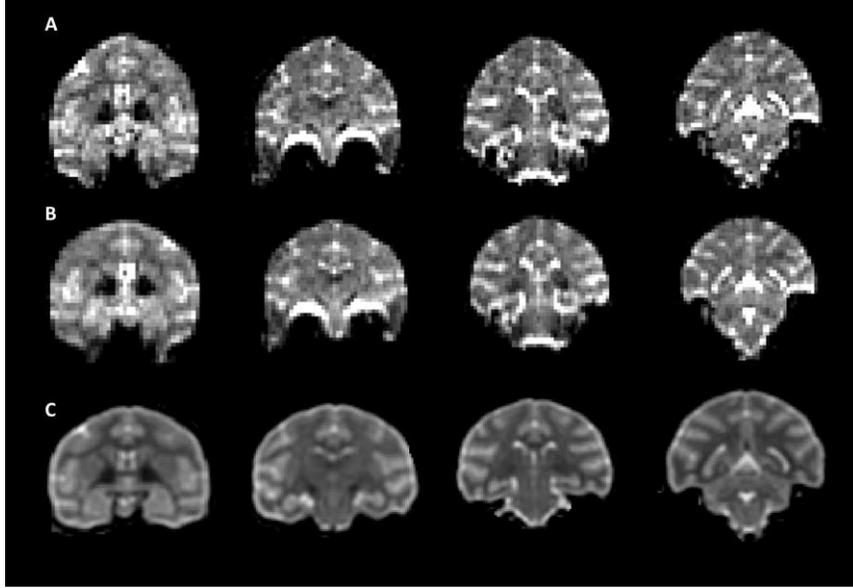


Figure 2.4: Coronal slices arranged from anterior to posterior slices of a monkey. (A) DW images with distortion along PE direction. Signal loss can be seen in the inferior regions of the brain. (B) Final results from TORTOISE after registering with distortion free T2-weighted images (C)

### 2.3 Bias Field Correction

Bias fields are intensity non-homogeneity resulting from spatial sensitivity of the receiver RF coils, resulting in a low frequency intensity variation on the otherwise uniform MR images. The bias field is more prominent at higher magnetic field strengths and can affect image analysis performed on the non-corrected data, including issues during the tissue segmentation processes or mis-registration. In a simplistic signal mode, the relationship between the original image  $u(x)$  and the image observed by the receiver coil  $g(x)$  is given by:

$$g(x) = u(x)f(x) + \eta(x)$$

Here,  $f(x)$  is the receiver coil sensitivity or the bias field and  $\eta(x)$  is Gaussian noise independent of the input image. In the absence of any noise, the equation above can be transformed to a log space and rewritten as:

$$\hat{g}(x) = \hat{u}(x) + \hat{f}(x)$$

$$\hat{g}(x) = \log[g(x)]$$

One can iteratively solve for the original image by estimating the bias field and obtaining the corrected image  $\hat{u}^n$  in the  $n^{\text{th}}$  iteration as described in (Sled, Zijdenbos et al. 1998):

$$\begin{aligned}\hat{u}^n &= \hat{g} - \hat{f}_e^n \\ \hat{f}_e^n &= \hat{g} - E[\hat{u}|\hat{u}^{n-1}] \\ \hat{u}^n &= \hat{g} - S\{\hat{g} - E[\hat{u}|\hat{u}^{n-1}]\}\end{aligned}$$

The estimate of the bias field  $\hat{f}_e$  based on a single measurement of  $g$  has been smoothed using a smoothing operator  $S$ . A variant of the above algorithm known as the N4ITK (Tustison, Gee 2009, Tustison, Avants et al. 2010) has been implemented in the Slicer 3D software (Fedorov, Beichel et al. 2012). Here, the corrected image is iteratively estimated using residual bias field  $\hat{f}_r$  instead of estimating the total bias field at the  $n^{\text{th}}$  iteration.

$$\begin{aligned}\hat{u}^n &= \hat{u}^{n-1} - \hat{f}_r^n \\ \hat{u}^n &= \hat{u}^{n-1} - S\{\hat{u}^{n-1} - E[\hat{u}|\hat{u}^{n-1}]\}\end{aligned}$$

All the T1-weighted images are corrected for bias fields using the Slicer 3D software (Slicer). A third order b-spline with grid resolution of [1,1,1], iterations [50,40,30] and convergence threshold of 0.0001 is used. Figure 2.5 shows original images (A and D), the bias fields that create a loss of signal intensity in the posterior regions of the brain (B and E) and the bias corrected images (C and F). Since the animals were placed in a sphinx position in a head coil, the receiver coil sensitivity drops towards the posterior regions of the brain resulting in signal loss. The bias field computed and corrected by the Slicer software results in more uniform signal intensity throughout the brain.

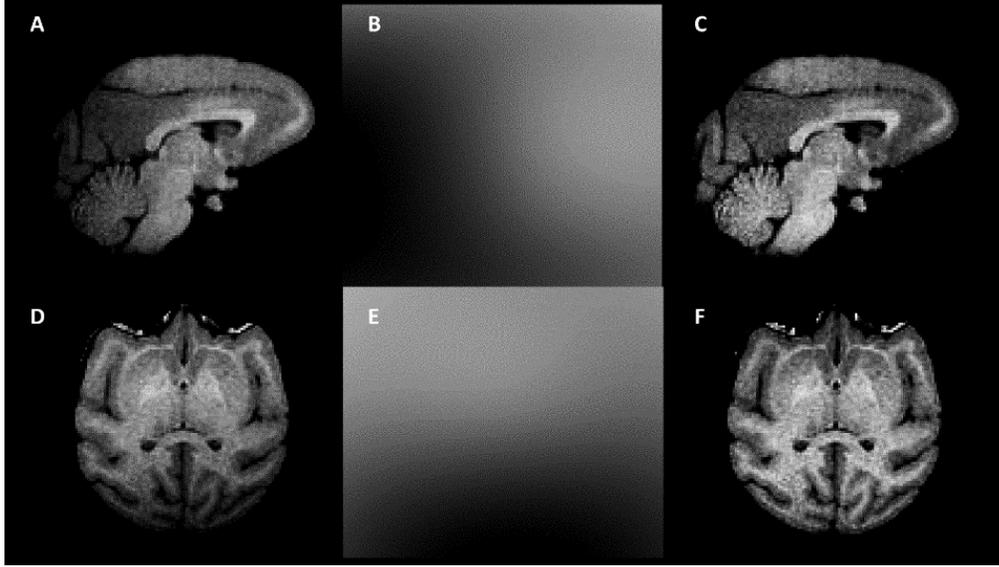


Figure 2.5: Non-bias corrected DW brain images showing sagittal (A) and axial (D) slices. (B) and (E) show the bias fields with inhomogeneity in the posterior regions of the brain, (C) and (F) are the bias corrected images corresponding to sagittal and axial slices respectively.

## 2.4 Noise Reduction in Diffusion MRI

The MR image acquisition in the scanner takes place in Fourier space where the signal detected in the real and imaginary channels of the coil are affected by independent and identically distributed additive white Gaussian noise of zero mean and a standard deviation given by  $\sigma$ . The signal observed from both channels are combined to form DICOM images using a sum of squares formulation.

$$|I_{observed}| = \sqrt{I_r^2 + I_i^2}$$

Here,  $I_r$  is the signal observed by the real channel of the coil (real part of MR data) and  $I_i$  is the signal observed by the imaginary channel of the receiver coil. The noise in the magnitude MR image now follows a Rician distribution. Because of the non-zero mean, the Rician noise introduces a bias in the measured MR signal affecting tensors or FOD shape and orientation (Basu, Fletcher et al. 2006). The signal variation in MR images along different orientations contain

valuable directional diffusion information. It is therefore important to filter any noise that might potentially bias parameters of interest.

Noise removal, or denoising, in diffusion MRI can be broadly classified into techniques that filter data in the image space such as Non-Local Means, Joint Linear Minimum Mean Square Estimations and total variation based denoising and those that filter the data in an alternate domain such as the wavelets or the principal component space. In this thesis, a local principal component analysis based noise removal technique is used.

#### 2.4.1 Overcomplete Local Principal Component Analysis based Denoising

Given a set of observations, principal component analysis (PCA) finds an orthogonal basis of eigenvectors of the data such that the eigenvector direction corresponding to the largest eigenvalue accounts for most of the variance in the data (Wold, Esbensen et al. 1987). The eigenvector corresponding to the second largest eigenvalue captures the second largest variance in the data and so on. The projection of the observations on the basis formed by the eigenvectors are the principal components of the data. It has been shown that using a small subset of ‘k’ basis vectors, corresponding to the first ‘k’ largest eigenvalues, such that  $k \ll N$ , the total number of eigenvectors; one can explain the original set of observations with good precision. This has led to widespread use of PCA in dimensionality reduction. Noise, with its high spatial variance, has a very low variance in the principal component space. The elimination of principal components with low variance therefore, has the desired effect of noise removal. The inherent sparsity in medical images make them ideal for a principal component analysis (PCA) based noise-filtering approach. Once the distortions associated with Echo planar imaging are corrected, an overcomplete local PCA based denoising scheme described in (Manjón, Coupé et al. 2013) to spatially filter the data is implemented.

Overcomplete local PCA performs denoising as a two-step process. In the first step, a global PCA decomposition is performed on the no diffusion-weighted images (B0 images) for noise estimation. This is because the B0 images have a higher signal to noise ratio than the diffusion-weighted images. The B0 images are transformed to the principal component space where the principal component associated with the smallest eigenvalue is considered noise. Noise standard deviation is calculated from a sliding 3D block on the principal component corresponding to noise and a correction factor for the Rician noise model is introduced as described in (Manjón, Coupé et al.

2013, Koay, Basser 2006). A noise map is obtained by low pass filtering the standard deviation map, which in turn, yields a threshold value to be used subsequently in the next step.

In the second step, principal component decomposition is performed on localized 4D blocks of the diffusion-weighted image such that the fourth dimension consists of 3D volumes acquired using different orientations of the diffusion gradient. The PCA decomposition yields a set of eigenvalues and eigenvectors for each small spatial block. Within a spatial block, any eigenvalue that is less than the threshold from the noise map corresponding to the voxel in the center of the block is set to zero. Inverse transformation takes the principal components back to the image space where the effect of filtering can be seen. The use of a sliding block leads to multiple estimates of denoising for a given voxel. These estimates are combined using a weighted approach where more weight is assigned to a PCA decomposition that retains fewer principal components after filtering.

An alternate denoising method based on filtering the PCA components spatially and along the different diffusion directions has been developed as part of this thesis. The details of this algorithm are presented in Appendix A.

#### 2.4.2 Noise Filtering the Bonnet Diffusion-weighted Images

The DWI images collected for the bonnet study were denoised using the MATLAB implementation of Overcomplete Local PCA algorithm. Figure 2.6 shows the sagittal and axial planes of a noisy DWI image (A and B) and the corresponding noise filtered image (C and D).

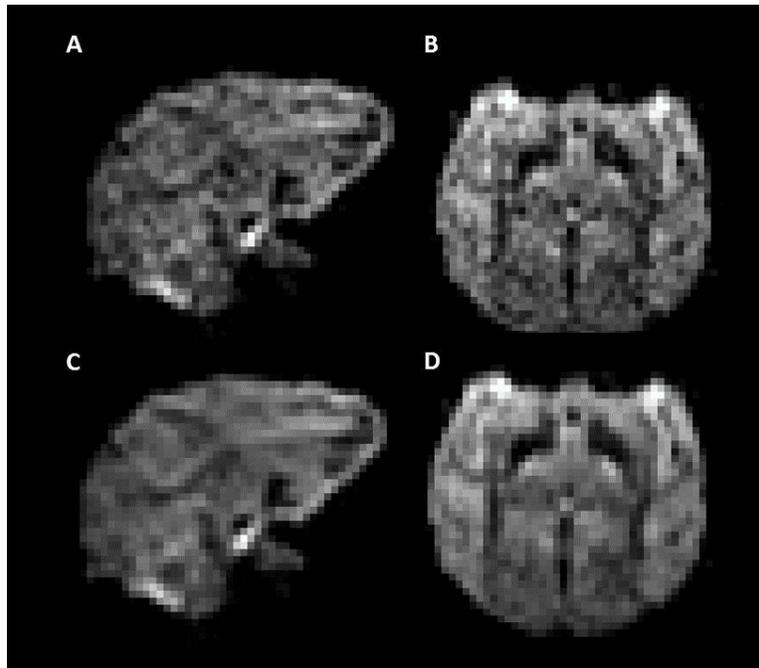


*Figure 2.6: Top row corresponds to noisy sagittal (A) and axial (B) slice of a macaque brain. Bottom row (C) and (D) show the denoised versions of the sagittal and axial slices respectively.*

## 2.5 Registration to High-resolution Anatomical Images

The ability to visualize diffusion MRI results in a high-resolution anatomical space makes it easier to overlay parameters of interest such as fractional anisotropy maps, fiber orientation distributions or the results from fiber tractography. This section describes the standard radiological display convention and a method to register the diffusion-weighted images to the high-resolution T1- or T2-weighted images.

### 2.5.1 Re-orientation of Images to Radiological Convention

The standard radiological convention to display medical images, also known as RAS, is: left to right along the x-direction, posterior to anterior along the y-direction and inferior to superior along the z-direction. The bonnets monkeys were imaged in the scanner in the sphinx position. As a result, the orientation of the acquired images was – left to right, superior to inferior and anterior to posterior. The vitamin-E capsule placed during imaging was used to differentiate the left side from

the right. In Figure 2.7, the original images (A) are in the orientation described above. The standard RAS convention is displayed in yellow on the images.

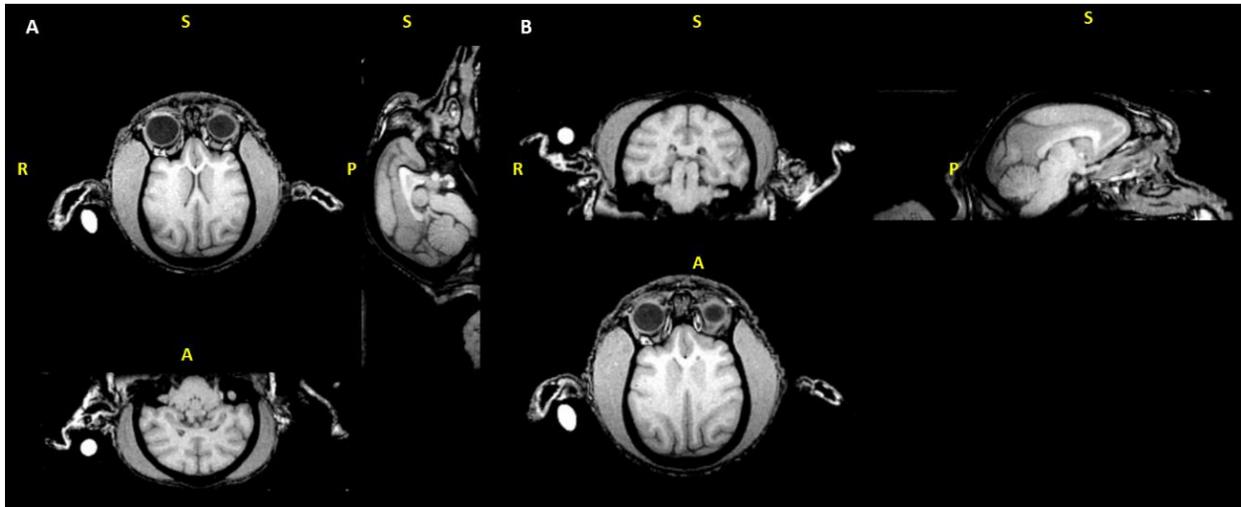


Figure 2.7: Original data (A) and images after re-orientation as per radiological convention (B). The labels on the images are Superior (S), Right (R), Anterior (A) and Posterior (P). The RAS convention is:  $x$  (Left to Right),  $y$  (Posterior to Anterior) and  $z$  (Superior to Inferior). The Vitamin-E capsule marking the right side of the animal is visible as a bright spot in the image outside the brain.

It is clear from Figure 2.7A that the anterior portion of the brain is where the superior region should be and the coronal slices of the image are along the  $z$ -direction, which should in fact go from inferior to the superior direction. The images were re-oriented to the RAS convention using the NIFTI toolbox in MATLAB (NIFTI). The corresponding b-vectors file was also reoriented to conform to the rotations used. The post-rotation image is shown in Figure 2.7B where the images are as per the standard convention and the axial slices are along the  $z$ -direction. The vitamin capsule appearing as the bright spot in the image continues to be on the right side of the image.

### 2.5.2 Registering Diffusion-weighted Images to T1-weighted Images

A simple rigid body registration of the diffusion-weighted images to the T1-weighted image, allowing six degrees of freedom (3 translations and 3 rotations), is sufficient when the distortions associated with echo-planar imaging are removed. Any higher order transformations such as affine or non-linear registration that require shears or non-linear deformations require re-orientation of the b-vectors.

FSL's diffusion toolbox (FDT) was used to register the DWI to T1-weighted image in a three-step process. In the first step, FMRIB's Automated Segmentation Tool (FAST) (Zhang, Brady et al. 2001) was used to segment out probabilistic maps of gray matter (GM), white matter (WM) and CSF from the brain extracted T1-weighted image. These are tissue probability masks where each voxel is assigned a probability to whether it is GM, WM or CSF. The sum of probabilities of all the tissue types in any voxel should add up to 1. The voxels with a probability of existence of WM greater than 0.5 are selected to be part of a binary mask to segment out WM in the T1 image. These segmented regions would be used in subsequent steps to register the white matter in the reference DWI image to the white matter in target T1-weighted image.

The second step, performed using FMRIB's Linear Image Registration Tool (FLIRT), pre-aligns the EPI image to the reference T1 brain by a rigid body registration with a correlation ratio cost function. This process results in an initial transformation matrix that when applied to the EPI volume roughly aligns it with the anatomical image. The aligned DWI acting as a good starting point for the next optimization routine, a Boundary Based Registration (BBR) algorithm (Greve, Fischl 2009) that makes use of the extracted white matter boundary. The diffusion signal intensity at a short distance from this segmented WM edge is chosen from either side of the boundary. This forms a pair of points with a set of diffusion signal intensities. The difference between the intensities at each pair of points is used to calculate the cost function. The BBR optimization routine aims to maximize the intensity difference between a pair of points. A fit is good when there is a large intensity difference between the two points, which is possible when one point is in the GM and the other is in the WM. The output transformation matrix from the BBR registration is applied to the EPI volume using a spline interpolation function.

Figure 2.8 shows the results of a boundary based registration scheme on a DWI volume. The reference high-resolution T1-weighted image (A) and the corresponding diffusion-weighted image in the T1-space (C) are shown along with a zoomed in area of the image in the yellow box across the two volumes. The edges of the WM extracted in the first step of the EPI registration process is overlaid on the two images (B and D) in red to show how it acts as a boundary between gray- and white-matter.

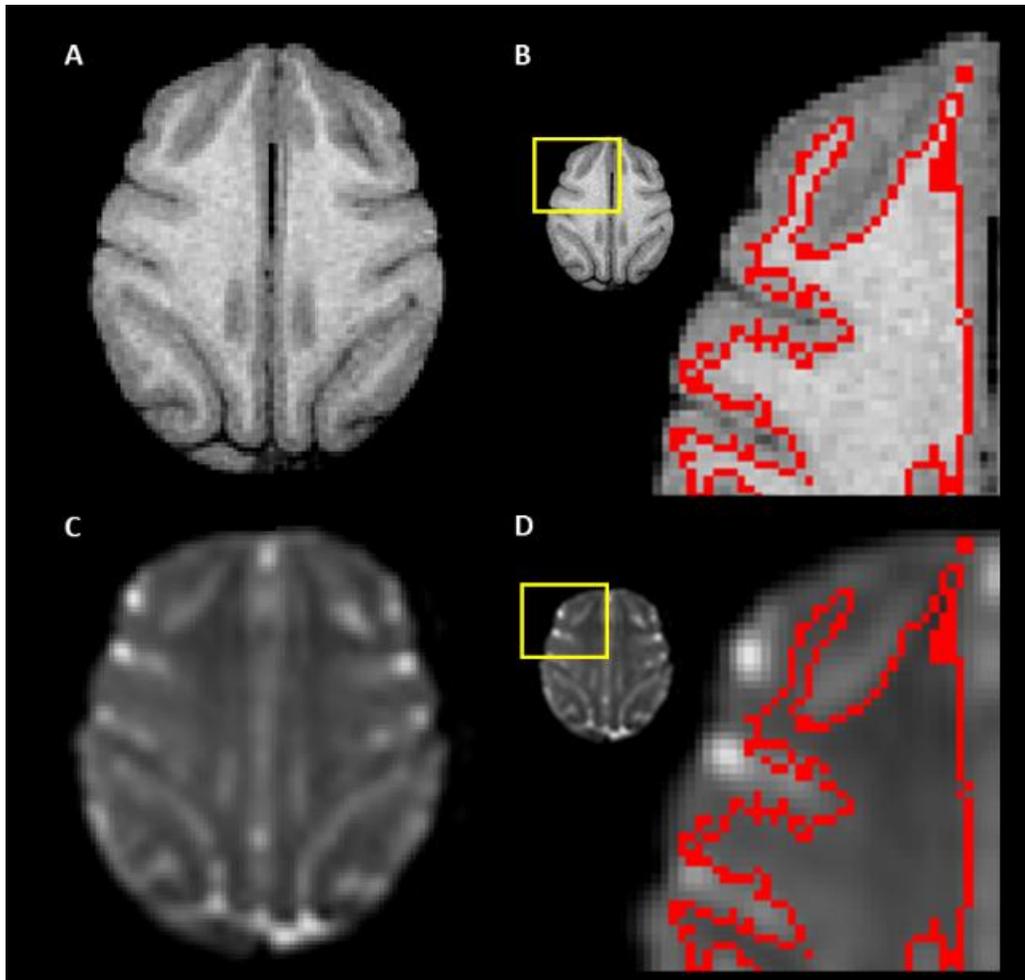


Figure 2.8: A T1-weighted image (A) and the corresponding DW image registered to it using Boundary based registration (C) are shown. Also included are the zoomed in versions of the area highlighted in the yellow box for the T1-weighted (B) and DWI (D). The white matter edge (in red) identified by FSL's FAST algorithm is overlaid on the two images

Once the diffusion-weighted images are registered to the T1-weighted images, diffusion PDFs can be reconstructed in the high-resolution space to generate DTI or HARDI parameters of interest. Alternatively, the diffusion PDF reconstruction can be done in the diffusion space and once the parameters are generated, they can be transformed to the anatomical space using the transformation matrices generated in this section.

## 2.6 Diffusion PDF Estimation

The next step of image analysis involves estimating the diffusion PDF using the diffusion-weighted images, which in turn, paves the way for tractography. As discussed in Chapter 1, the diffusion PDF estimation can be performed using either a model based or a model free technique. The robustness of the HARDI acquisition enables us to reconstruct it either way.

### 2.6.1 Model based Reconstruction

#### 2.6.1.1 *Single Tensor Fitting*

FSL's Diffusion toolbox (FDT) was used to fit the diffusion-weighted images in the T1 space to a single tensor model. The eigenvalues and eigenvectors corresponding to each voxel within the brain were computed. Fractional anisotropy (FA), axial diffusivity (AD) and radial diffusivity (RD) are calculated from the eigenvalues using equation (1-6). A T1-weighted image of a bonnet monkey and the corresponding FA (B), AD (C) and RD (D) images are shown in Figure 2.9. The FA map, depicting the degree of anisotropy, shows the white matter to be brighter compared to the gray matter or CSF. The axial diffusivity, a map of the primary eigenvalue  $\lambda_1$ , is higher for anisotropic regions and is believed to be a direct indicator of white matter maturation. It has higher values corresponding to the white matter regions. The radial diffusivity, i.e. the average of  $\lambda_2$  and  $\lambda_3$ , is believed to depend on the axonal diameter and the degree of myelination. When the white matter is highly myelinated or the diffusion is anisotropic, the radial diffusivity is reduced. In other words, gray matter and CSF have the highest values in a RD image. This single tensor fitting process is repeated for all the monkey brain images.

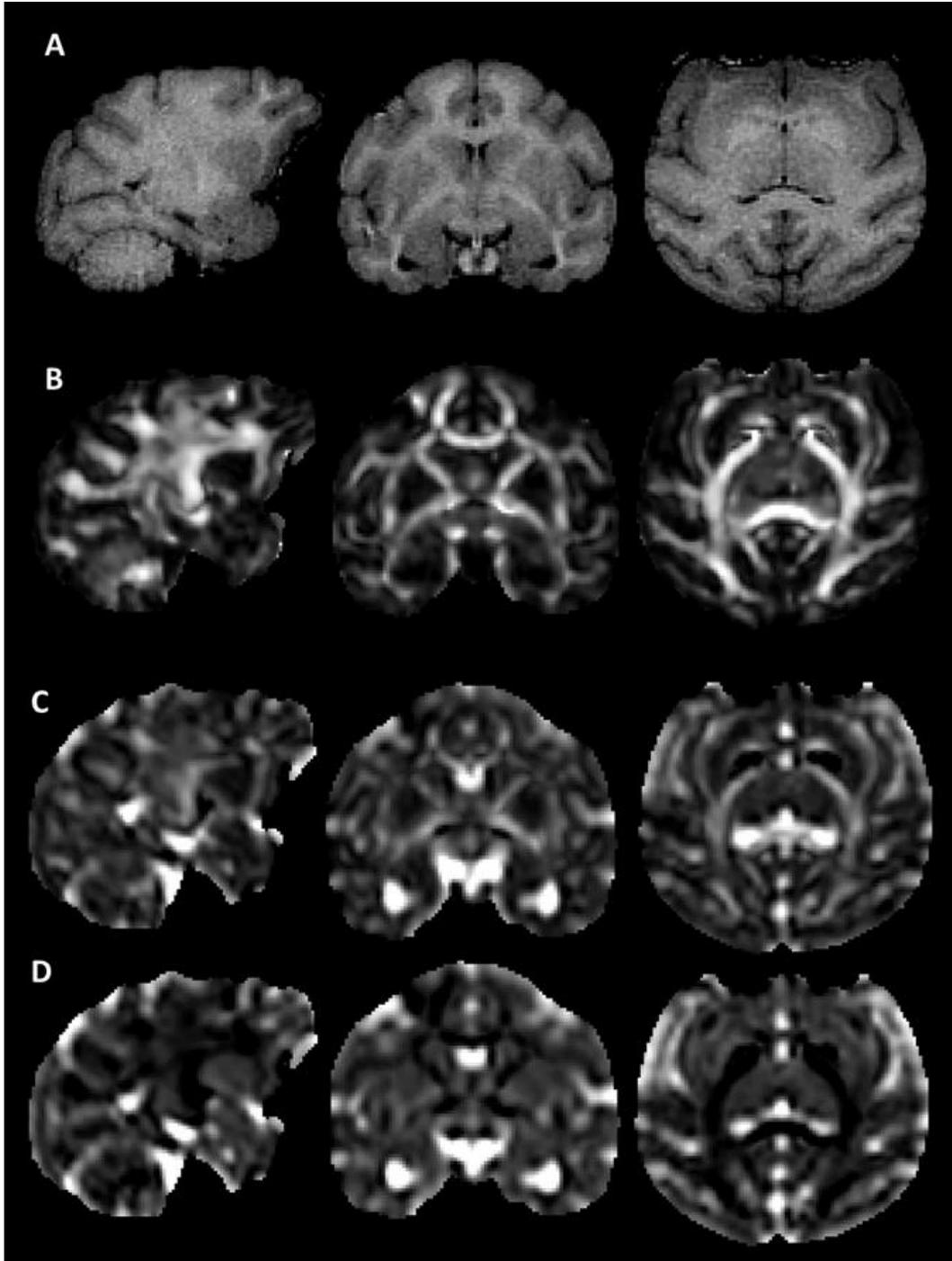


Figure 2.9: Sagittal, coronal and axial cross-sections of a monkey brain showing the T1-weighted images in (A), the corresponding fractional anisotropy (B), axial diffusivity (C) and radial diffusivity (D) images. White matter has a high FA compared to the gray matter and cerebrospinal fluid. White matter pathways are visible in the T1- images in (A). Corresponding structures in fractional anisotropy and axial diffusivity images appear brighter than the surrounding structures. In the radial diffusivity images (D), the white matter appears darker as the gray matter and cerebrospinal fluid has higher diffusivity than white matter.

### 2.6.1.2 *Multi-tensor Fitting*

The FDT toolbox also enables fitting a multi-compartment model to the diffusion-weighted images using a Bayesian Estimation of Diffusion Parameters Obtained using Sampling Techniques modelled using crossing fibers (BEDPOSTX). In this approach, a user-specified number of fiber compartments are modelled within a voxel. As described in Chapter 1, the probabilistic tractography repetitively samples from an underlying distribution to generate multiple streamlines from each voxel. For each modelled fiber within a voxel, BEDPOSTX generates Markov Chain Monte Carlo sampling and builds up distributions in the spherical co-ordinate system. The system is set up to model up to three crossing fibers in each voxel. The modelling of fibers and subsequent formation of a sampling distribution is performed in the low-resolution diffusion space. BEDPOSTX is a computationally expensive algorithm and can take up to 15 hours for a high-resolution diffusion-weighted image; the time taken by the algorithm can be reduced by processing the low-resolution diffusion-weighted images. As the images are already registered to the high-resolution space, any output from FSL's diffusion toolbox can be transformed using the transformation map derived in Section [2.5.2].

Figure 2.10 shows the three crossing fiber model for one of the bonnets overlaid on a FA map along with the zoomed in version of the region in the yellow box. The red color sticks represent the first modelled fiber. The colors blue and pink represent the second and third fiber modelled within each voxel.

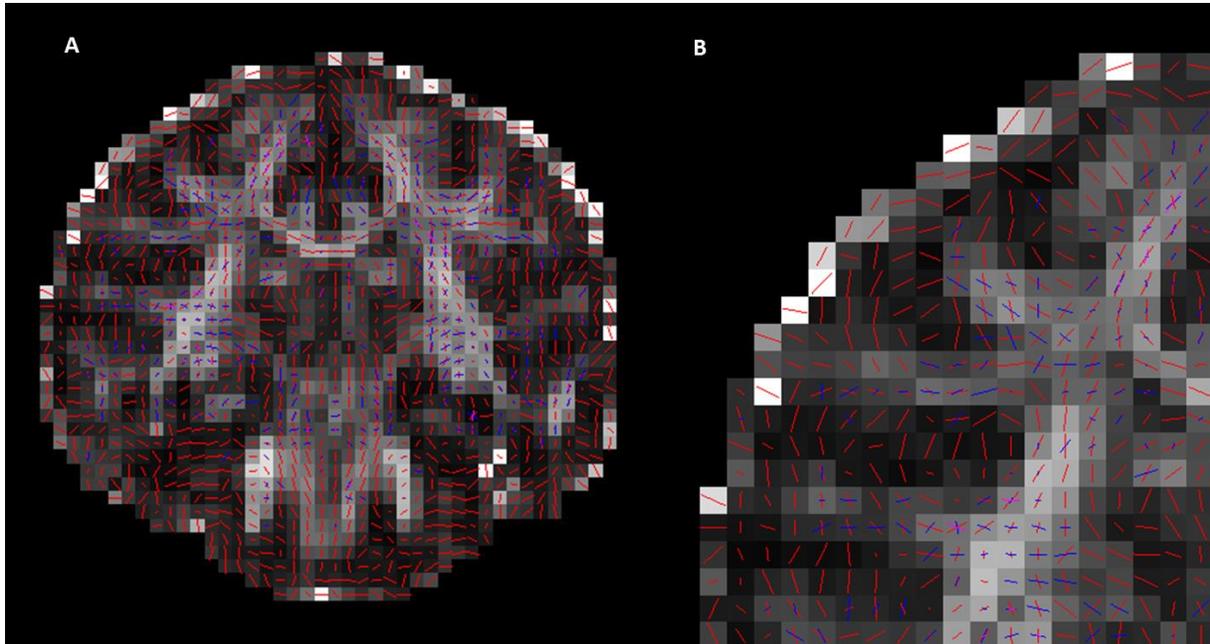
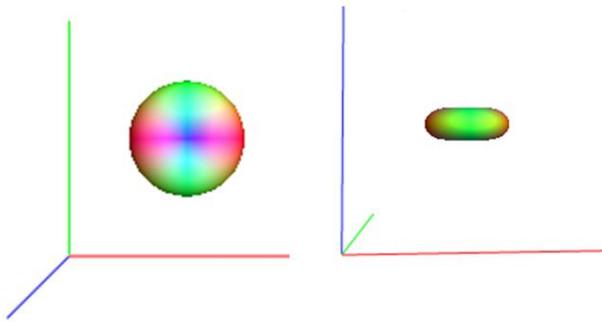


Figure 2.10: Fractional Anisotropy map of a coronal slice in diffusion space (A) with up to three crossing fibers modelled in each voxel using BedpostX. This modelling is performed in the native diffusion space. Image in (B) shows a zoom in of a small section of (A) showing the first (red), second (blue) and the third (pink) fiber modelled within each voxel.

## 2.6.2 Model free CSD Reconstruction

The MRtrix toolbox (Tournier, Calamante et al. 2012, MRtrix) implements the CSD reconstruction algorithm. The response function required for CSD is obtained from the raw diffusion images by identifying image voxels that are believed to contain a single fiber population. The response function in white matter tissues is the diffusion signal from voxels with a single fiber population. The response function is estimated using the algorithm outlined in Chapter 1.

Figure 2.12 highlights a set of single fiber voxels from an axial cross-section of a monkey brain that were used in the estimation of the response function. Note that the voxels belong to the highly anisotropic region of corpus callosum. Figure 2.11 shows the final response function generated for one of the bonnet monkeys. As stated earlier, the DWI signals are rotated such that the response functions are aligned along the z-direction i.e. the fibers are oriented along the z-direction.



*Figure 2.11: The diffusion profile generated for the CSD operation in one of the monkeys. The function is ideally supposed to be a flat disk but the shape varies slightly due to the truncation of higher-order Spherical Harmonic coefficients.*

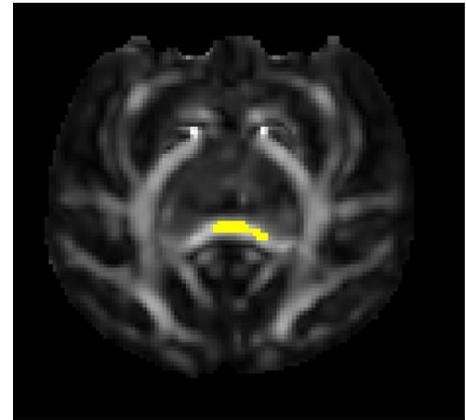


*Figure 2.12: The voxels that were selected for the generation of the response function are highlighted in yellow. The image only shows the voxels from the axial slice being displayed.*

When a diffusion gradient is applied along the z-direction, the signal along the z-direction is completely lost and the diffusion profile or the response function has a disc shape in the x-y plane. The figure shows the top view and the side view of the response function. Instead of the ideal flat disk, the response function is slightly oblate along the z-direction, represented by the blue axis, due to the truncation of higher-order spherical harmonic coefficients in the CSD.

Using the response function, non-negativity constrained spherical deconvolution yields FODs for each voxel. The FOD lobes are color-coded based on the direction of the fiber they represent: red for left to right, blue for superior-inferior and green for posterior-anterior. Figure 2.13 shows an FA map corresponding to a coronal cross-section. The FODs generated from the CSD reconstruction are overlaid on the FA map in (A). The FODs from the yellow box are displayed in (B). In regions, with two crossing fibers, the FODs have two distinct peaks along the two orientations of the fibers. The transition from one orientation to another is visible as the color of the FODs changes.

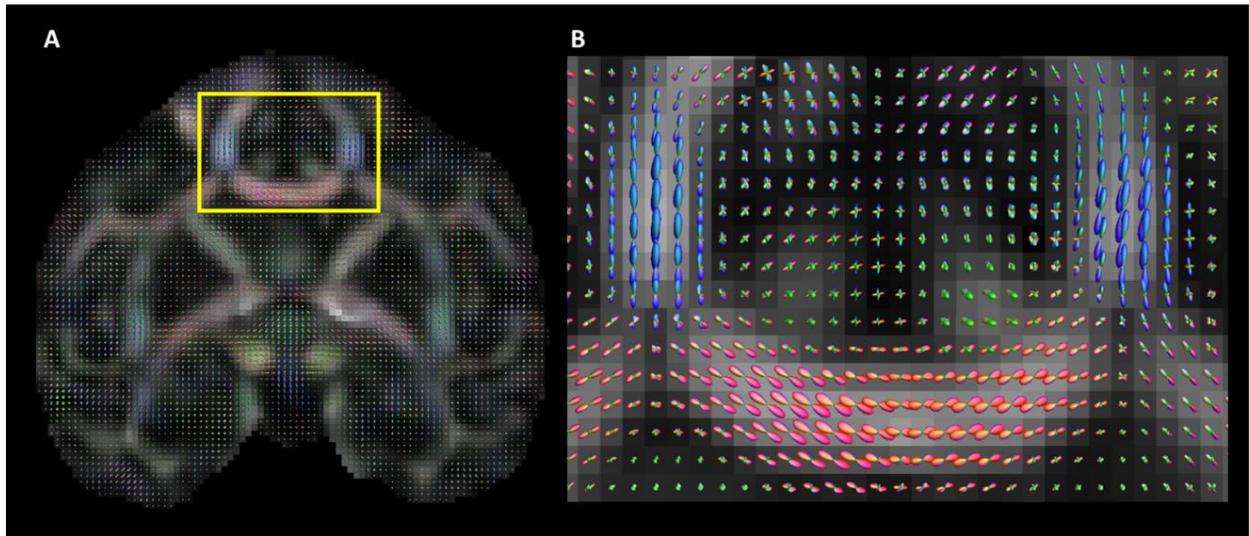


Figure 2.13: FODs overlaid on an FA map (A). (B) is the zoom in to the yellow box. The ODFs are color-coded and are scaled by the underlying FA values. This means that voxels with higher FA will have larger FOD lobes.

## 2.7 Region of Interest Identification

Fiber tractography can be used to assess the connectivity between any two regions of interest (Hagmann, Kurlant et al. 2007). A pre-requisite to tractography is identification of the regions of interest (ROI) from which a tract is either initiated (seed mask) or terminated (target mask). This delineation is done by creating binary masks with a value of one within an ROI and zero everywhere else. The ability of the tractography algorithm to select the relevant streamlines is improved by specifying anatomically correct waypoints through which the fiber tracts of interest are known to pass, or by specifying exclusion ROIs to discard any streamlines that stray into it.

### 2.7.1 Seed and Target Masks

The seed ROI decides which voxels in an image would be used to initiate streamlines. Once the streamlines reach a target ROI, they are terminated. Sara Burke et al. (Burke, Thome et al. 2014) describe how the gray matter regions corresponding to the OFC and amygdala are identified on the T1-weighted images of each bonnet macaque's brain. The amygdala mask consists of the basolateral and the basomedial nuclei of amygdala.

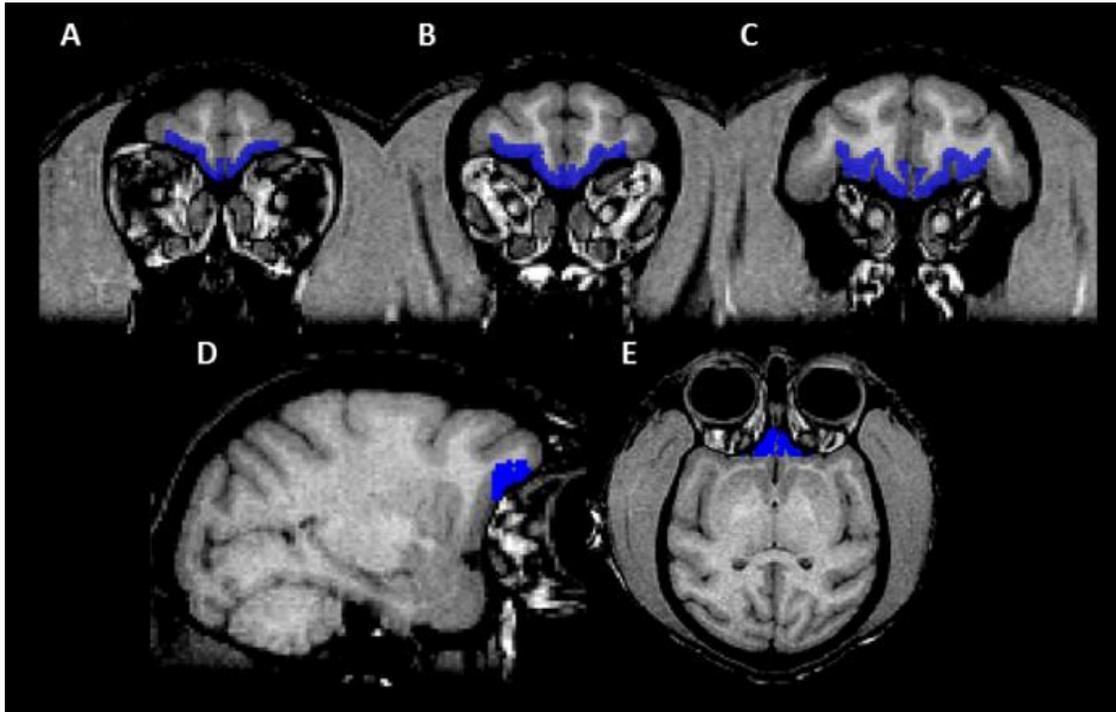


*Figure 2.14: OFC binary mask (blue) overlaid on coronal (A-C from anterior to posterior of the brain), sagittal (D) and axial (E) cross-sections of a T1-weighted image.*

Figure 2.14 shows the orbitofrontal cortex mask in blue overlaid on coronal (A-C), sagittal (D) and axial (E) slices of the T1-weighted image of a monkey brain. The coronal slices are arranged in anterior to posterior direction. Figure 2.15 shows the amygdala mask in red overlaid on coronal (A-C), sagittal (D) and axial (E) slices of the T1-weighted image of a monkey brain. The coronal slices are once again arranged in anterior to posterior direction as we move from A to C.

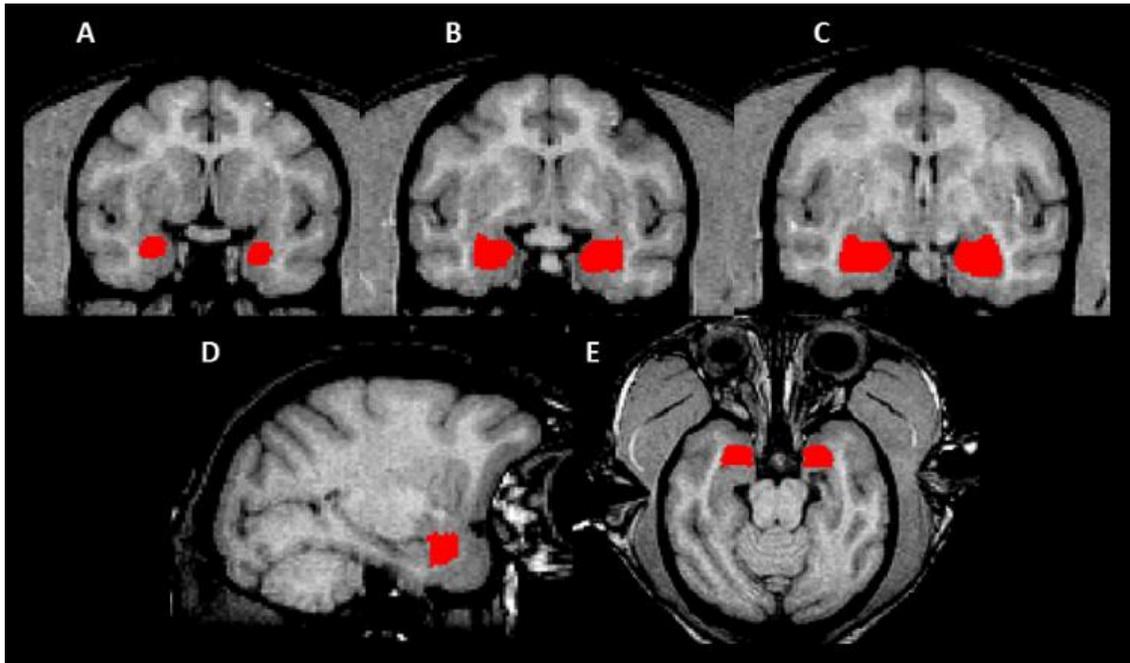
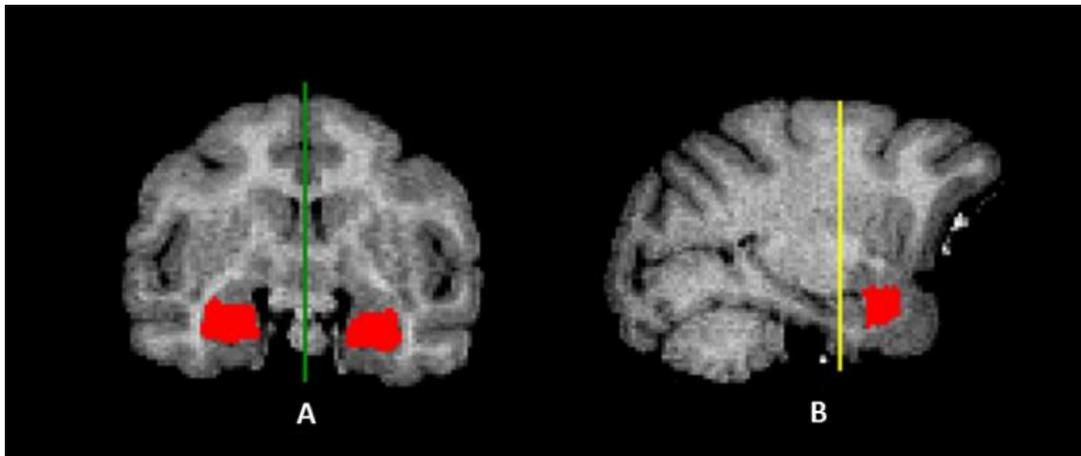


Figure 2.15: Amygdala binary mask (red) overlaid on coronal (A-C from anterior of the brain to posterior), sagittal (D) and axial (E) cross-sections of a T1-weighted image.

In a tracer study on rhesus macaque monkeys (Ghashghaei, Barbas 2002), the axonal connections from OFC to amygdala are shown to terminate within the amygdala, in a white matter sheath that lies in the basolateral (BL) and basomedial (BM) nuclei of amygdala. Other studies (Schmahmann, Pandya et al. 2007) have shown that uncinate fasciculus (UF) emerges from the anterior part of the temporal lobe and passes through the lateral nucleus of amygdala towards the frontal cortex. In order to avoid ambiguity, the entire amygdala mask identified above was used as a seed region and the OFC volume was used as the target region.

### 2.7.2 Exclusion Mask

A number of streamlines can exist between two regions of interest. For example, many tracks travel along the UF as it propagates from the amygdala to the OFC; some of these include the commissure fibers that connect the left and the right hemispheres, inferior longitudinal fasciculus that extends posterior to the amygdala. With the knowledge of anatomy, it is possible to create exclusion masks to filter out the tracts that are not of interest.



*Figure 2.16 A: Left-right separation mask in green on a sagittal slice and exclusion mask in yellow on a coronal slice. Exclusion mask in A excludes the commissure fibers, that crossover from the left to the right hemispheres. Exclusion mask in B excludes fibers from inferior longitudinal fasciculus from being taken into account.*

In Figure 2.16, two exclusion masks are shown. The exclusion mask in green (A) is identified in the sagittal plane to eliminate tracks that cross over from one hemisphere to the other. Another exclusion mask (B) in yellow is identified on the coronal plane to eliminate tracts from the amygdala that extend posterior to it. Together, these would exclude commissure fibers and fibers from inferior longitudinal fasciculus from being taken into account.

### 2.7.3 Inclusion Mask

To increase the accuracy of the streamlines, a waypoint ROI is identified along the UF to ensure any tracts that pass through the ROI are included. This is drawn in the region where the UF fiber bundles transition from the temporal to the frontal lobe as described in (Petrides, Pandya 2007). Figure 2.17 shows the most posterior coronal cross section of a T1-weighted image where a clear separation between the frontal and the temporal lobes can be observed. The uncinate fasciculus ROI is overlaid on the T1-image (B) and the corresponding FA map (C).

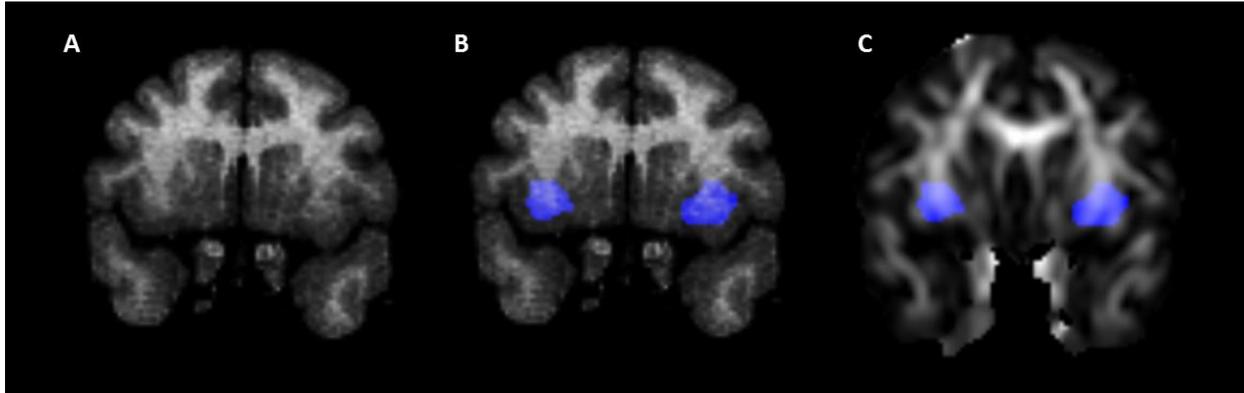


*Figure 2.17: Coronal cross-sections of a monkey brain showing the T1-weighted image (A), uncinatus fasciculus inclusion mask in blue overlaid on the T1-weighted image (B) and the corresponding fractional anisotropy image. The coronal slice in A shows a clear separation between the frontal and the temporal lobes and marks the region of transition of the uncinatus fasciculus.*

## 2.8 Fiber Tractography

Two probabilistic algorithms are used to ensure consistency in the location of the UF fiber tracts. In both techniques, the seed and target masks and the inclusion and exclusion ROIs identified in section 2.7 are used.

### 2.8.1 Multi-tensor Diffusion PDF based Probabilistic Tractography

FSL's Diffusion toolbox (Behrens et al., 2003, Behrens et al., 2007) is used to initiate 5000 streamlines from the seed voxels within each monkey's amygdala. The algorithm randomly selects 5000 samples from the sampling distribution generated by BedpostX that accounts for the uncertainty in the propagation of fibers, similar to the technique described in Chapter 1. The streamlines are propagated towards the OFC with a step size of 0.5 mm and a curvature threshold of 0.2. The fiber tracking results in a connectivity distribution where each voxel has an intensity value that represented the number of streamlines that pass through the voxel and are successful in reaching the target mask. The algorithm also outputs the 'waytotal', which is the total number of tracks from the seed ROI that are successful in reaching the OFC via the waypoint or the inclusion ROI.

## 2.8.2 FOD based Probabilistic Tractography

Probabilistic tractography is also performed in MRtrix using a 2<sup>nd</sup> order integration over the fiber orientation distributions (iFOD2) algorithm described in Chapter 1. From every seed voxel in amygdala, 2000 streamlines are initiated. Additional constraints such as a minimum FA value for a seed voxel and terminating voxel are also imposed. The output of this tractography is a set of streamlines in a tract file, connecting the two ROI that can be visualized by overlaying on the corresponding FA or T1-weighted image.

## 2.8.3 Tractography Parameters

A number of parameters control the end-result of tractography and it is therefore important to choose the correct values for the parameters in the two algorithms. The following tabular column shows the constraints that were used.

Terminology	Description	FSL tractography	MRtrix tractography
<b>Source</b>	The source data to be used for tractography	Multi tensor fitting from BEDPOSTX	The spherical harmonic image generated from CSD technique
<b>Algorithm</b>	What kind of tractography algorithm is used	Probabilistic	iFOD2
<b>Step size</b>	Increments along trajectory	0.5 mm	0.5*voxel size = 0.3 mm
<b>Curvature</b>	The maximum permitted angle between successive step size	0.2	45 degrees
<b>Cutoff</b>	When to terminate tracks	No constraints	FOD amplitude < 0.1
<b>Initial cutoff</b>	When to start a streamline	No constraints	FOD > 0.1
<b>Streamlines</b>	The number of streamlines to generate	5000 samples per seed voxel	2000 samples per seed voxel in iFOD2 or Two million streamlines per seed ROI in ACT

## Chapter 3 Assessing Uncinate Fasciculus Tract Integrity in Bonnet Macaque Monkeys

Chapter 2 introduced an image processing pipeline that was applied to a group of 11 female bonnet macaques: six young to mature (mean age: 13.33 years, standard deviation: 1.62 years) and five aged monkeys (mean age: 26.03 years, standard deviation: 2.76 years). The diffusion-weighted images for each monkey were corrected for distortions due to eddy currents, field inhomogeneity, and filtered for noise removal using the local PCA based denoising, as described in the previous chapter. The DW images were registered to the bias corrected T1-weighted images before performing a multi-tensor fitting and constrained spherical deconvolution (Tournier, Calamante et al. 2007). The fractional anisotropy (FA) and the fiber orientation distribution (FOD) images generated from the two algorithms were used in probabilistic tractography to delineate the axonal bundles belonging to uncinata fasciculus (UF), a prominent white matter pathway that connects the amygdala with the orbitofrontal cortex. This chapter presents the results of probabilistic tractography from the multi-tensor (Behrens, Berg et al. 2007) and the FOD-based algorithm (Tournier, Calamante et al. 2012). Quantitative measures related to white matter integrity are calculated along the length of the UF tracts and statistical analysis of these parameters are performed.

### 3.1 Probabilistic Fiber Tractography

#### 3.1.1 Connectivity Map from Multi-Tensor Fit based Tractography

The probabilistic algorithm using BEDPOSTX (Behrens, Berg et al. 2007, Behrens, Woolrich et al. 2003) in FSL generates a connectivity map from each voxel in the seed amygdala binary mask to every other voxel in the brain that lies along the uncinata fasciculus. Figure 3-1 shows a connectivity map for one of the bonnet monkeys overlaid on an axial cross-section of the corresponding FA map. From the total number of tracts, also known as the way total, which successfully reach the target orbitofrontal-cortex region, the number of streamlines that pass through any voxel is given by the connectivity map. The tracts are displayed in a red-yellow color scale where yellow represents the maximum value of a given connectivity map.

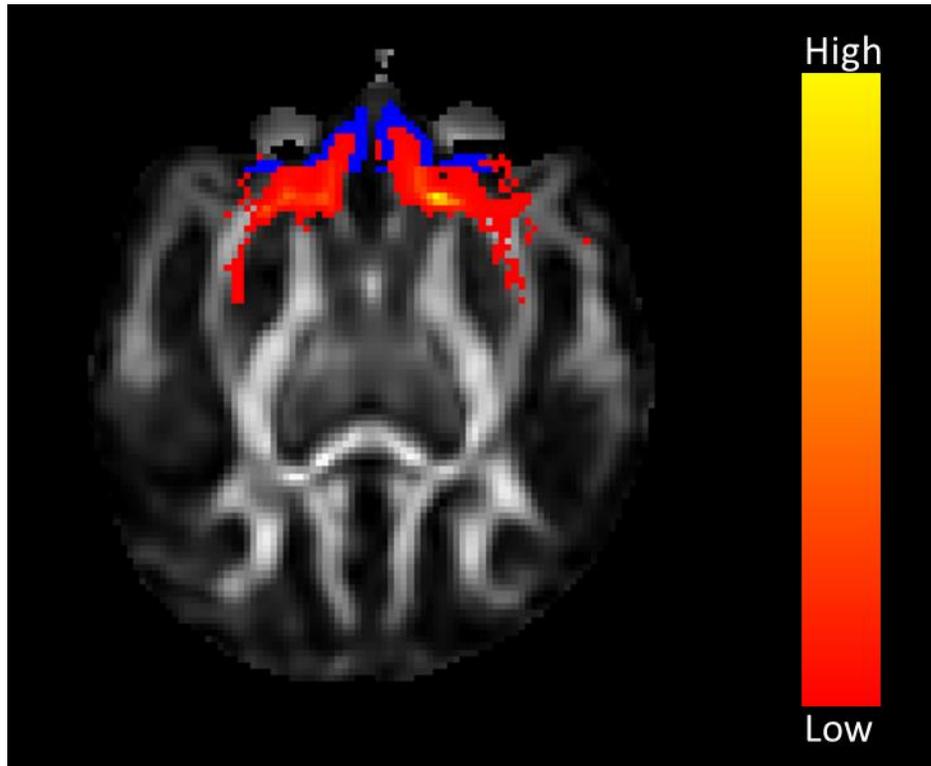


*Figure 3-1: The connectivity map between amygdala and the orbitofrontal cortex (shown in blue) is overlaid on an axial cross-section of a fractional anisotropy image for one of the bonnet monkeys. The slice shows uncinatus fasciculus tracts entering into the orbitofrontal cortex. Each voxel in the connectivity map represents the number of tracts that pass through that voxel and end up in orbitofrontal cortex. The tracts are shown in a red-yellow color map where yellow represents the maximum value of the connectivity map.*

As the way total for different bonnet monkeys may differ, the connectivity map for each animal might have different maximum values. Figure 3-2 shows the connectivity map of uncinatus fasciculus overlaid on a series of fractional anisotropy maps of a monkey brain. The axial slices are arranged moving from inferior of the brain to the superior regions of the brain. The amygdala region is shown in blue in the slices from the inferior regions of the brain whereas the orbitofrontal cortex region, also in blue, is visible in the later slices. To eliminate voxels that have a low connectivity value, a threshold has been applied at 10% of the maximum value of the connectivity map.

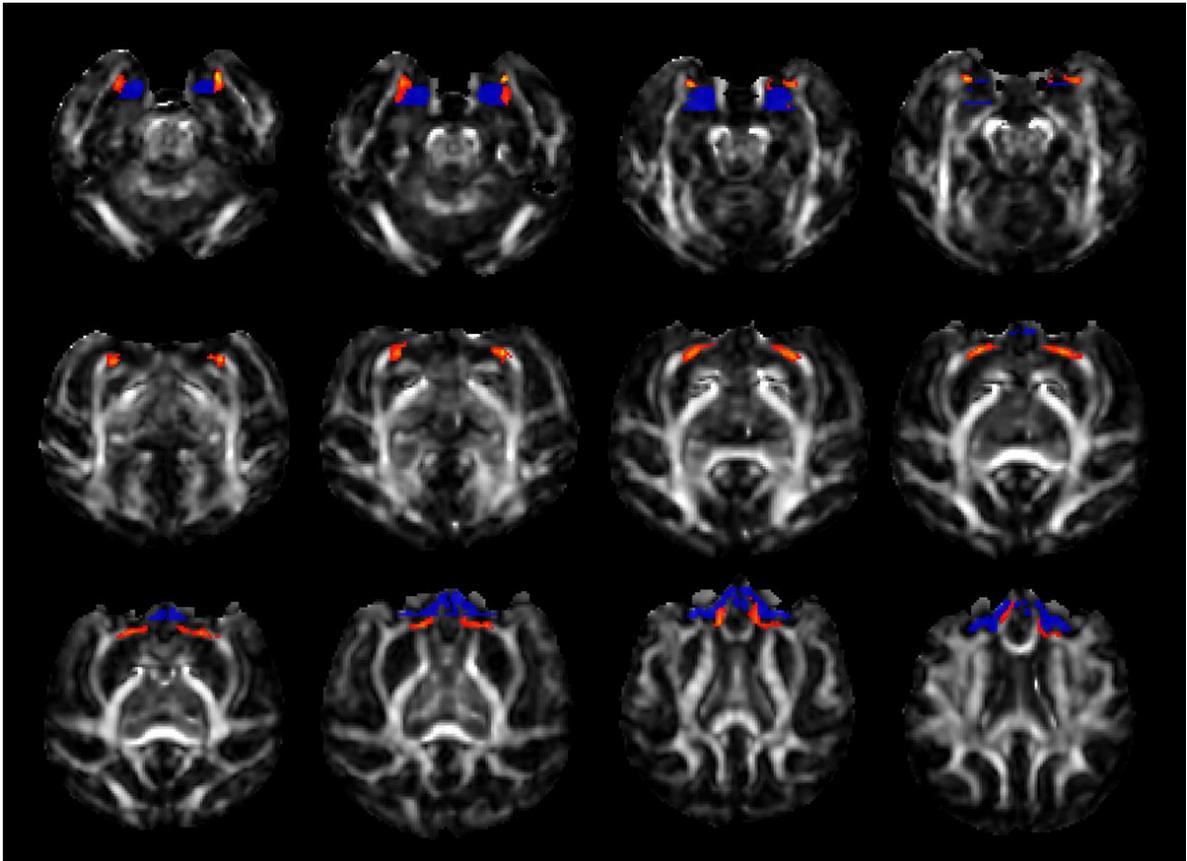
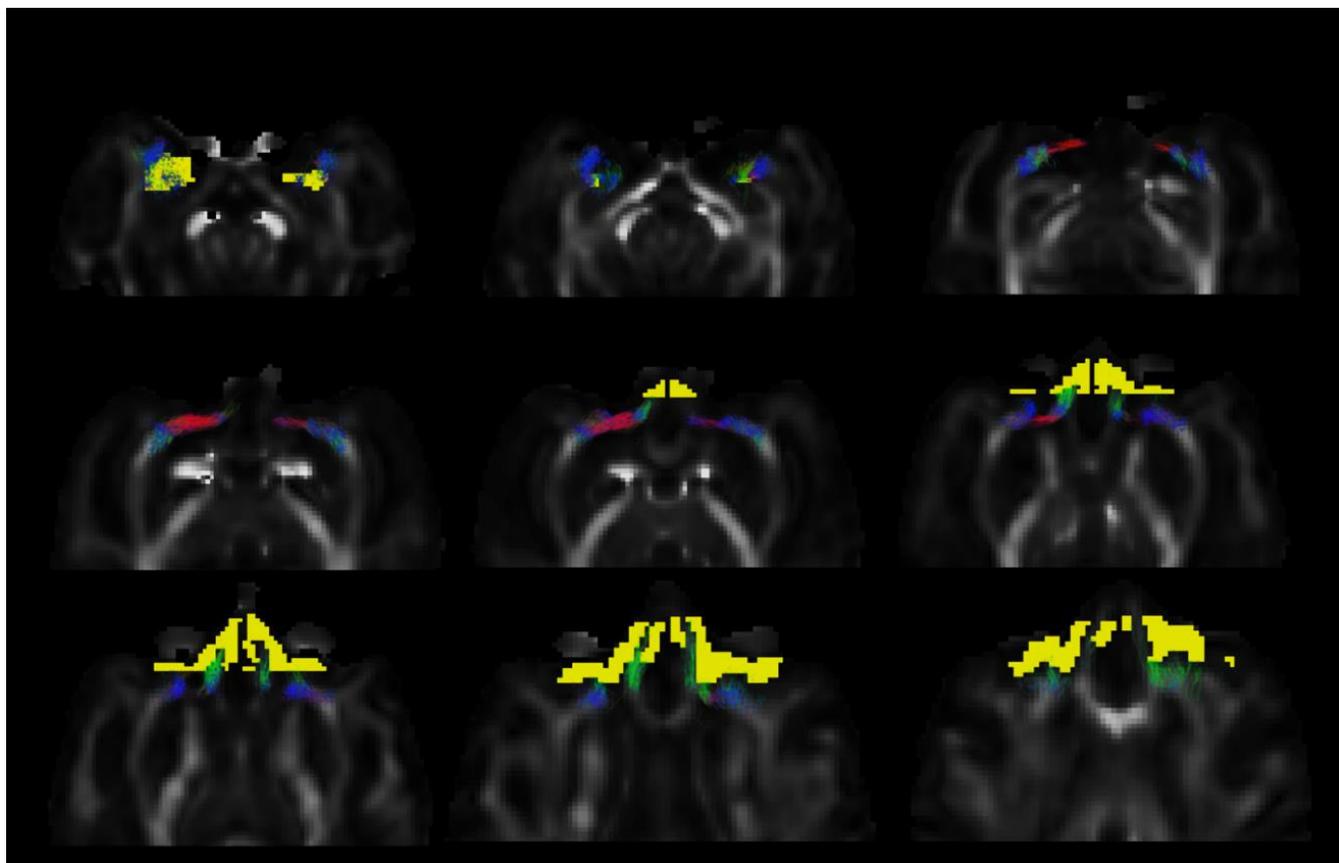


Figure 3-2: The uncinatus fasciculus connectivity map in one of the bonnet monkeys is overlaid on axial cross-sections (moving from inferior to superior) of the fractional anisotropy map. The amygdala is highlighted in blue in the top row of the image and the orbitofrontal cortex is highlighted in blue in the bottom row of the image. Voxels that have less than 10% of the maximum number of tracts in the connectivity map were eliminated.

### 3.1.2 Streamlines from Fiber Orientation Distribution based Tractography

Instead of a voxel based connectivity map, the FOD based tractography algorithm produces streamline structures connecting the two regions of interests. The tract streamlines generated by the CSD-iFOD2 algorithm (Tournier, Calamante et al. 2010) aid in visualizing the strength of the uncinatus fiber bundle. The wider the streamline bundle, the more number of tracts. The output tract data consists of triplets of floating-point values for every vertex along the track (Tournier, Calamante et al. 2012). Figure 3-3 shows the streamlines initiated from amygdala that successfully reach the OFC region via the uncinatus fasciculus waypoint mask. The seed and the target masks are highlighted in yellow.



*Figure 3-3: Fiber tracts from amygdala to orbitofrontal cortex are overlaid on axial slices moving from inferior to superior. The streamlines are direction-encoded i.e. the fibers going left to right are in red, superior to inferior are in blue and posterior to anterior are in green. From every voxel in the seed amygdala mask (in yellow in the posterior slices), 2000 streamlines are initiated. All streamlines that reach the mask (in yellow in the superior slices) through the waypoint uncinate fasciculus and do not enter any of the exclusion masks identified in Chapter 2 are shown here.*

The tracts themselves are direction-encoded that is, the fibers are colored depending on the direction along which they are moving. Fibers in red, blue and green represent fibers moving along the left to right, superior to inferior and the posterior to anterior directions, respectively. Fibers along intermediate directions are represented by a combination of these three colors. The uncinate streamlines can be seen originating from the amygdala mask, highlighted in yellow in the top row. These streamlines are blue in color as they move up, turning green as they move from posterior to anterior before turning red as they move towards the medial regions of the brain. The final part of the uncinate fasciculus curves towards the frontal cortex from behind, in a hook shaped manner, as is evident from the green colored fiber tracts in the bottom row.

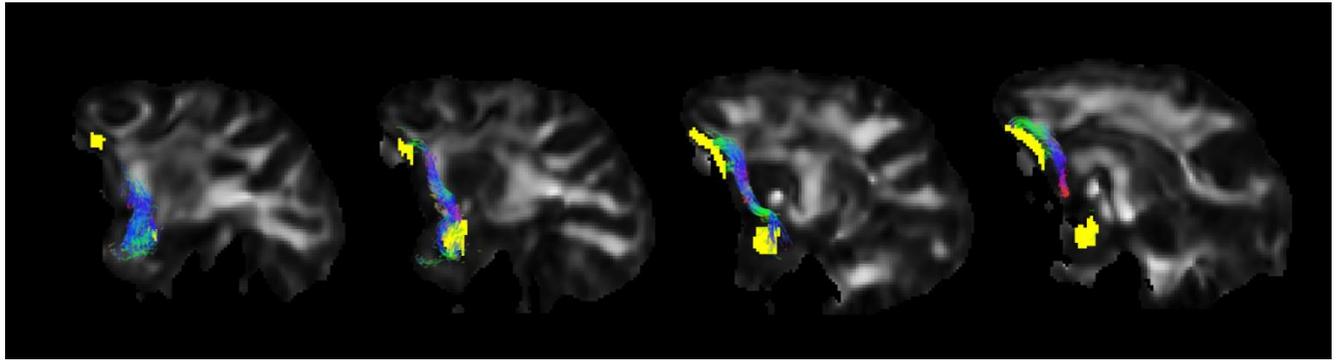


*Figure 3-4: Fiber tracts from amygdala to frontal cortex are overlaid on sagittal slices moving from right edge to the medial regions of the brain. The streamlines are direction-encoded i.e. the fibers going left to right are in red, superior to inferior are in blue and posterior to anterior are in green. As the fibers emerge from the amygdala in the first image, they rise up and are blue in color. The hook shape of the uncinate fasciculus tracts can be seen in the third and the last image.*

The UF tracts along the sagittal slices for the same subject are shown in Figure 3-4. The hook shape of the uncinate is clear in the sagittal cross-sections displaying the tracts. The amygdala and OFC masks are visible in yellow.

### 3.1.3 Connectivity Map vs FOD Streamlines

Tractography algorithms that use diffusion PDF reconstructed from completely different methods were used to ensure consistency in the identified uncinate tracts, given the same set of source, target and waypoint masks. Figure 3-5 compares the connectivity map from the multi-tensor model with the fiber streamlines from CSD's iFOD2 based tractography algorithm for one of the monkeys that showed a bias in the UF tracts between the left and the right hemisphere. The images in column A show the connectivity map overlaid on axial slices of the corresponding T1-weighted image whereas those in B show the fiber streamlines for the same axial slices. The connectivity map is displayed in the red-yellow color scale. The maximum tract intensity is limited to 300, implying that the color yellow corresponds to voxels with at least 300 streamlines passing through them. The fiber streamlines on the right are direction-encoded and the width of the fiber bundle is proportional to the total number of streamlines.

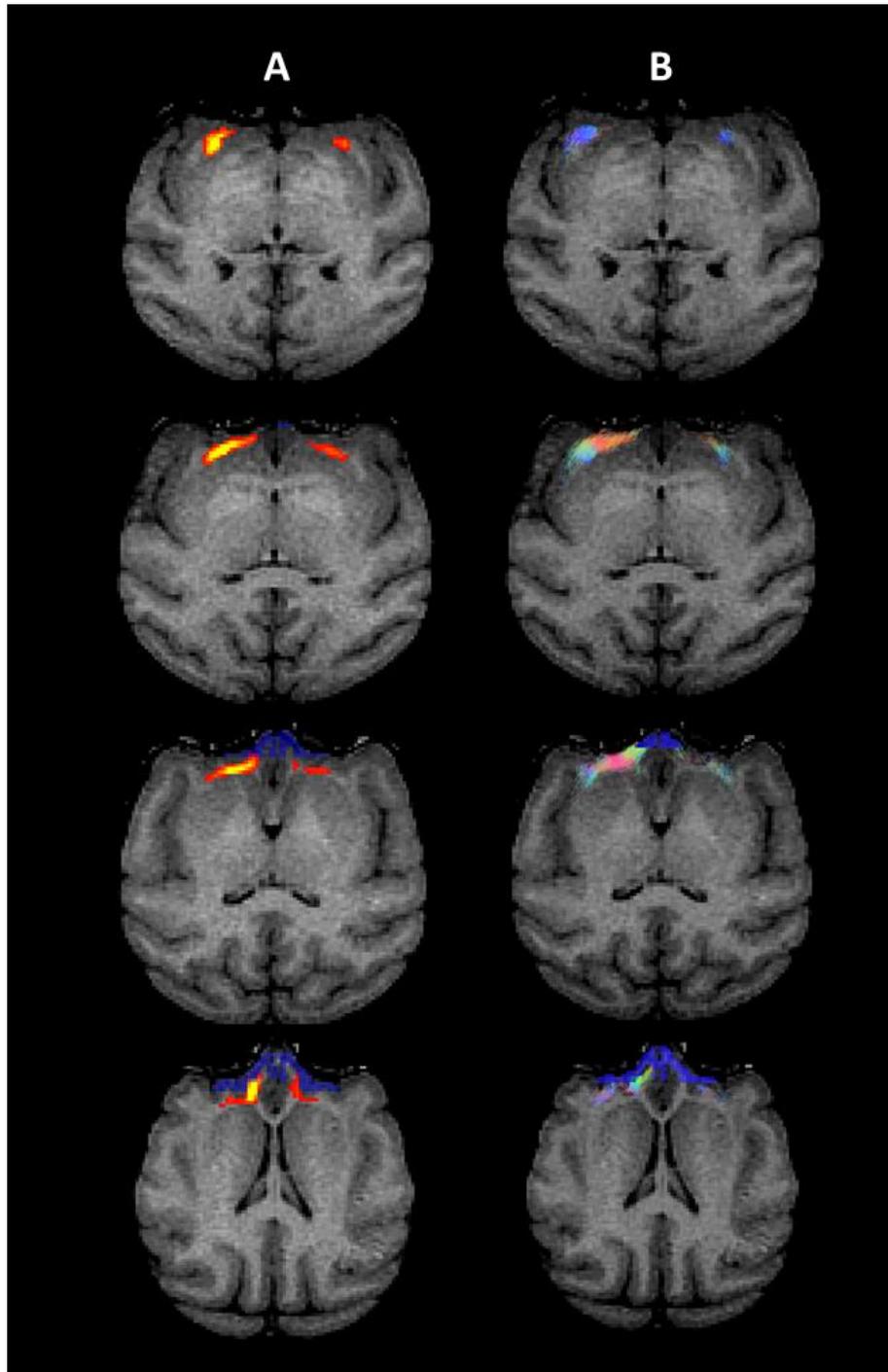


*Figure 3-5: Axial slices of a T1-weighted bonnet brain show the overlaid uncinate tracts identified by a multi-tensor based (A) and a FOD based (B) probabilistic algorithm. Rows 3 and 4 also show the orbitofrontal cortex ROI in blue. Both the algorithms predict that the right uncinate fasciculus is stronger than the left for this particular monkey.*

The connectivity map shows higher intensities in the right hemisphere, as indicated by more number of yellow voxels in the connectivity map. This correlates well with the thick axonal bundle predicted by the CSD-iFOD2 algorithm. The consistency between the two results improves our confidence in the results from the two algorithms.

## 3.2 Quantifying Uncinate Fasciculus Tract Integrity

It is believed that with aging, there is a reduction in the white matter density due to axonal pruning or demyelination (Salat, Tuch et al. 2005). Figure 3-6 shows the uncinate streamlines from a young and an aged monkey, overlaid on a series of axial slices of their corresponding T1-weighted image. The amygdala and the orbitofrontal cortex masks are highlighted in yellow for reference. From visual inspection, it is evident that in this particular case, the younger monkey appears to have a thicker axonal bundle compared to the older one. However, for comparisons between groups of monkeys, more than visual inspection is needed and this is the motivation for analysis strategies to quantify tract strength.

### 3.2.1 Tract-based Analysis

There are two prominent analysis strategies – voxel based and tract based analysis. A voxel based analysis (VBA) locally compares imaging parameters such as those extracted from a simple tensor fit (FA, AD or RD) for the whole brain across multiple subjects or groups. Such an analysis is feasible only when the individual images are registered to a common co-ordinate system such as the Montreal Neurological Institute (MNI) template, Talaraich space (Talairach, Tournoux 1988) or DARTEL (Ashburner 2007). The non-linear transformation to a common space ensures that an anatomical region of interest retains its spatial position with respect to all subjects. Due to its high-level of dependency on effective registration between subjects, any mis-alignment or mis-registration can produce erroneous results as the anatomical ROIs no longer overlap with each other.

A tract-based analysis on the other hand involves identifying the tracts of interests and extracting a mean from all the voxels that lie along the tract. This strategy returns a single value per subject, which can then be used for comparisons between subjects or groups.

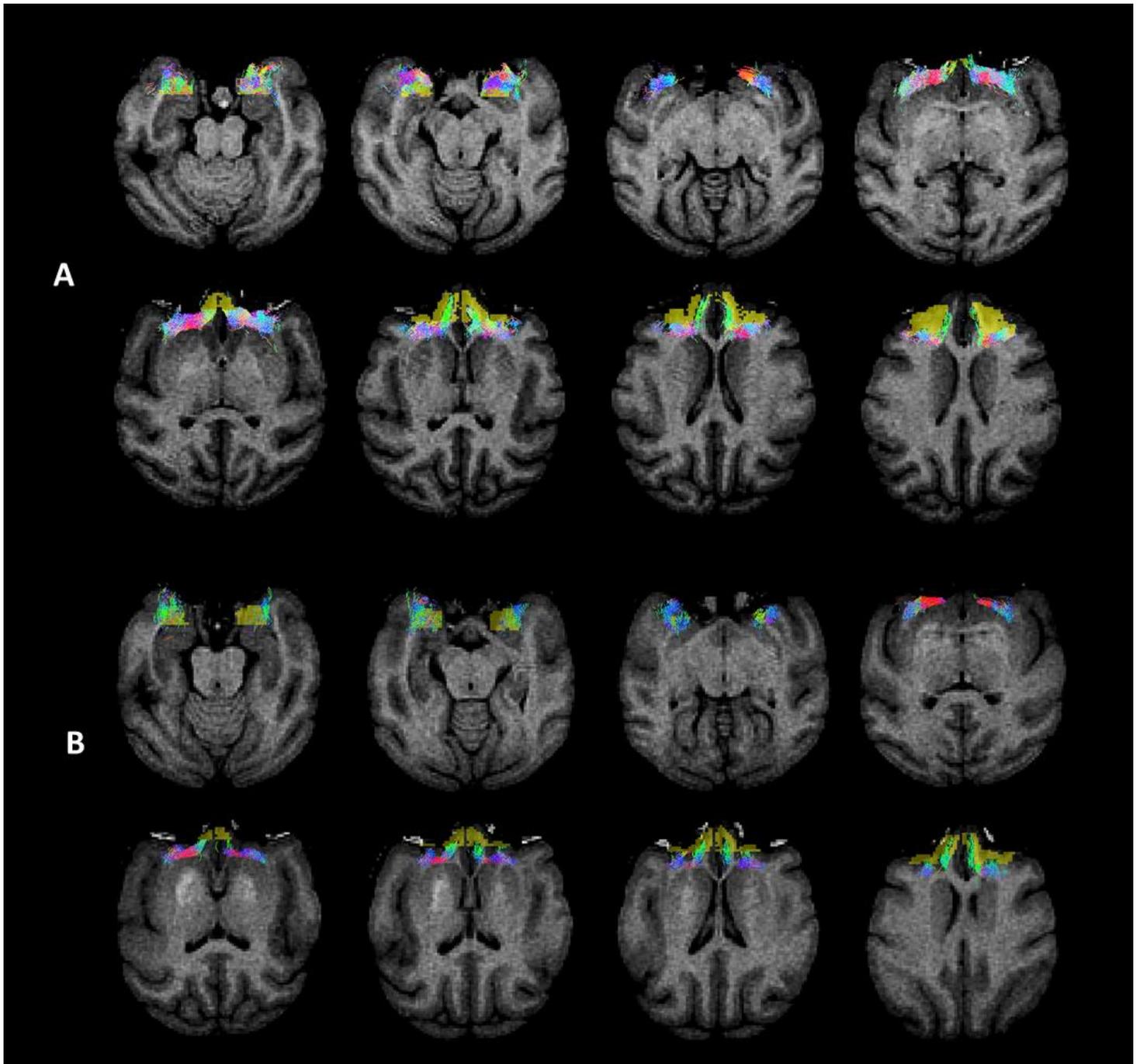


Figure 3-6: Probabilistic streamlines from uncinate fasciculus overlaid on axial cross-sections of a T1-weighted image belonging to a young monkey (A) and an aged monkey (B). The axial slices move from the inferior to the superior direction. The amygdala mask and the orbitofrontal cortex are highlighted in yellow in the first and the second row of A and B. The uncinate tracks are larger in number and thicker in the younger monkey than the older one.

Moving the images to a common space can diminish the variability in the organization of the brain structures between the young and the aged groups of monkeys. The differences in the structures could be a key to explain age-related differences in their anatomy. As such, a tract-based analysis was performed as it permits analysis in a subject's native space. This is possible by identifying a mask for the UF pathway that can be used to extract relevant voxels from the parameter images.

### 3.3 UF Connectivity mask for DTI Parameters

A simple approach to extract DTI parameters of interest from individual subject images is to use the corresponding connectivity map, which can then be converted to a binary mask with a value of one for any voxel that belongs to the map. A criticism of using a binary mask is that it assigns equal weights to all the voxels in the mask irrespective of their probability of connectivity. To explain it better, let us consider a connectivity map that has 5000 streamlines between two regions of interests. One voxel along the identified fiber pathway has 1000 streamlines passing through it and another has only 100 streamlines passing through it. The probability that the first voxel belongs in the tract is 0.25 whereas it is 0.025 for the second voxel. A binary connectivity mask will treat these two voxels equally. An alternative is to create a probability mask where the weight associated with a voxel is equal to the probability that it belongs to the tract of interest. This is done by dividing each voxel in the connectivity map by the total number of streamlines that were not rejected due to exclusion masks. A histogram of the non-zero probabilities for each subject is generated to identify the 95<sup>th</sup> percentile of the distribution. A threshold is set at 40% of this value, such that any voxel with a probability less than 40% of the 95<sup>th</sup> percentile is set to zero. We refer to this new probability map as the weighted UF mask. As explained in (Galantucci, Tartaglia et al. 2011), a threshold at 40% of the 95<sup>th</sup> percentile instead of the maximum probability “excludes any background noise or avoids applying a restrictive threshold if the maximum intensity itself is an outlier of the distribution while correcting for differences in the dimensions of the seed regions”.

Figure 3-7 shows a connectivity map for a bonnet monkey brain. The image on the right is the corresponding probability map on which a threshold has been applied as described above.

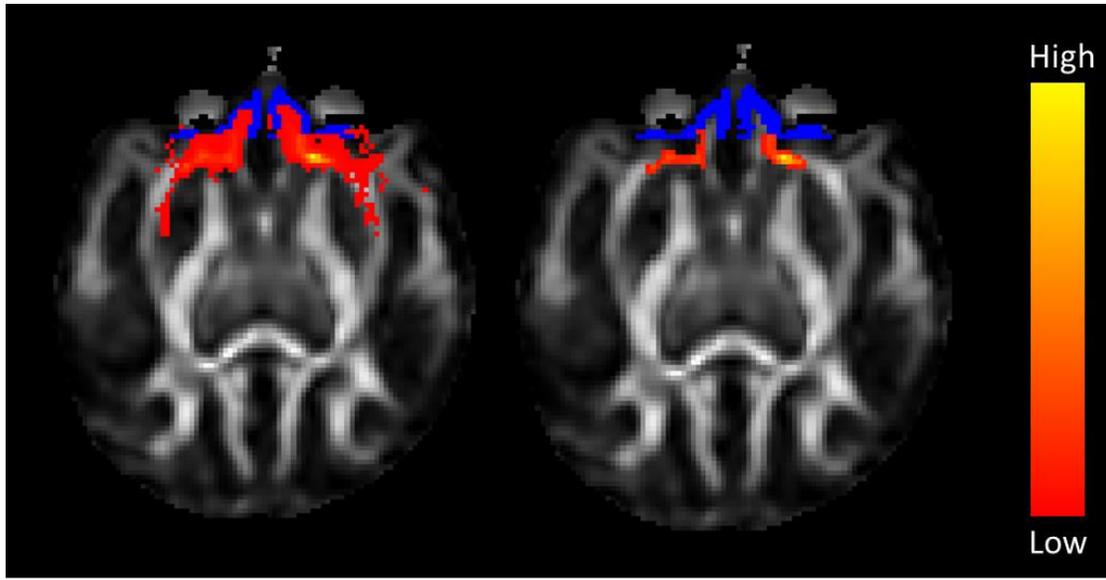


*Figure 3-7: A weighted connectivity map (right) is generated from a connectivity map (left). A probability map is created by first dividing each voxel in the connectivity map with the waytotal. A threshold is applied to the probability map such that any voxel that has a probability less than 40% of the 95<sup>th</sup> percentile of the histogram of the intensities in the probability map is set to zero.*

Parameter images such as fractional anisotropy (FA), axial diffusivity (AD), and radial diffusivity (RD) are generated by a single tensor fitting of the diffusion data in the T1-space. The weighted UF mask is applied to each individual's FA, RD and AD images to extract these parameters along the uncinate fasciculus. We refer to these imaging parameters as the imaging indices. For example, the fractional anisotropy extracted using the thresholded probability map is referred to as the FA index instead of FA as they represent the imaging parameters weighted by their respective probabilities.

A mean of these weighted imaging parameters, one from each hemisphere, is extracted to investigate whether the left and right hemispheres age differently or affect the behavior of the monkeys in a different way. An average of the values from the left and the right hemispheres is used to study the global effect.

The experiment is repeated again in the diffusion space where the weighted connectivity map is used to extract the FA, AD, and RD measures obtained from a single tensor fitting of diffusion data in the low-resolution space.

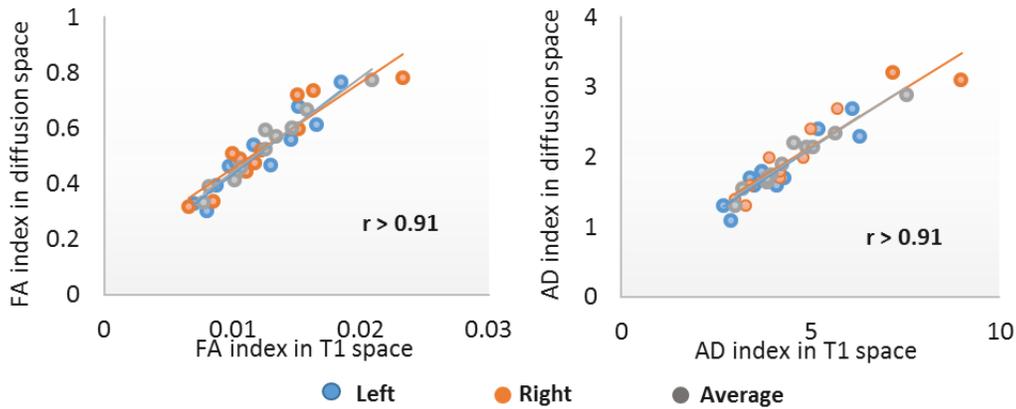


*Figure 3-8: Scatter plot of imaging measures from diffusion space and T1-weighted space. There is a strong correlation between the DTI imaging parameters extracted along the uncinate fasciculus in the two spaces.*

Figure 3-8 shows a scatter plot of the extracted DTI imaging parameters in the high-resolution T1 space vs the low-resolution diffusion space. The data from both these spaces show a high correlation. It was therefore decided to perform all analysis in the T1-space.

### 3.3.1 HARDI parameters

The number of streamlines along the uncinate fasciculus identified by the iFOD2 probabilistic streamlines algorithm (Tournier, Calamante et al. 2010) in each animal is noted. These streamlines depend on the seed amygdala volume. A larger number of voxels in amygdala would result in more streamlines being initiated. Therefore, to use the number of streamlines between OFC and amygdala as a metric for comparison, the streamlines are normalized by the seed volume. This is done by dividing the number of streamlines in each animal by the volume of the corresponding amygdala and then multiplying by the average volume of the amygdala across all subjects. The left and the right hemispheres are treated independently during normalization.

## 3.4 Statistical Analysis

### 3.4.1 Assessing relationship between age and imaging parameters

The mean FA, AD, RD values as well as the number of streamlines generated in each monkey for the left, right and average of the two hemispheres are separated into two groups - young and aged. Assuming that the imaging measures from the two groups follow a normal distribution, a two-tailed student's t-test is performed. The null hypothesis is that there is no difference in the means of the imaging measures between the young and the aged monkeys. The null hypothesis would be rejected for  $\alpha < 0.05$ .

A linear regression is also performed with age as an independent variable and the imaging measures as dependent variables to understand the correlation between age and the parameters along UF.

#### 3.4.1.1 Group Analysis

Figure 3-9 shows a bar plot of the mean fractional anisotropy index for the left, right and the average of two hemispheres across young and aged monkeys. The error bars on the plot represent the standard error of means and the p-values are displayed on the bar plots. The mean FA index values of the young monkeys in blue are higher than that of the older monkeys in gray.

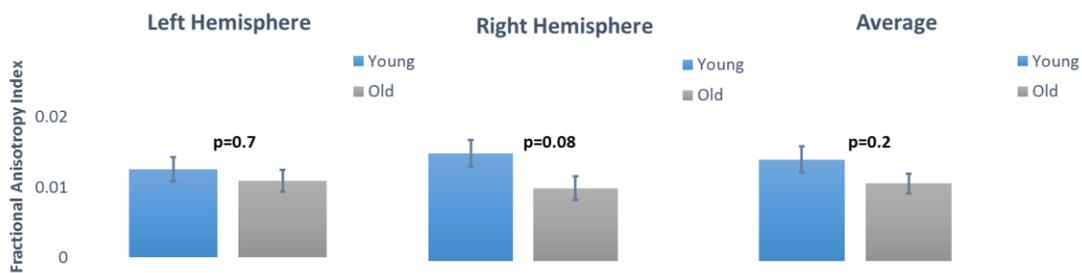


Figure 3-9: A comparison of the mean fractional anisotropy index between the young and aged group of monkeys. The error bars represent standard error of means.

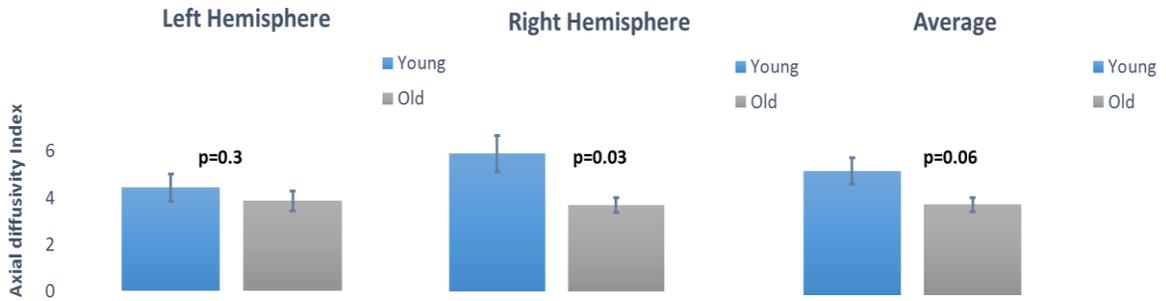


Figure 3-10: A comparison of the mean axial diffusivity index between the young and aged group of monkeys. There is a significant difference between the axial diffusivities in the right hemisphere of the two groups.

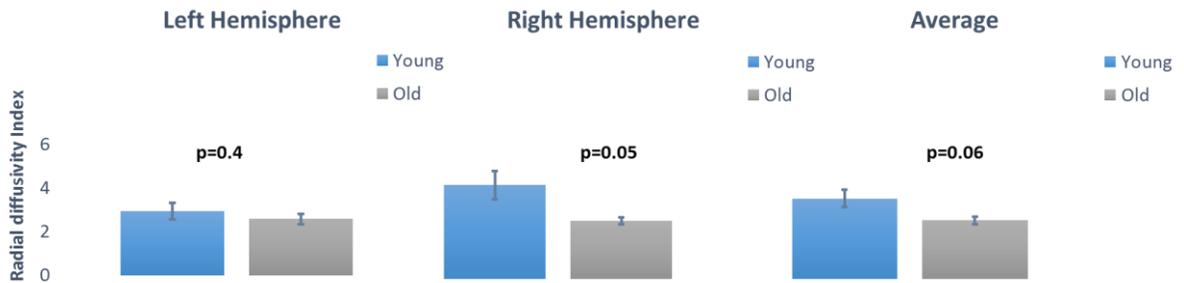


Figure 3-11: A comparison of the mean radial diffusivity index between the young and the aged group of monkeys. The difference in the right hemisphere is close to significant values, with the older monkeys in the group having a smaller radial diffusivity on average.

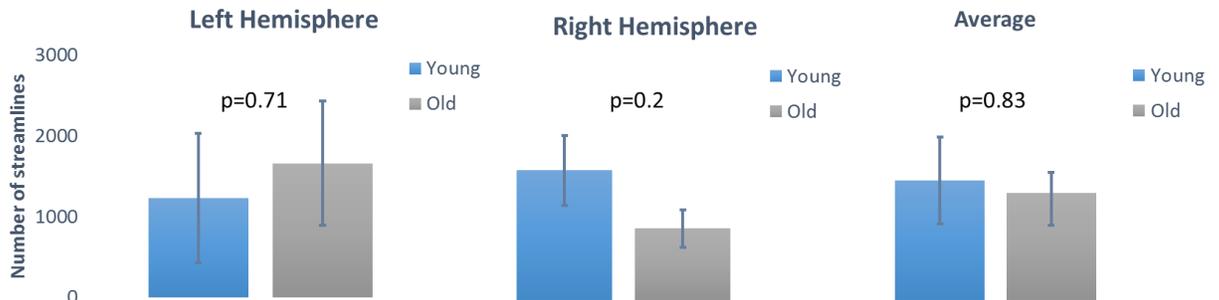


Figure 3-12: A comparison of the number of tracts between the amygdala and the orbitofrontal cortex in young and the aged group of monkeys. The tracts were identified by a FOD based tractography algorithm and were normalized by the seed amygdala

Although none of the means reach significance differences, the mean FA index in the right hemisphere is closer to the significance value of 0.05. Figure 3-10 and Figure 3-11 show the changes in axial and radial diffusivity between the two groups. Figure 3-12 shows the group differences in the number of streamlines that constitute the uncinate fasciculus. The mean number of UF tracts in the young monkeys are higher in the right hemisphere than the older monkeys but the values do not reach significant levels.

#### 3.4.1.2 *Regression Analysis*

Although a group analysis was indicative of differences between the two groups, a linear regression was performed to assess if any of the imaging indices have a linear relationship with age. A least squares fit was performed with the imaging measures as the dependent variable and age as an independent variable. Figure 3-13 shows the relationship between age and the imaging parameters- FA index, RD index and AD index. Pearson's correlation coefficient 'r' and the statistical significance 'p' of the relationship are also displayed on the scatter plots. The age of the monkey being a criterion for inclusion in the study meant a wide age-gap between the two groups. As such, the age was not truly a continuous variable for the scatter plots.

From the scatter plots, it is clear that a strong negative correlation exists between age and the FA index. In other words, older monkeys in the study exhibit a reduced lower FA index along the UF when compared to their younger counterparts. The reduction in the FA index values with age is more significant in the right hemisphere than the left. The AD index scatter plot show a similar trend, consistent with the general consensus that with age there is a reduction in the axial diffusivity. The relationship between the RD index and age however produced an interesting result. A strong negative correlation was observed between age and the RD index such that the measured radial diffusivity index along the UF reduced with age. It has been widely reported in the literature that radial diffusivity has a strong positive correlation with age that shows up as an increase in diffusion perpendicular to the axonal bundles. The case of increased radial diffusivity in the younger bonnet monkeys is investigated in the discussion section.

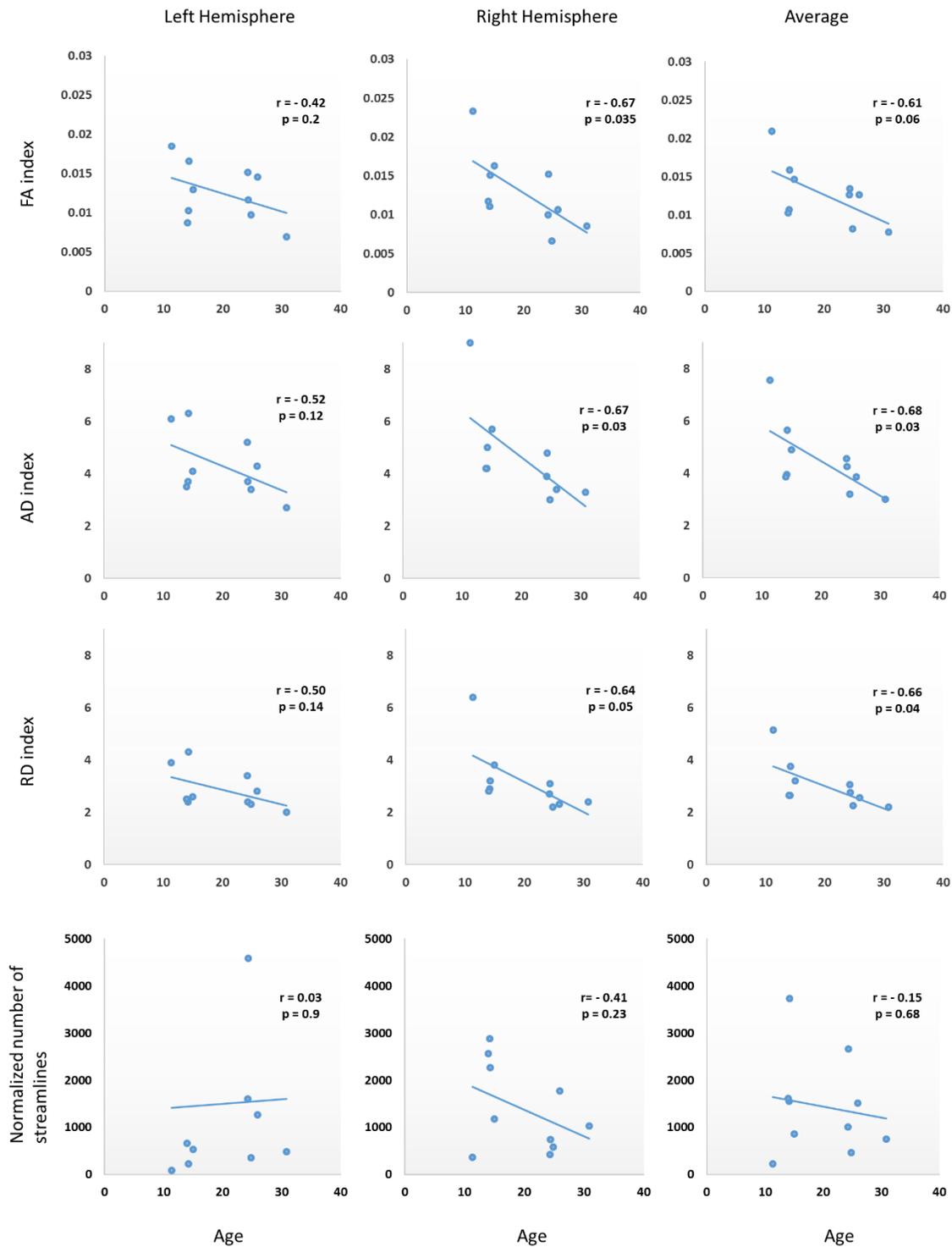


Figure 3-13: Scatter plots showing the relationship between imaging parameters and age. From top to bottom, the imaging parameters are fractional anisotropy, axial diffusivity, radial diffusivity and the number of streamlines normalized by the amygdala volume. The columns from left to right are left hemisphere, right hemisphere and the average of the two hemispheres. The Pearson's correlation coefficient 'r' and the p-values are depicted on each plot.

### 3.4.2 Assessing relationship between behavioral performance and imaging parameters

The imaging measures were also analyzed against the performance of the monkeys on the different behavioral tasks. The young and aged bonnet macaque monkeys were assessed on a delayed-no-match to sample with interference (DNMS-INT) task as well as an object reversal-learning (RL) task to understand how aging affected their updating and monitoring processes. In the RL task, the number of trials taken by the monkey to learn a reversed object to reward association was noted. Here, a lower number of trials indicate a better performance by the monkey in the test. In the DNMS-INT task, the percentage of successful trials by a monkey was noted, a higher number was indicative of a better performance.

#### 3.4.2.1 Regression Analysis

A linear regression is performed with the reversal learning scores as the independent variable and the imaging parameters as the dependent variables. Figure 3-14 shows plots of the imaging parameters vs the performance score of the bonnet monkeys on the reversal learning tasks. The three columns of plots from left to right are the data from left hemisphere, right hemisphere and the average of the two hemispheres. From top to bottom, the imaging measures are FA index, AD index, RD index and the number of streamlines normalized by the amygdala volume. The Pearson's correlation coefficient and the p value are denoted on the respective plots. There is a negative correlation between the FA index and the RL task scores of the monkeys, that is, monkeys with higher FA took fewer trials to learn the reversed object-reward association. The correlation is stronger in the left hemisphere than the right, but this relationship did not attain significance. The AD index showed stronger negative correlation in the left hemisphere than the FA index but followed the same trend as the FA. The number of UF streamlines showed a negative trend with the RL scores such that animals with fewer tracts took more trials in a RL task. None of the imaging measures could significantly explain the performance of the monkeys on the RL task.

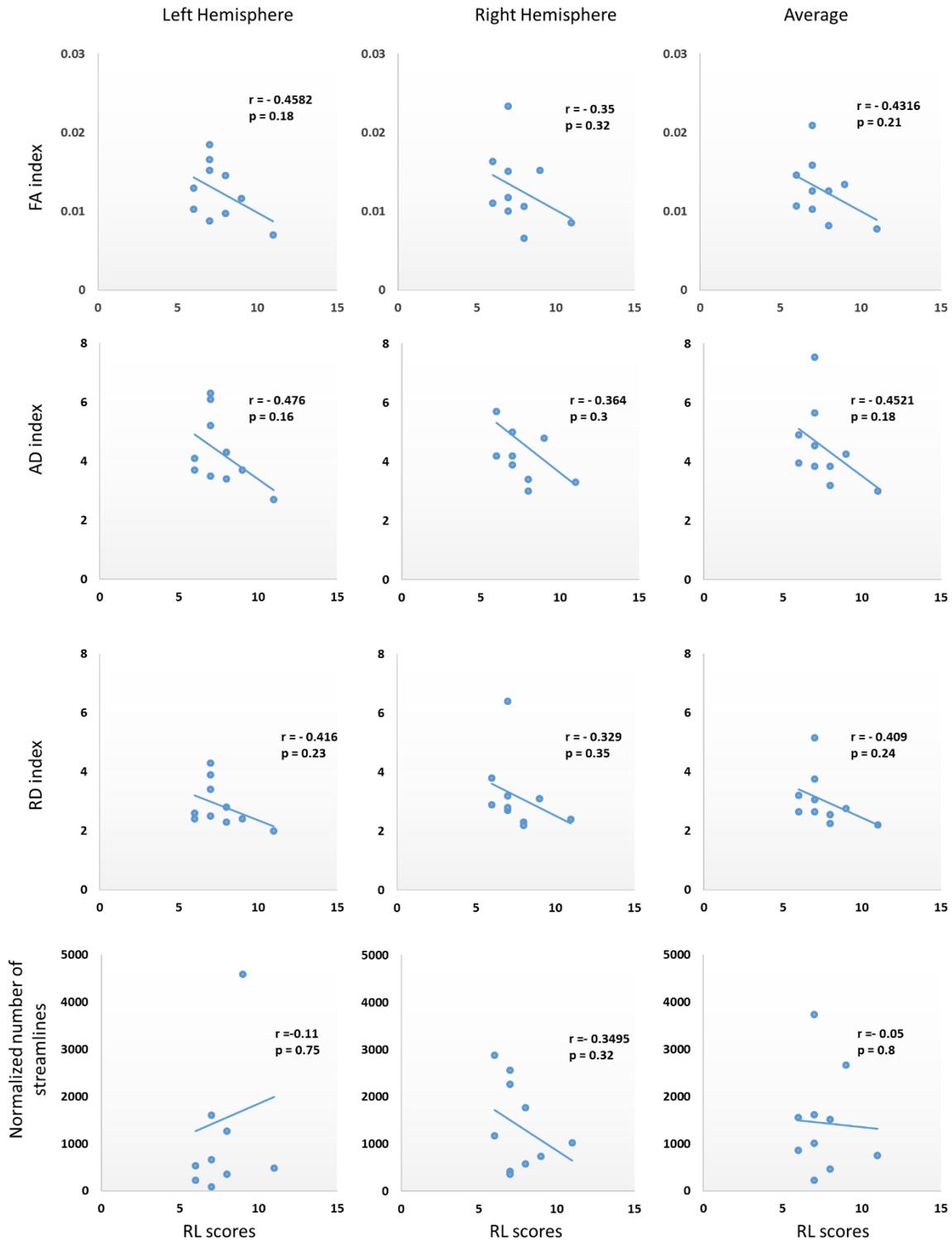


Figure 3-14: Scatter plots showing the relationship between imaging parameters and the performance of monkeys on a reversal-learning task. From top to bottom, the imaging parameters are fractional anisotropy, axial diffusivity, radial diffusivity and the number of streamlines normalized by the amygdala volume. The columns from left to right are left hemisphere, right hemisphere and the average of the two hemispheres. The Pearson's correlation coefficient 'r' and the p-values are depicted on each plot.

Another regression is performed with the performance of the monkeys on a delay no match to sample (DNMS) with interference scores as the independent variable and the imaging parameters as the dependent variables. Figure 3-15 shows plots of the imaging parameters vs the DNMS with interference performance scores. Once again, the imaging measures from top to bottom are FA index, AD index, RD index and the number of streamlines normalized by the amygdala volume. A weak correlation is seen between the FA, AD, RD index and the DNMS with interference scores. The number of streamlines in UF however showed a good positive correlation with the DNMS with interference scores in the right hemisphere such that animals with more streamlines performed better on the tasks. None of the imaging parameters could significantly explain the performance of the monkeys on the DNMS with interference task.

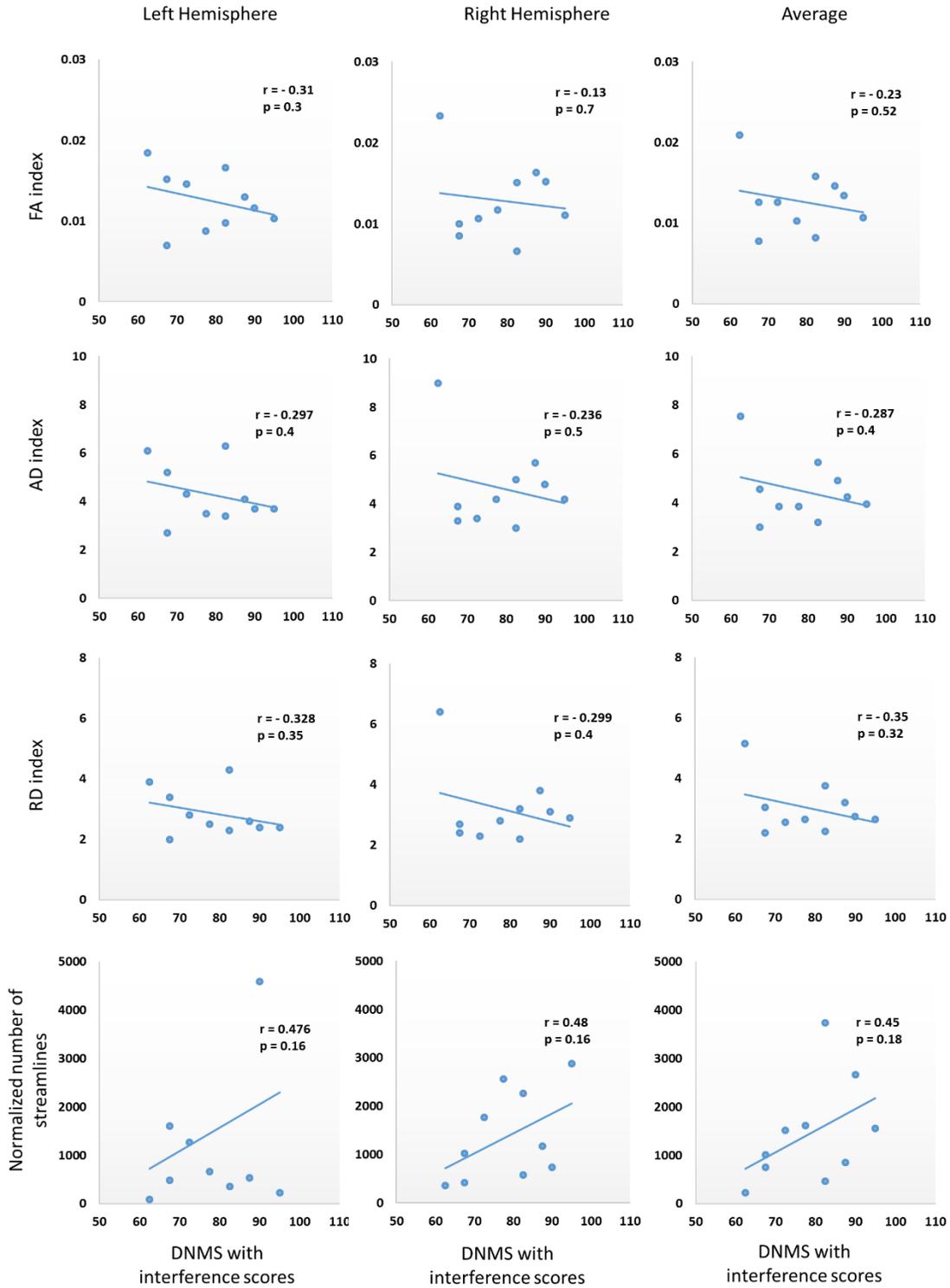


Figure 3-15: Scatter plots showing the relationship between imaging parameters and the performance of monkeys on a delay no match to sample task with interference. From top to bottom, the imaging parameters are fractional anisotropy, axial diffusivity, radial diffusivity and the number of streamlines normalized by the amygdala volume. The columns from left to right are left hemisphere, right hemisphere and the average of the two hemispheres. The Pearson's correlation coefficient 'r' and the p-values are depicted on each plot.

## 3.5 Discussion

From the results presented in section 3.4, it is observed that the fractional anisotropy index in the uncinata fasciculus had a significant positive correlation with age in the right hemisphere but did not significantly affect the performance of the monkeys on a RL task or the DNMS with interference task. The axial diffusivity index in the UF followed a similar trend as the fractional anisotropy index. The radial diffusivity along the UF reduced significantly with age in the subjects under study, with the implication that as the bonnet monkeys grow older, their radial diffusivity reduces. A number of aging studies (Bennett, Madden et al. 2010, Song, Sun et al. 2002, Burzynska, Preuschhof et al. 2010) have reported an increase in the radial diffusivity of the white matter with age, possibly due to de-myelination. To understand the anomalous behavior of radial diffusivity along the UF, it seemed necessary to understand how the diffusivity in the white matter tracts in the entire monkey brain changes with age.

### 3.5.1 Axial and Radial Diffusivity in the white matter along the entire brain

White matter is known to have higher FA values due to their high degree of anisotropy when compared to GM or CSF. Therefore, a white matter mask is created from the FA images by selecting all voxels that have an anisotropy value greater than 0.25. This white matter mask from each subject is applied to the corresponding axial and radial diffusivity images. For each image, value from the white matter is calculated. Figure 3-16 shows a FA image for a bonnet monkey (A) and a white matter mask (B) corresponding to it. The radial diffusivity image (C) and the radial diffusivity extracted along the white matter tracts in the brain (D) are in the bottom row. In the radial diffusivity image (C), the cerebrospinal fluid has the highest diffusion, followed by diffusion in gray matter. The anisotropic nature of white matter greatly restricts diffusion of free water. The contamination from CSF appears as a bright rim in (D) in the voxels adjoining the corpus callosum boundary with CSF. This is due to partial volume effects, an inevitable effect in diffusion MRI due to the size of the imaging voxels. Contamination from CSF can greatly increase diffusivity in a voxel. Figure 3-17 compares the average radial and axial diffusivity along the entire white matter between young and aged monkeys. Both axial ( $p=0.06$ ) and radial diffusivity ( $p=0.2$ ) are higher in the younger monkeys on average when compared to the older ones. The increase observed in radial diffusivity along the uncinata fasciculus is simply an extension of the diffusivities in the underlying white matter.

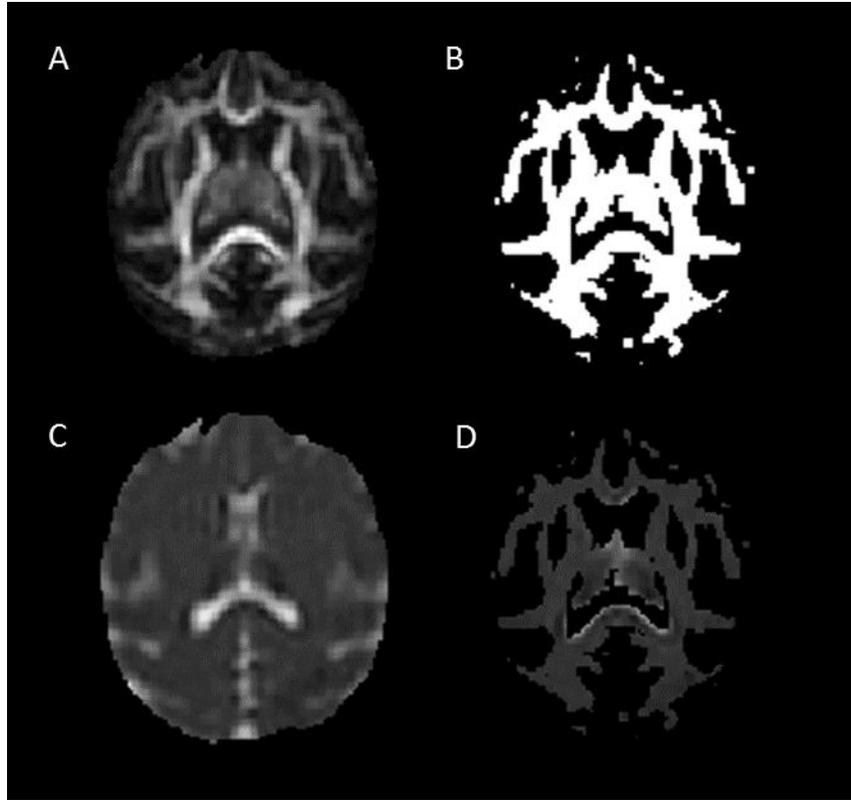


Figure 3-16: Figure shows a fractional anisotropy image (A), a white matter mask (B) obtained from the fractional anisotropy image by applying a threshold of  $FA > 0.25$ , the corresponding radial diffusivity image (C). The white matter mask (B) is applied to the radial diffusivity image to extract the image in (D).

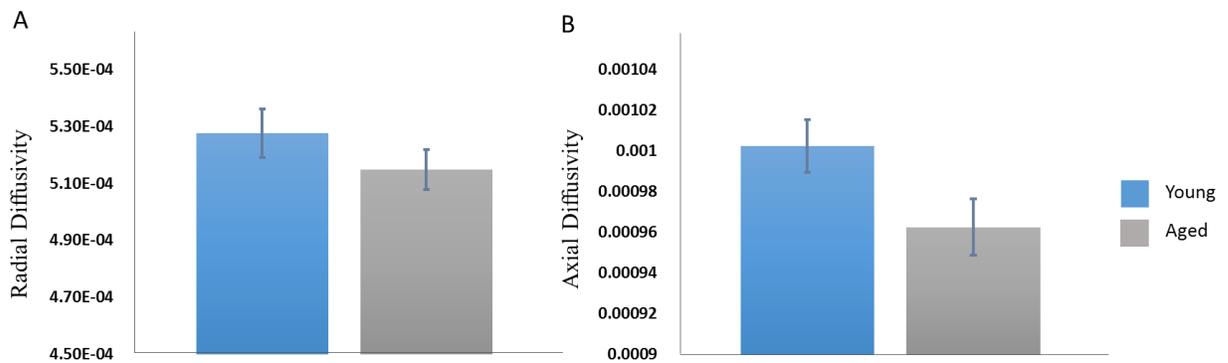


Figure 3-17: A comparison of the average radial diffusivity (A) and axial diffusivity (B) in the white matter voxels in young and aged subjects. For each subject, a white matter mask was applied on the radial and axial diffusivity maps

This reduction in radial diffusivity cannot be interpreted as demyelination in younger bonnet monkeys compared to the older ones without more proof. As explained in (Wheeler-Kingshott, Cercignani 2009), associating changes in eigenvalues to axonal degeneration or de-myelination should be accompanied by a complete study of the tensor models used in the generation of these eigenvalues for each subject. Ground truth can also be established by using post-mortem examinations.

### 3.5.2 Outliers in analysis

None of the imaging parameters correlated significantly with the performance of the monkeys on RL or DNMS with interference tasks. We saw earlier that with age, the FA, AD and RD index reduced significantly. Although not significant, these imaging measures showed a negative correlation with the RL task scores, consistent with the fact that the older monkeys performed poorly on a reversal-learning task when compared to the younger monkeys. On the other hand, the older monkeys have been shown to be at a disadvantage when performing DNMS with interference tasks (Gray, Smith et al. 2016) whereas Figure 3-15 shows a weak but negative correlation, implying animals with higher FA or AD index performed poorly on a DNMS with interference task. On closer inspection of the data, we find that one of the younger monkeys, with a high FA index and a high AD index performed poorly on the DNMS with interference task. It is this one particular data point that drives the negative correlation between the imaging measures and the DNMS with interference performance scores. This outlier is clearly visible in the plots of imaging measures vs DNMS with interference scores in the right hemisphere. To investigate if the relationship between the imaging measures in the right hemisphere would change if we exclude this outlier, regression analysis was repeated.

Figure 3-18 shows relationship of the FA index, AD index and RD index with the DNMS with interference task scores. The outlier monkey has been excluded from analysis and the corresponding plots are shown on the right. The FA and the AD index shows a good positive correlation with the DNMS with interference scores. Higher FA and AD index values correspond to a higher performance on the DNMS with interference task. Increase in RD corresponds to an increase in the performance scores.

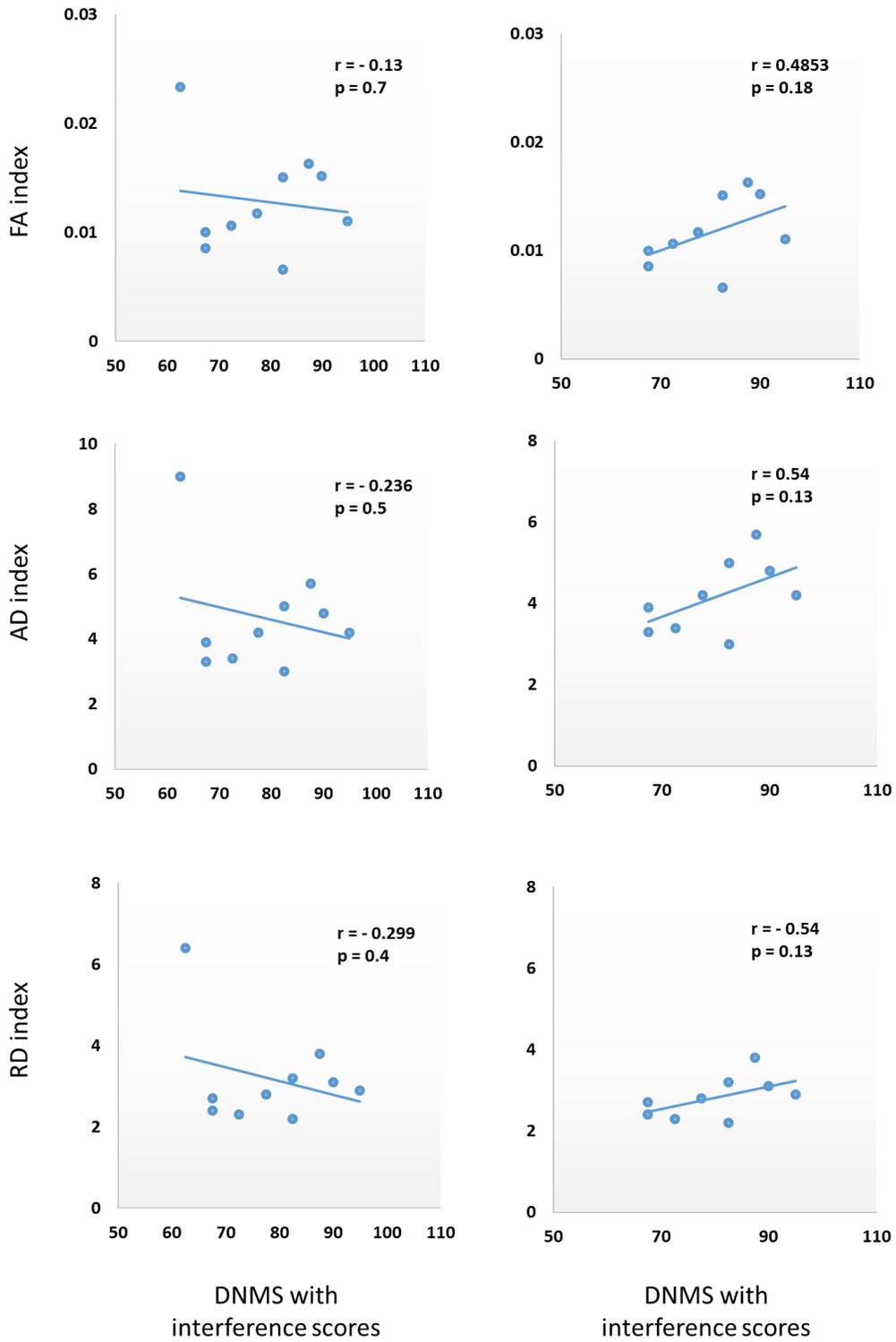


Figure 3-18: Relationship of imaging parameters with DNMS with performance scores. The second column on the right excludes the outlier monkey from regression analysis. The negative correlation of the imaging parameters reverses to a good positive correlation.

This is consistent with the fact that the younger monkeys had higher RD index when compared to the older counterparts. Interestingly, the outlier monkey, with low scores on the DNMS with interference task also had the least number of UF streamlines. As such, a regression analysis excluding the outlier monkey was not necessary for the normalized number of streamlines.

### 3.5.3 Laterality in the uncinate fasciculus

An interesting outcome of this study was the laterality observed in the uncinate fasciculus. In all the comparisons, the right uncinate fasciculus exhibited stronger correlations with the imaging parameters when compared to the left uncinate fasciculus. The findings in DTI literature are mixed regarding, the prominent hemisphere. Some authors report a leftward bias in the FA values and the UF volume (Rodrigo, Oppenheim et al. 2007, Hasan, Iftikhar et al. 2009) whereas other studies using DTI (Craig, Catani et al. 2009, Highley, Walker et al. 2002) and post-mortem dissections have reported a rightward bias in the uncinate fasciculus volume and FA values. Other studies suggest that some parts of the UF tracts have more hemispherical bias than others (Rodrigo, Oppenheim et al. 2007, Kubicki, McCarley et al. 2007, Von Der Heide, Skipper et al. 2013).

## 3.6 Conclusion

A group of young and aged bonnet macaque monkeys were imaged using diffusion-weighted MRI to understand if the strength of the uncinate fasciculus affected the orbitofrontal cortex- amygdala interactions. These interactions have been shown to affect the ability of an animal to make reward based decisions. DTI and HARDI based imaging measures were extracted from the processed diffusion-weighted MR images of the monkeys and were compared to age and the performance of the monkeys on behavioral tasks. The fractional anisotropy index and the axial diffusivity index significantly reduced with age, so did the radial diffusivity index. This pattern of increased radial diffusivity in the younger monkeys compared to the old ones was also observed in the white matter of the entire brain for the monkeys. The imaging measures also showed a negative correlation with the reversal learning trials and a positive correlation with the delay no match to sample with interference performance scores.

## APPENDIX A Local Principal Component Analysis based Filtering in x-q space

As described in Chapter 1, images acquired at each point in q-space are generated by playing diffusion gradients at a specific orientation, gradient strength and diffusion time interval. In a single shell HARDI acquisition, diffusion images collected at a given b-value and diffusion time interval can be interpreted as points on the surface of a unit sphere in q-space. The diffusion images corresponding to q-vectors along orientation  $v$  and  $-v$  will have similar intensities. This similarity can be extended to directions that are not exactly opposite but close enough. Figure A.1 (A) shows the q-vectors corresponding to the 72 diffusion directions, marked in gray, spread on the surface of a unit sphere. The vector corresponding to a direction of interest is shown in green and the q-vectors in red are the first five orientations that are closest to the red vector on the surface of the sphere. Figure A.1 (B) shows the projection of the b-vectors on to a 2D plane for better visualization. The only gray colored vector that appears to be close to the green vector is the q-vector at the center of the sphere corresponding to the B0 images; this point is equidistant from all the points on the surface of the sphere.

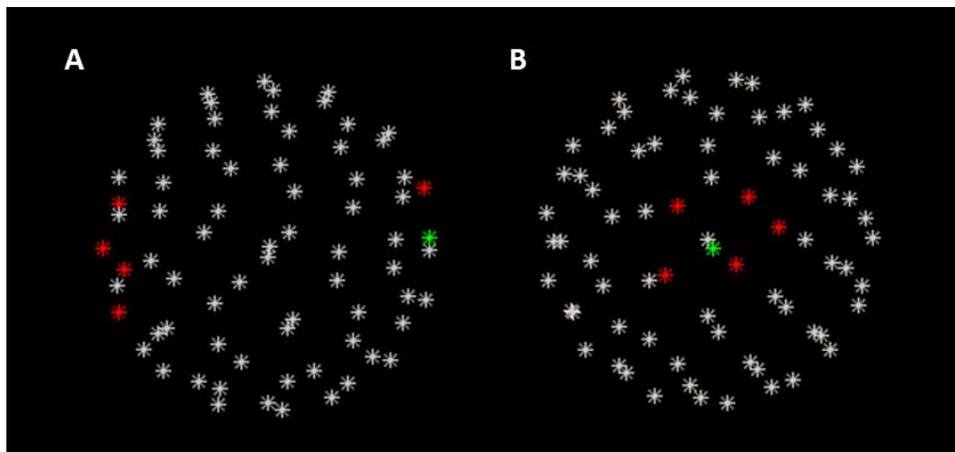
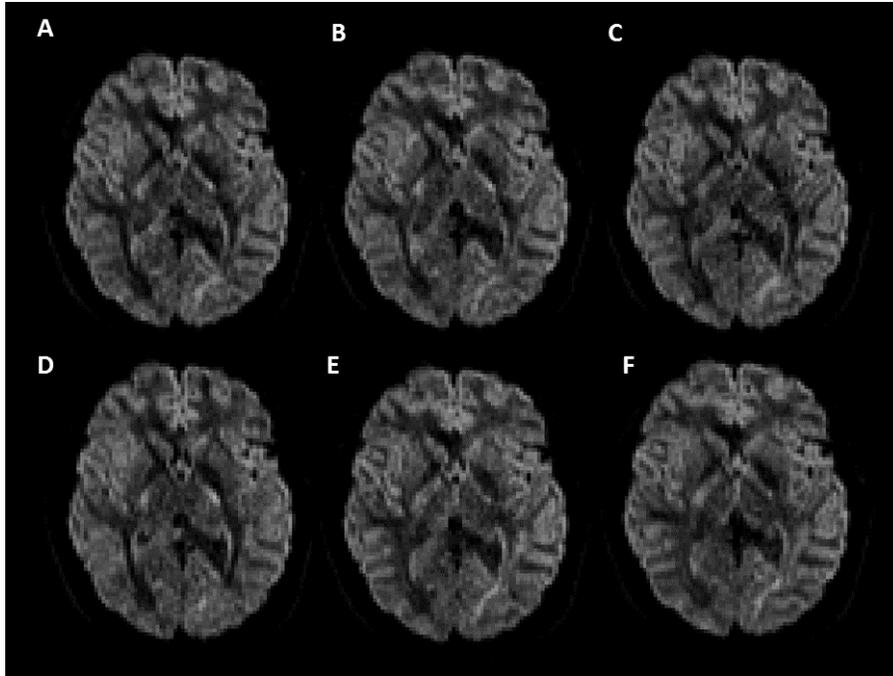


Figure A.1: (A) shows a select orientation (in green) and five directions (red) closest to it. The projection of the b-vectors on the sphere on a 2D plane is shown in (B).

Figure A.2 shows an axial slice of the diffusion-weighted image corresponding to the vector marked in green in the Figure A.1. The images next to it correspond to the q-vectors in red that are closest to the first direction; arranged in the order of increasing distances. This corroborates our theory that the q-vectors that are closer to each other on the surface of the sphere will yield diffusion-weighted images with similar intensities.



*Figure A.2: DW images corresponding to the closest directions highlighted in Figure A.1. The images are in the order of increasing distances from the direction of interest. Note the similarities in signal intensities.*

Our assumption is that given a large number of diffusion directions spread out on the surface of the sphere in q-space, the signal from a smaller subset of gradient directions that are closer to each other would have an even sparser representation in the principal component analysis (PCA) space. This data redundancy along similar directions can be utilized with the PCA based filtering approach discussed in Chapter 2 (Manjón, Coupé et al. 2013) to get better separation between noise and valuable signal information. The difference between the two techniques is that instead of obtaining a principal component basis over all diffusion directions in a local region of the image, a sparser basis is obtained over a smaller subset of directions.

We call this approach directionally constrained x-q space filtering. The algorithm consists of the following steps:

- For each diffusion direction, identify N-1 other diffusion direction similar to it.
- Performing filtering of diffusion-weighted images in local patches for every set of N similar directions.

### A.1 Finding the nearest neighbor

The shortest distance between any two vectors in Cartesian space is given by the Euclidean distance between them. This formulation, however, cannot be used for points on the surface of a sphere; the distances no longer being linear. Instead, the angle between the two vectors in a spherical coordinate system is used as a metric to quantify angular distances. The larger the angular separation between the two vectors, the farther away the two vectors are on the surface of the sphere. For any two vectors  $\vec{r}_1$  and  $\vec{r}_2$ , the separation between them is given by the cosine of the angle between them.

$$\cos(\theta) = \vec{r}_1 \cdot \vec{r}_2 = x_1x_2 + y_1y_2 + z_1z_2$$

Note that we use the cosine of the angle and not the angle itself as a distance measure. For all angles up to  $2\pi$ ,  $\cos(\theta)$  would produce unique values. The distance between two points in q-space is given by:

$$d = -|\cos(\theta)| = -|x_1x_2 + y_1y_2 + z_1z_2|$$

The negative of the absolute value of the cosine ensures that the smaller values of  $\theta$  produce smaller d values. Similar vectors  $v$  and  $-v$  with  $\theta = 180$ , will have  $d = 0$ . For every diffusion-weighted image corresponding to a q-vector, the distance d to every other vector is calculated and the distances are sorted in ascending order. A nearest neighbor matrix is created such that the first column contains the directions of interest and the subsequent entries in each row are the q-vectors that are in increasing order of distances from the first vector. Each row forms a group of similar diffusion directions.

## A.2 Joint Filtering

Similar to the local PCA approach described in Chapter 2, for any voxel in a diffusion-weighted image along a certain orientation, a 3D patch surrounding it is extracted to form a column vector (1 x K). For the voxel in the same spatial location, vectors are extracted from N-1 diffusion directions that are similar to the given orientation. The nearest neighbor matrix created in the previous section is used to identify and select the N diffusion directions closer to a given direction. A matrix X is created such that rows consists of voxels within the 3D patch and the columns correspond to the 3D patches along similar directions.

The covariance matrix of X can be decomposed into

$$C_{xx} = XX^T = U\Sigma U^T$$

The PCA decomposition gives the eigenvalues or the variance in the data in the diagonal matrix  $\Sigma$  and the eigenvectors in matrix U. If an eigenvalue in diagonal matrix  $\Sigma$  is less than the noise variance calculated earlier for the voxel at the center of the 3D patch, the eigenvector corresponding to it is discarded. In other words, we form a new matrix  $\hat{\Sigma}$  with all diagonal entries less than the threshold  $\tau$  set to zero where  $\tau$  corresponds to the noise variance of the voxel being processed.

The inverse PCA transformation that transforms the principal components back to image space is given by:

$$\hat{X} = YU^T \hat{\Sigma}$$

The matrix Y corresponds to the principal components of the data in X and  $U^T$  is the inverse of the eigenvectors U. The matrix  $\hat{\Sigma}$  consists of filtered eigenvalues such that only eigenvectors corresponding to the non-zero eigenvalues contribute to the transformation to the image space. The matrix  $\hat{X}$  contains filtered values corresponding to the 3D patch. This 3D block is now slid such that it is centered at a neighboring voxel and the process is repeated again.

After filtering all the images belonging to a group of similar diffusion directions, we move to a new group and the entire process is repeated again. Since the directions are being filtered in an overcomplete manner, weighted averaging is used to combine the results by assigning higher weights to denoising in which fewer principal component basis were used.

### A.3 Comparison with Local Principal Component Analysis based Denoising

The local principal component based filtering from Chapter 2 and the directionally constrained  $x$ - $q$  space filtering technique were implemented in MATLAB. Figure A.3 shows a diffusion-weighted image (A) and the denoising results from the local principal component based filtering used in Chapter 2 in (B). The image in (C) is the result of filtering using the directionally constrained  $x$ - $q$  space filtering approach. In the second technique, a value of  $N=6$  was chosen i.e. every diffusion direction was filtered with six other diffusion directions.

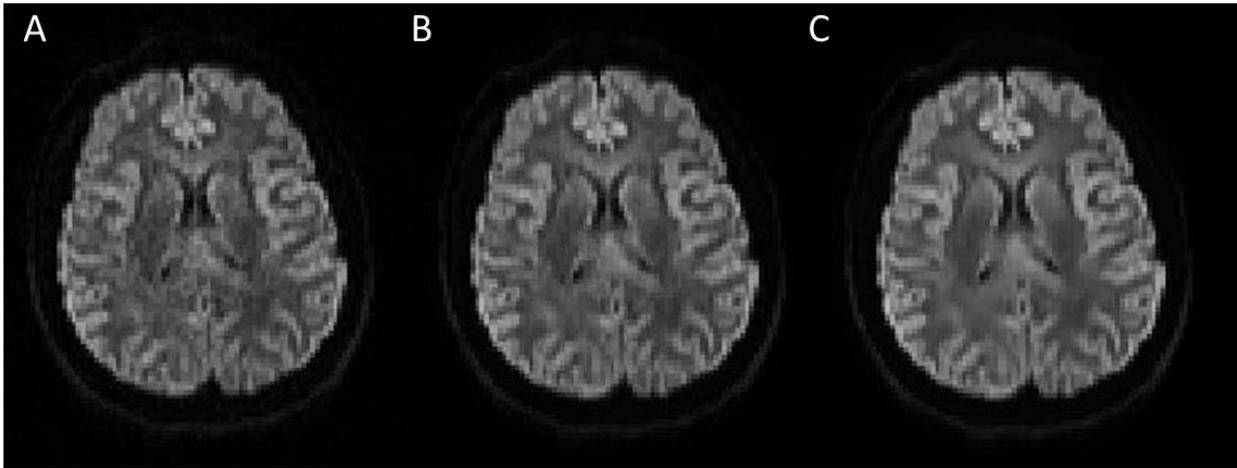


Figure A.3: Diffusion-weighted image corresponding to an axial section of a human brain (A), denoising results from the local principal component analysis based filtering (B) and denoising results from directionally constrained  $x$ - $q$  space filtering (C).

#### A.3.1 Diffusion Computer Phantom for Gold Standard

A noise free diffusion computer phantom available with the Explore DTI toolbox (Leemans, Jeurissen et al. 2009) is used as a gold standard to enable quantitative comparison between the two filtering algorithms. The computer phantom was generated using the following parameters:  $71 \times 71$  matrix size, 1 mm in-plane resolution: 1 mm, 15 slices, 6 B0 images and 60 diffusion directions with  $b=1200 \text{ s/mm}^2$ . Figure A.4 shows a diffusion-weighted image of the computer phantom along a certain orientation in (B). Images C-G show diffusion-weighted images corresponding to  $N=5$  directions obtained from the nearest neighbor matrix. These directions are highlighted in green in image (A).

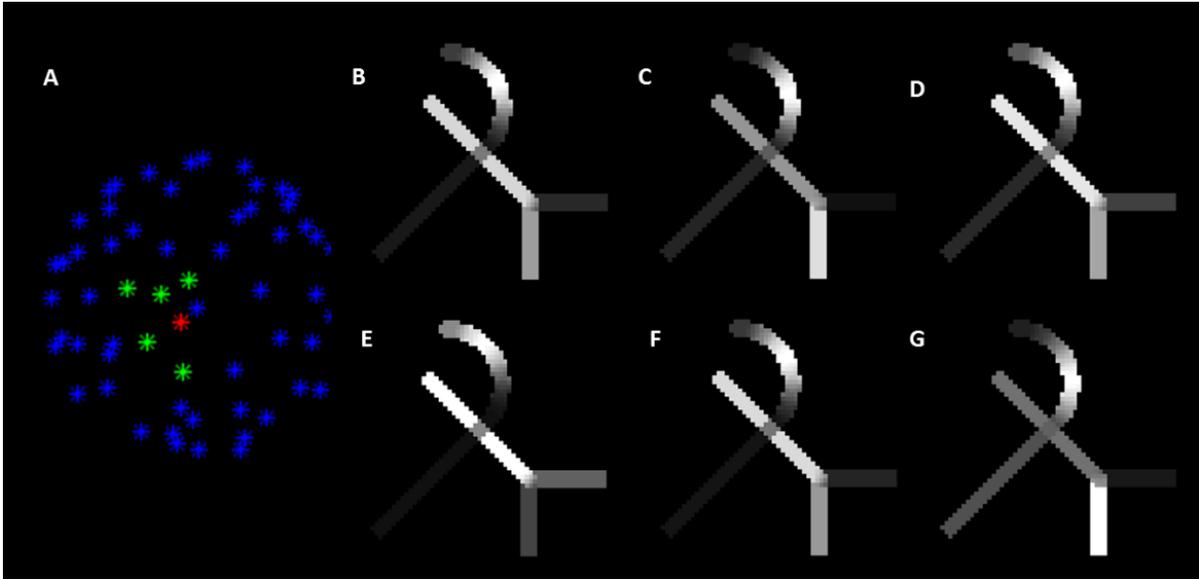


Figure A.4: The diffusion directions displayed on a unit sphere surface in  $q$ -space (A). Red is the direction of interest, with the corresponding DWI image (B). The vectors in green are the five orientations close to the direction in red and the corresponding DW images are shown in (C – G).

### A.3.2 Addition of Noise

To better evaluate the performance of the algorithm Rician noise of known standard deviation is added to the noise free computer phantom images. The noise is added separately to the real and the imaginary components as follows:

$$I_r = S + \eta_1; \quad \eta_1 \sim N(0, \sigma)$$

$$I_i = \eta_2; \quad \eta_2 \sim N(0, \sigma)$$

$$|I_{observed}| = \sqrt{I_r^2 + I_i^2}$$

The standard deviation of noise to be added in the above formulation is determined by a percentage of the maximum image intensity of the B0 image. For e.g. if the maximum image intensity is 255, then addition of a 1% standard deviation noise is equivalent to a noise standard deviation of  $255 * 1/100 = 2.25$ . Figure A.5 shows one such diffusion direction of the computer phantom for different noise levels. With an increase in the level of noise, prominent information corresponds to diffusion of water in the phantom is lost.

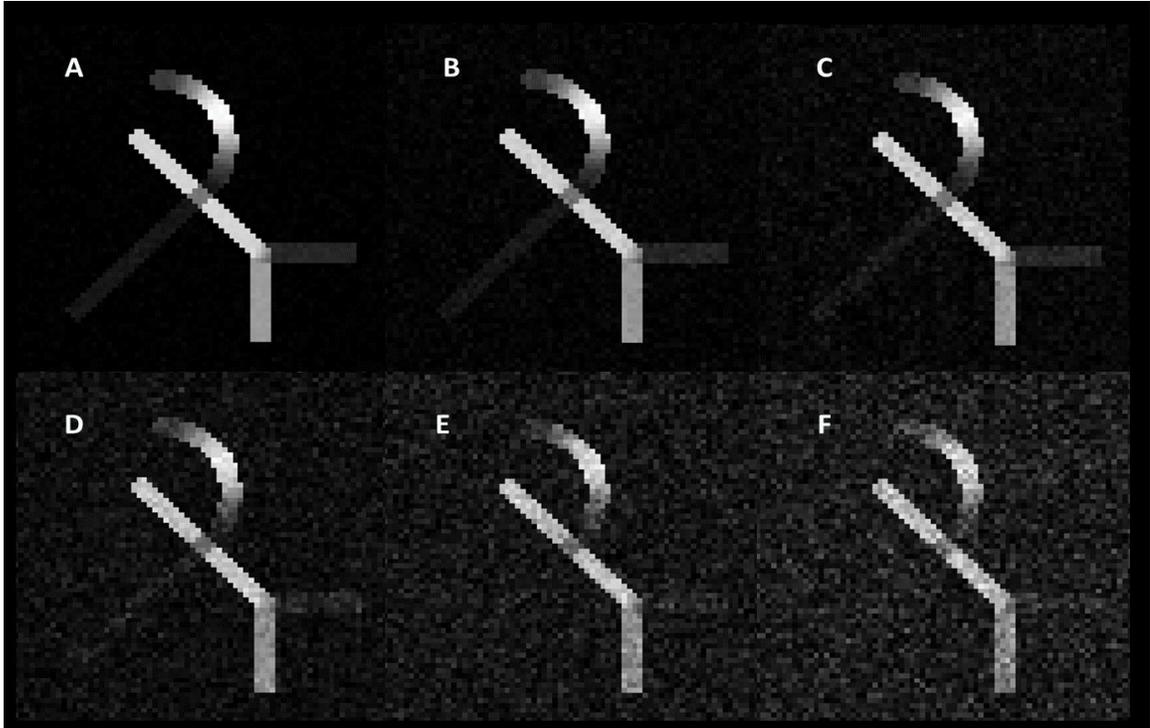


*Figure A.5: Diffusion-weighted image of the computer phantom corrupted by varying levels of Rician noise is shown. Images (A-F) are corrupted by Rician noise of level 1%, 2%, 3%, 5%, 7% and 9% of maximum  $B_0$  image intensity. As the amount of noise in the image increase, valuable signal information is lost.*

### A.3.3 Noise Estimation

A noise estimate in the images is obtained using the Multiple  $B_0$  images based noise estimation technique described in Chapter 2 (Manjón, Coupé et al. 2013). Using the analytical scheme discussed in (Koay, Bassar 2006), a correction is introduced to account for the Rician nature of the noise and compensate for the underestimation of noise standard deviation in regions of low SNR. Application of a low pass filter to the corrected standard deviation map yields a regularized noise map. This map is used to arrive at a threshold for filtering in the two denoising algorithms that we intend to compare. Figure A.6 shows a diffusion-weighted image corrupted by 3% Rician noise (A) and the standard deviation map calculated for every  $3 \times 3 \times 3$  block (B). A regularized noise map (C) is obtained by correcting for Rician noise and applying a low pass filter to (B).

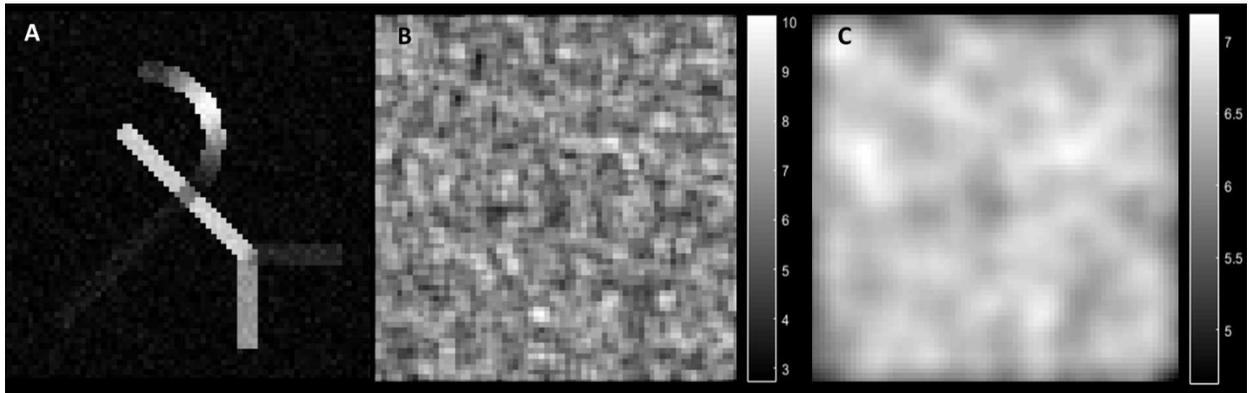


Figure A.6: Diffusion-weighted image corrupted by 3% Rician noise in (A), noise standard deviation estimated in local blocks (B), regularized noise map (C) obtained by low pass filtering the standard deviation map in (B)

#### A.4 Results and Discussion

Denoising is performed on 3% and 7% noise corrupted diffusion-weighted images using the two filtering techniques. The same noise map is used with both the techniques. In directionally constrained x-q space filtering,  $N=12$  is used i.e. a group of 12 diffusion directions are filtered together. The presence of a gold standard enables the comparison of the filtered diffusion signal with the true noise free diffusion signal. Root mean square error in the estimation of each pixel intensity across the different diffusion directions is calculated for the phantom. Figure A.7 shows the root mean square error map for a computer phantom slice for the two filtering techniques for both the noise levels. The top row corresponds to the results on a 3% Rician noise corrupted image whereas the bottom row corresponds to 7% noise. Images (A) and (C) are the results from the local principal component analysis based technique. Images (B) and (D) are the results from the directionally constrained x-q space filtering technique. Darker regions of the image correspond to a low root mean square error in the estimation of true diffusion signal intensities whereas brighter values correspond to larger errors. The error bars for each noise level are presented alongside the images.

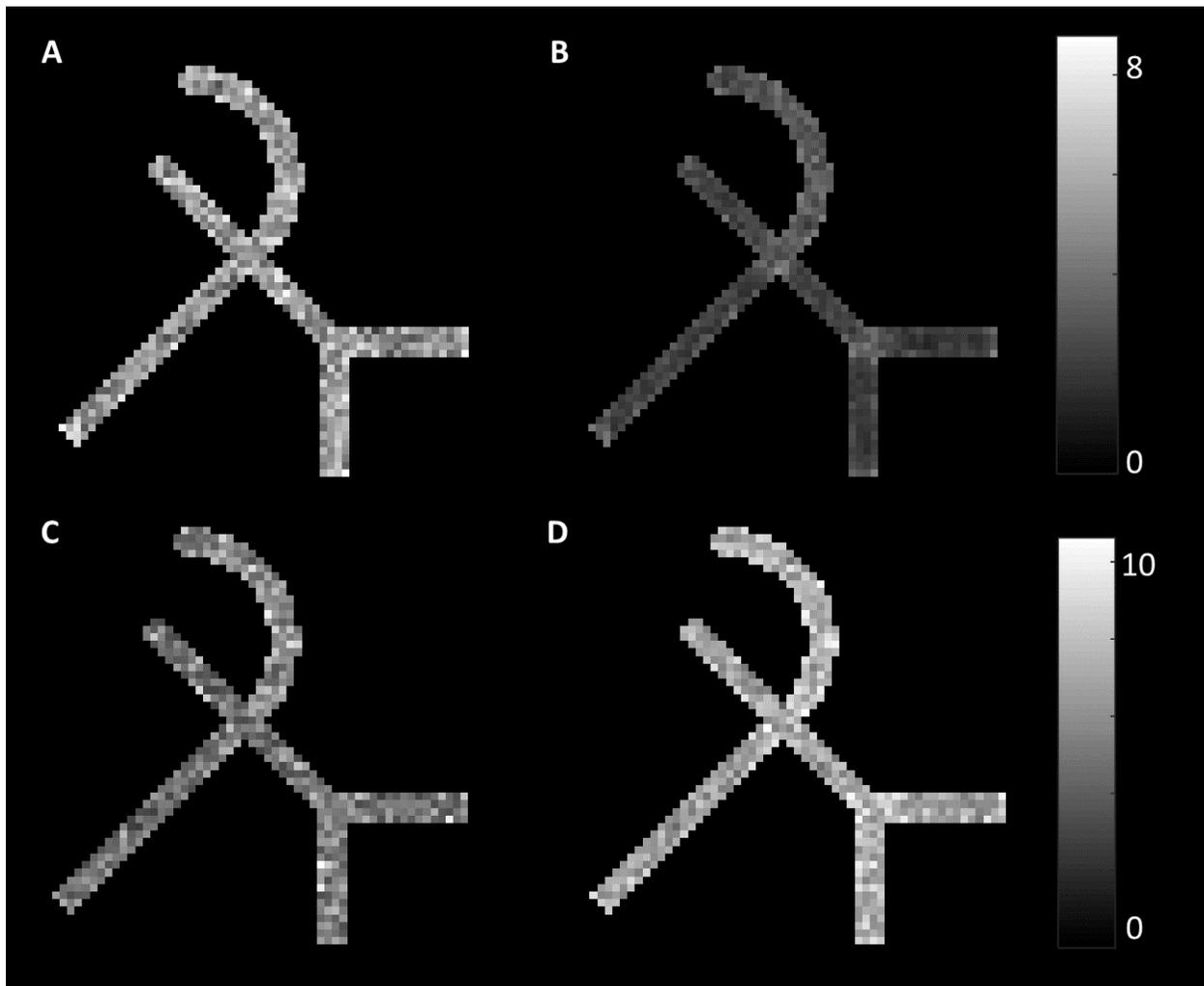


Figure A.7: Root mean square error map for the two noise filtering algorithms at different noise levels. Each pixel represents the root mean square error in the estimation of that pixel across the diffusion directions. The error map for local principal component analysis based denoising method for 3% and 7% Rician noise levels is shown in image (A) and (C). (B) and (E) are the error maps for directionally constrained  $x$ - $q$  space filtering for 3% and 7% Rician noise level respectively.

The noise free diffusion weighted images of the computer phantom are fit to a single tensor model to calculate the fractional anisotropy (FA) images. The results from the noise filtering algorithms is fit to a single tensor model to yield the respective FA images. The root mean square error in the estimation of fractional anisotropy values is used as another metric to compare the performance of the two algorithms. Figure A.8 shows the root mean square error in the estimation of FA values for 5% Rician noise corrupted image filtered by the two filtering algorithms.

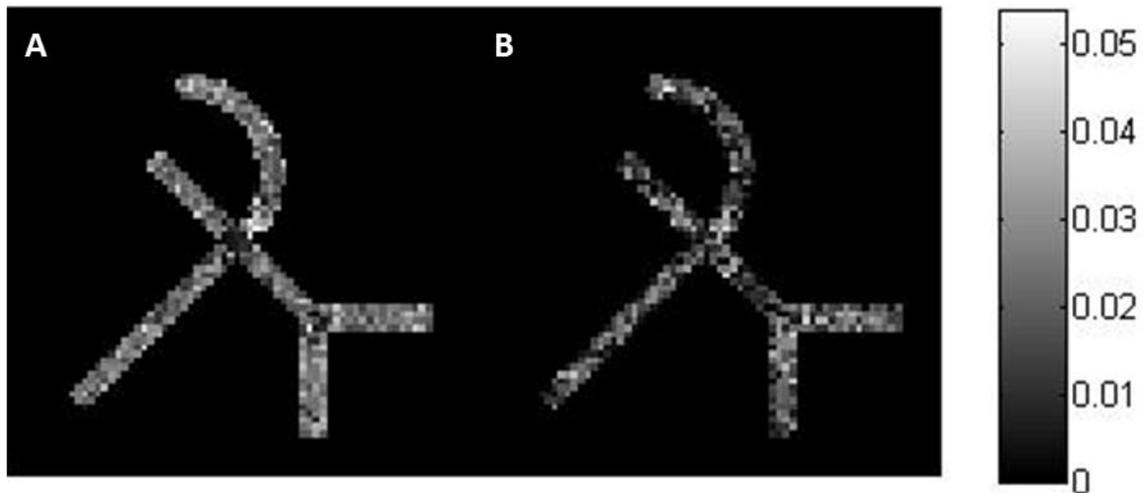
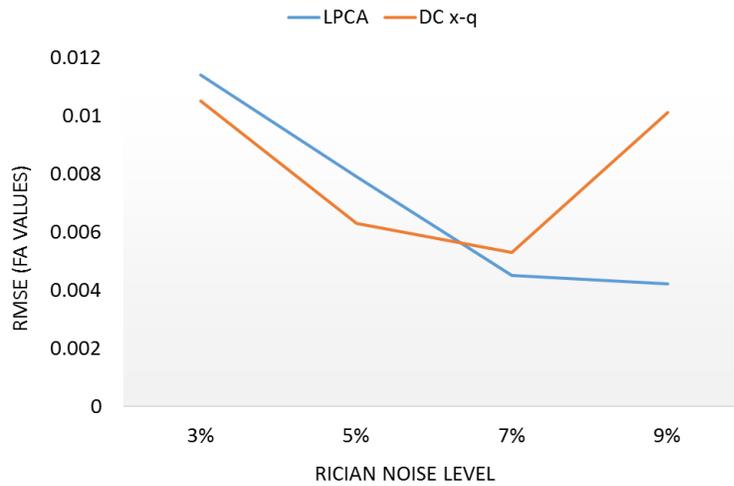


Figure A.8: Root mean square error map for local principal component analysis based filtering technique (A) and directionally constrained x-q space filtering technique (B) at 5% Rician noise. Each pixel represents the root mean square error in the estimation of fractional anisotropy values when compared to the ground truth.

The directionally constrained x-q space filtering technique yielded fractional anisotropy values that were closer to the original FA values than the local principal component analysis based technique. As the level of noise increased, the error in the estimation of the FA values also increased. The root mean square error was calculated for different noise levels from 1% to 9% and a plot was generated that illustrates how the error varies with increase in noise levels. Figure A.9 plots the variations in the root mean square error for FA values with increasing noise levels. This shows that the directionally constrained filtering method performs really well for low noise levels but its efficiency deteriorates as the amount of noise in the images increases. As can be seen from Figure A.5, with increase in noise levels, the signal is completely lost in certain regions of the image that have low signal to noise ratio to begin with. When a group of similar directions are filtered together, the information is corrupted in all such images due to noise and PCA is unable to recover the lost information. In the case of local PCA based noise filtering all the diffusion directions are filtered together, resulting in a higher average SNR in a spatial patch when compared to filtering with only a subset of directions. This enables the local PCA method to capture the variance in the data more effectively and recover the underlying noise corrupted signal.



*Figure A.9: A plot of root mean square error in the estimation of fractional anisotropy in the computer phantom for different levels of Rician noise. For low noise levels, the directionally constrained x-q space filtering technique outperforms the principal component analysis based filtering technique. As the level of Rician noise increases, the performance deteriorates and the error in estimation of fractional anisotropy values increase.*

In conclusion, an alternate principal component analysis based filtering technique that filters groups of diffusion directions across local patches in diffusion images is presented. The algorithm is shown to perform well at low noise levels but further work needs to be performed to improve the robustness of the algorithm at increased noise levels.

## REFERENCES

- ALEXANDER, A.L., LEE, J.E., LAZAR, M. and FIELD, A.S., 2007. Diffusion Tensor Imaging of the Brain. *Neurotherapeutics*, pp. 316-329.
- ANDERSSON, J.L. and SOTIROPOULOS, S.N., 2015. Non-parametric representation and prediction of single-and multi-shell diffusion-weighted MRI data using Gaussian processes. *NeuroImage*, **122**, pp. 166-176.
- ANDERSSON, J.L.R. and SOTIROPOULOS, S.N., 2016. An integrated approach to correction for off-resonance effects and subject movement in diffusion MR imaging. *NeuroImage*, **125**, pp. 1063-1078.
- ASHBURNER, J., 2007. A fast diffeomorphic image registration algorithm. *NeuroImage*, **38**(1), pp. 95-113.
- BASSER, P.J., 1995. Inferring microstructural features and the physiological state of tissues from diffusion-weighted images. *NMR in biomedicine*, pp. 333-344.
- BASSER, P.J. and JONES, D.K., 2002. Diffusion-tensor MRI: theory, experimental design and data analysis - a technical review. *NMR in biomedicine*, pp. 456-467.
- BASSER, P.J., MATTIELLO, J. and LEBIHAN, D., 1994. MR Diffusion Tensor Spectroscopy and Imaging. *Biophysical journal*, pp. 259-267.
- BASSER, P.J., PAJEVIC, S., PIERPAOLI, C., DUDA, J. and ALDROUBI, A., 2000. In Vivo Fiber Tractography Using DT-MRI Data. *Magnetic Resonance in Medicine*, **44**(4), pp. 625-632.
- BASU, S., FLETCHER, T. and WHITAKER, R., 2006. Rician Noise Removal in Diffusion Tensor MRI. In: R. LARSEN, M. NIELSEN and J. SPORRING, eds, *Medical Image Computing and Computer-Assisted Intervention -- MICCAI 2006: 9th International Conference, Copenhagen, Denmark, October 1-6, 2006. Proceedings, Part I*. Berlin, Heidelberg: Springer Berlin Heidelberg, pp. 117-125.
- BEAULIEU, C., 2002. The basis of anisotropic water diffusion in the nervous system - a technical review. *NMR in biomedicine*, pp. 435-455.
- BEHRENS, T.E., BERG, J.H., JBABDI, S., RUSHWORTH, M.F. and WOOLRICH, M.W., 2007. Probabilistic diffusion tractography with multiple fiber orientations: What can we gain? *NeuroImage*, pp. 144-155.
- BEHRENS, T.J., WOOLRICH, M.W., JENKINSON, M., JOHANSEN-BERG, H., NUNES, R.G., CLARE, S., MATTHEWS, P.M., BRADY, J.M. and SMITH, S.M., 2003. Characterization and propagation of uncertainty in diffusion-weighted MR imaging. *Magnetic Resonance in Medicine*, pp. 1077-1088.

- BENNETT, I.J., MADDEN, D.J., VAIDYA, C.J., HOWARD, D.V. and HOWARD, J.H., 2010. Age-related differences in multiple measures of white matter integrity: A diffusion tensor imaging study of healthy aging. *Human brain mapping*, **31**(3), pp. 378-390.
- BIHAN, D.L., 2003. Looking into the functional architecture of the brain with diffusion MRI. *Nature Reviews Neuroscience*, pp. 469-480.
- BODAMMER, N., KAUFMANN, J., KANOWSKI, M. and TEMPELMANN, C., 2004. Eddy current correction in diffusion-weighted imaging using pairs of images acquired with opposite diffusion gradient polarity. *Magnetic Resonance in Medicine*, **51**(1), pp. 188-193.
- BURKE, S.N., THOME, A., PLANGE, K., ENGLE, J.R., TROUARD, T.P., GOTHARD, K.M. and BARNES, C.A., 2014. Orbitofrontal Cortex Volume in Area 11/13 Predicts Reward Devaluation, But Not Reversal Learning Performance, in Young and Aged Monkeys. *The Journal of Neuroscience*, **34**(30), pp. 9905-9916.
- BURZYNSKA, A.Z., PREUSCHHOF, C., BÄCKMAN, L., NYBERG, L., LI, S.-., LINDENBERGER, U. and HEEKEREN, H.R., 2010. Age-related differences in white matter microstructure: Region-specific patterns of diffusivity. *NeuroImage*, **49**(3), pp. 2104-2112.
- CALLAGHAN, P., ECCLES, C. and XIA, Y., 1988. NMR microscopy of dynamic displacements: k-space and q-space imaging. *Journal of Physics E: Scientific Instruments*, pp. 820-822.
- CASEY, B.J., GIEDD, J.N. and THOMAS, K.M., 2000. Structural and functional brain development and its relation to cognitive development. *Biological psychology*, **54**(1-3), pp. 241-257.
- CATANI, M., THIEBAUT DE SCHOTTEN and M., 2008. A diffusion tensor imaging tractography atlas for virtual in vivo dissections. *Cortex*, pp. 1105-1132.
- CATANI, M. and MESULAM, M., 2008. The arcuate fasciculus and the disconnection theme in language and aphasia: History and current state. *Cortex*, **44**(8), pp. 953-961.
- CHAN, R.W., VON DEUSTER, C., GIESE, D., STOECK, C.T., HARMER, J., AITKEN, A.P., ATKINSON, D. and KOZERKE, S., 2014. Characterization and correction of eddy-current artifacts in unipolar and bipolar diffusion sequences using magnetic field monitoring. *Journal of Magnetic Resonance*, **244**, pp. 74-84.
- COOK, I.A., BOOKHEIMER, S.Y., MICKES, L., LEUCHTER, A.F. and KUMAR, A., 2007. Aging and brain activation with working memory tasks: an fMRI study of connectivity. *International Journal of Geriatric Psychiatry*, **22**, pp. 332-342.
- CRAIG, M.C., CATANI, M., DEELEY, Q., LATHAM, R., DALY, E., KANAAN, R., PICCHIONI, M., MCGUIRE, P.K., FAHY, T. and MURPHY, D.G.M., 2009. Altered connections on the road to psychopathy. *Molecular psychiatry*, **14**(10), pp. 946-953.

EINSTEIN, A., 1905. Investigations on the theory of The Brownian Movement. *Ann. der Physik*, **17**, pp. 549

FEDOROV, A., BEICHEL, R., KALPATHY-CRAMER, J., FINET, J., FILLION-ROBIN, J., PUJOL, S., BAUER, C., JENNINGS, D., FENNESSY, F., SONKA, M., BUATTI, J., AYLWARD, S., MILLER, J.V., PIEPER, S. and KIKINIS, R., 2012. 3D Slicer as an image computing platform for the Quantitative Imaging Network. *Magnetic resonance imaging*, **30**(9), pp. 1323-1341.

FELDMAN, H.M., YEATMAN, J.D. and GAMAN-BEAN, S., 2010. Diffusion Tensor Imaging: A review for Pediatric Researchers and Clinicians. *Journal of developmental and behavioral pediatrics*, pp. 346-356.

FSL 5.0 Toolbox Available: <http://fsl.fmrib.ox.ac.uk/fsl/fslwiki/FDT>.

GAFFAN, D. and WILSON, C.R.E., 2008. Medial temporal and prefrontal function: Recent behavioral disconnection studies in the macaque monkey. *Cortex*, **44**(8), pp. 928-935.

GALANTUCCI, S., TARTAGLIA, M.C., WILSON, S.M., HENRY, M.L., FILIPPI, M., AGOSTA, F., DRONKERS, N.F., HENRY, R.G., OGAR, J.M., MILLER, B.L. and GORNO-TEMPINI, M.L., 2011. White matter damage in primary progressive aphasia: a diffusion tensor tractography study. *Brain*

GAZZALEY, A., COONEY, J., RISSMAN, J. and D'ESPOSITO, M., 2005. Top-down suppression deficit underlies working memory impairment in normal aging. *Nature neuroscience*, pp. 1298-1300.

GHASHGHAEEI, H.T. and BARBAS, H., 2002. Pathways for emotion: interactions of prefrontal and anterior temporal pathways in the amygdala of the rhesus monkey. *Neuroscience*, **115**(4), pp. 1261-1279.

GHASHGHAEEI, H.T., HILGETAG, C.C. and BARBAS, H., 2007. Sequence of information processing for emotions based on the anatomic dialogue between prefrontal cortex and amygdala. *NeuroImage*, **34**(3), pp. 905-923.

GRAY, D.T., SMITH, A.C., BURKE, S.N., GAZZALEY, A. and BARNES, C.A., 2016. Attentional updating and monitoring and affective shifting are impacted independently by aging in macaque monkeys. *Behavioural brain research*.

GREVE, D.N. and FISCHL, B., 2009. Accurate and robust brain image alignment using boundary-based registration. *NeuroImage*, **48**(1), pp. 63-72.

HAGMANN, P., KURANT, M., GIGANDET, X., THIRAN, P., WEDEEN, V.J. and MEULI, R., 2007. *Mapping Human Whole-Brain Structural Networks with Diffusion MRI*.

HAHN, E.L., 1950. Spin Echoes. *Physical Review*, **80**(4), pp. 580.

- HANSEN, P.C., 1994. REGULARIZATION TOOLS: A Matlab package for analysis and solution of discrete ill-posed problems. *Numerical Algorithms*, **6**(1), pp. 1-35.
- HASAN, K.M., IFTIKHAR, A., KAMALI, A., KRAMER, L.A., ASHTARI, M., CIRINO, P.T., PAPANICOLAOU, A.C., FLETCHER, J.M. and EWING-COBBS, L., 2009. Development and aging of the healthy human brain uncinate fasciculus across the lifespan using diffusion tensor tractography. *Brain research*, **1276**, pp. 67-76.
- HASELGROVE, J.C. and MOORE, J.R., 1996. Correction for distortion of echo-planar images used to calculate the apparent diffusion coefficient. *Magnetic Resonance in Medicine*, **36**(6), pp. 960-964.
- HIGHLEY, J.R., WALKER, M.A., ESIRI, M.M., CROW, T.J. and HARRISON, P.J., 2002. Asymmetry of the Uncinate Fasciculus: A Post-mortem Study of Normal Subjects and Patients with Schizophrenia. *Cerebral Cortex*, **12**(11), pp. 1218-1224.
- HOSEY, T., WILLIAMS, G. and ANSORGE, R., 2005. Inference of multiple fiber orientations in high angular resolution diffusion imaging. *Magnetic Resonance in Medicine*, pp. 1480-1489.
- JEURISSEN, B., TOURNIER, J., DHOLLANDER, T., CONNELLY, A. and SIJBERS, J., 2014. Multi-tissue constrained spherical deconvolution for improved analysis of multi-shell diffusion MRI data. *NeuroImage*, pp. 411-426.
- JEZZARD, P. and BALABAN, R.S., 1995. Correction for geometric distortion in echo planar images from B0 field variations. *Magnetic resonance in medicine*, **34**(1), pp. 65-73.
- JEZZARD, P., BARNETT, A.S. and PIERPAOLI, C., 1998. Characterization of and correction for eddy current artifacts in echo planar diffusion imaging. *Magnetic Resonance in Medicine*, **39**(5), pp. 801-812.
- JONES, D.K., 2010. Diffusion MRI. *Oxford University Press*.
- JONES, D.K. and CERCIGNANI, M., 2010. Twenty-five pitfalls in the analysis of diffusion MRI data. *NMR in biomedicine*, pp. 803-820.
- KOAY, C.G. and BASSER, P.J., 2006. Analytically exact correction scheme for signal extraction from noisy magnitude MR signals. *Journal of Magnetic Resonance*, **179**(2), pp. 317-322.
- KUBICKI, M., MCCARLEY, R., WESTIN, C., PARK, H., MAIER, S., KIKINIS, R., JOLESZ, F.A. and SHENTON, M.E., 2007. A review of diffusion tensor imaging studies in schizophrenia. *Journal of psychiatric research*, **41**(1-2), pp. 15-30.
- KUMAR, R., NGUYEN, H.D., MACEY, P.M., WOO, M.A. and HARPER, R.M., 2012. Regional brain axial and radial diffusivity changes during development. *Journal of neuroscience research*, pp. 346-355.

LE BIHAN, D., POUPON, C., AMADON, A. and LETHIMONNIER, F., 2006. Artifacts and pitfalls in diffusion MRI. *Journal of magnetic resonance imaging*, **24**(3), pp. 478-488.

LEEMANS, A. and JONES, D.K., 2009. The B-matrix must be rotated when correcting for subject motion in DTI data. *Magnetic Resonance in Medicine*, **61**(6), pp. 1336-1349.

LEEMANS, A., JEURISSEN, B., SIJBERS, J. and JONES, D., 2009. ExploreDTI: a graphical toolbox for processing, analyzing, and visualizing diffusion MR data, *Intl Soc Mag Reson Med* 2009.

MAKRIS, N., PAPADIMITRIOU, G.M., VAN DER KOUWE, A., KENNEDY, D.N., HODGE, S.M., DALE, A.M., BENNER, T., WALD, L.L., WU, O., TUCH, D.S., CAVINESS, V.S., MOORE, T.L., KILLIANY, R.J., MOSS, M.B. and ROSENE, D.L., 2007. Frontal connections and cognitive changes in normal aging rhesus monkeys: A DTI study. *Neurobiology of aging*, **28**(10), pp. 1556-1567.

MANJÓN, J.V., COUPÉ, P., CONCHA, L., BUADES, A., COLLINS, L. and ROBLES, M., 2013. Diffusion Weighted Image Denoising Using Overcomplete Local PCA. *PLoS one* 8.9: e73021.

MANSFIELD, P., 1977. Multi-planar image formation using NMR spin echoes. *Journal of Physics: Solid State Physics*, **10**(3), pp. L55.

MORI, S., KAUFMANN, W.E., DAVATZIKOS, C., STIELTJES, B., AMODEI, L., FREDERICKSEN, K., PEARLSON, G.D., MELHEM, E.R., SOLAIYAPPAN, M., RAYMOND, G.V., MOSER, H.W. and VAN ZIJIL, P.C., 2002. Imaging cortical association tracts in the human brain using diffusion-tensor-based axonal tracking. *Magnetic Resonance in Medicine*, **47**(2), pp. 215-223.

MORI, S. and VAN ZIJIL, P.C., 2002. Fiber Tracking: principles and strategies - a technical review. *NMR in biomedicine*, pp. 468-480.

MORI, S. and ZHANG, J., 2006. Principles of Diffusion Tensor Imaging and Its Applications to Basic Neuroscience Research. *Neuron*, **51**(5), pp. 527-539.

MRtrix 3.0 Toolbox Available at: <http://www.mrtrix.org/>.

NIFTI Toolbox. Available at: <https://www.mathworks.com/matlabcentral/fileexchange/8797-tools-for-nifti-and-analyze-image>.

PETRIDES, M. and PANDYA, D.N., 2007. Efferent association pathways from the rostral prefrontal cortex in the macaque monkey. *The Journal of neuroscience*, **27**(43), pp. 11573-11586.

PFEIFFER, S.E., WARRINGTON, A.E. and BANSAL, R., 1993. The oligodendrocyte and its many cellular processes. *Trends in cell biology*, pp. 191-197.

PIERPAOLI, C., WALKER, L., IRFANOGLU, M., BARNETT, A., BASSER, P., CHANG, L., KOAY, C., PAJEVIC, S., ROHDE, G. and SARLLS, J., 2010. TORTOISE: an integrated software package for processing of diffusion MRI data. *Book TORTOISE: An Integrated Software Package for Processing of Diffusion MRI Data (Editor ed^ eds)*, **18**, pp. 1597.

PIERPAOLI, C. and BASSER, P.J., 1996. Towards a quantitative assessment of diffusion anisotropy. *Magnetic Resonance in Medicine*, pp. 893-906.

RAFFELT, D., TOURNIER, J.-., ROSE, S., RIDGWAY, G.R., HENDERSON, R., CROZIER, S., SALVADO, O. and CONNELLY, A., 2012. Apparent Fibre Density: A novel measure for the analysis of diffusion-weighted magnetic resonance images. *NeuroImage*, **59**(4), pp. 3976-3994.

RASMUSSEN, C.E., 2006. Gaussian processes for machine learning.

REESE, T.G., HEID, O., WEISSKOFF, R.M. and WEDEEN, V.J., 2003. Reduction of eddy-current-induced distortion in diffusion MRI using a twice-refocused spin echo. *Magnetic Resonance in Medicine*, **49**(1), pp. 177-182.

ROCHE, A., MALANDAIN, G., PENNEC, X. and AYACHE, N., 1998. The correlation ratio as a new similarity measure for multimodal image registration. In: W.M. WELLS, A. COLCHESTER and S. DELP, eds, *Medical Image Computing and Computer-Assisted Intervention — MICCAI'98: First International Conference Cambridge, MA, USA, October 11–13, 1998 Proceedings*. Berlin, Heidelberg: Springer Berlin Heidelberg, pp. 1115-1124.

RODRIGO, S., OPPENHEIM, C., CHASSOUX, F., GOLESTANI, N., COINTEPAS, Y., POUPON, C., SEMAH, F., MANGIN, J.-., LE BIHAN, D. and MEDER, J.-., 2007. Uncinate fasciculus fiber tracking in mesial temporal lobe epilepsy. Initial findings. *European radiology*, **17**(7), pp. 1663-1668.

ROHDE, G.K., BARNETT, A.S., BASSER, P.J., MARENCO, S. and PIERPAOLI, C., 2004. Comprehensive approach for correction of motion and distortion in diffusion-weighted MRI. *Magnetic Resonance in Medicine*, **51**(1), pp. 103-114.

RORDEN, C., MRICron. Available at: <http://people.cas.sc.edu/rorden/mricron/index.html>.

SALAT, D.H., TUCH, D.S., GREVE, D.N., VAN DER KOUWE, A.J.W., HEVELONE, N.D., ZALETA, A.K., ROSEN, B.R., FISCHL, B., CORKIN, S., ROSAS, H.D. and DALE, A.M., 2005. Age-related alterations in white matter microstructure measured by diffusion tensor imaging. *Neurobiology of aging*, **26**(8), pp. 1215-1227.

SCHMAHMANN, J.D., PANDYA, D.N., WANG, R., DAI, G., D'ARCEUIL, H.E., DE CRESPIGNY, A.J. and WEDEEN, V.J., 2007. Association fibre pathways of the brain: parallel observations from diffusion spectrum imaging and autoradiography. *Brain: a journal of neurology*, **130**, pp. 630-653.

SHENTON, M.E., DICKEY, C.C., FRUMIN, M. and MCCARLEY, R.W., 2001. A review of MRI findings in schizophrenia. *Schizophrenia research*, **49**(1–2), pp. 1-52.

SLED, J.G., ZIJDENBOS, A.P. and EVANS, A.C., 1998. A nonparametric method for automatic correction of intensity nonuniformity in MRI data. *IEEE Transactions on Medical Imaging*, **17**(1), pp. 87-97.

Slicer 3D Toolbox. Available at: <https://www.slicer.org/>.

SONG, S., SUN, S., RAMSBOTTOM, M., CHANG, C., RUSSELL, J. and CROSS, A., 2002. Dysmyelination revealed through MRI as increased radial (but unchanged axial) diffusion of water. *NeuroImage*, pp. 1429-1436.

STEJSKAL, E. and TANNER, J., 1965. Spin Diffusion Measurements: Spin Echoes in the Presence of a Time Dependent Field Gradient. *The Journal of chemical physics*.

SUTTON, B.P., 2009. Image Reconstruction: Off-Resonance Effects and Correction, *Sunrise Educational Session, ISMRM 2009*.

TALAIRACH, P. and TOURNOUX, J., 1988. A stereotactic coplanar atlas of the human brain.

TAX, C.M., JEURISSEN, B., VOS, S.B., VIERGEVER, M.A. and LEEMANS, A., 2014. Recursive calibration of the fiber response function for spherical deconvolution of diffusion MRI data. *NeuroImage*, pp. 67-80.

THIEBAUT DE SCHOTTEN, M., D., F., V., R. and CATANI, M., 2012. Monkey to human comparative anatomy of the frontal lobe association tracts. *Cortex*, , pp. 82-96.

TORTOISE Toolbox. Available at: <https://science.nichd.nih.gov/confluence/display/nihpd/TORTOISE>.

TOURNIER, D.J., CALAMANTE, F. and CONNELLY, A., 2013. Determination of the appropriate b value and the number of gradient directions for high-angular-resolution diffusion-weighted imaging. *NMR in biomedicine*, pp. 1775-1786.

TOURNIER, D.J., CALAMANTE, F. and CONNELLY, A., 2012. MRtrix: Diffusion tractography in crossing fiber regions. *International Journal of Imaging Systems and Technology*, pp. 53-66.

TOURNIER, D.J., CALAMANTE, F. and CONNELLY, A., 2010. Improved probabilistic streamlines tractography by 2nd order integration over fiber orientation distributions. *Proc. 18th Annual Meeting of the Intl. Soc. Mag. Reson. Med.(ISMRM)*.

TOURNIER, J.-., CALAMANTE, F., GADIAN, D.G. and CONNELLY, A., 2004. Direct estimation of the fiber orientation density function from diffusion-weighted MRI data using spherical deconvolution. *NeuroImage*, **23**(3), pp. 1176-1185.

TOURNIER, J., CALAMANTE, F. and CONNELLY, A., 2007. Robust determination of the fibre orientation distribution in diffusion MRI: Non-negativity constrained super-resolved spherical deconvolution. *NeuroImage*, **35**(4), pp. 1459-1472.

TUCH, D.S., REESE, T.G., WIEGELL, M.R., MAKRIS, N., BELLIVEAU, J.W. and WEEDEN, J.V., 2002. High Angular Resolution Diffusion Imaging Reveals Intravoxel White Matter Fiber Heterogeneity. *Magnetic Resonance in Medicine, Communications*, pp. 577-582.

TUSTISON, N. and GEE, J., 2009. N4ITK: Nick's N3 ITK implementation for MRI bias field correction. *Insight Journal*.

TUSTISON, N.J., AVANTS, B.B., COOK, P.A., ZHENG, Y., EGAN, A., YUSHKEVICH, P.A. and GEE, J.C., 2010. N4ITK: improved N3 bias correction. *IEEE Transactions on Medical Imaging*, **29**(6), pp. 1310-1320.

VIOLA, P. and WELLS III, W.M., 1997. Alignment by Maximization of Mutual Information. *International Journal of Computer Vision*, **24**(2), pp. 137-154.

VON DER HEIDE, R.J., SKIPPER, L.M., KLOBUSICKY, E. and OLSON, I.R., 2013. Dissecting the uncinat fasciculus: disorders, controversies and a hypothesis. *Brain*, **136**(6), pp. 1692-1707.

VOYTKO, M., 1999. Impairments in acquisition and reversals of two-choice discriminations by aged rhesus monkeys. *Neurobiology of Aging*, (20), pp. 617-627.

WEEDEN, V., HAGMANN, P., TSENG, W., REESE, T. and WEISSKOFF, R., 2005. Mapping complex tissue architecture with diffusion spectrum magnetic resonance imaging. *Magnetic Resonance in Medicine*, pp. 1377-1386.

WHEELER-KINGSHOTT, C. and CERCIGNANI, M., 2009. About axial and radial diffusivities. *Magnetic Resonance in Medicine*, pp. 1255-1260.

WOLD, S., ESBENSEN, K. and GELADI, P., 1987. Principal component analysis. *Chemometrics and Intelligent Laboratory Systems*, **2**(1), pp. 37-52.

WU, M., CHANG, L., WALKER, L., LEMAITRE, H., BARNETT, A.S., MARENCO, S. and PIERPAOLI, C., 2008. Comparison of EPI distortion correction methods in diffusion tensor MRI using a novel framework, *International Conference on Medical Image Computing and Computer-Assisted Intervention 2008*, Springer, pp. 321-329.

ZHANG, Y., BRADY, M. and SMITH, S., 2001. Segmentation of Brain MR Images through a hidden Markov random field model and the expectation-maximization algorithm. *IEEE Transactions Medical Imaging*, **20**(1), pp. 45-57.